Gas Jets in Granular Matter

Observed by a High Speed X-ray Tomography System

Gas Jets in Granular Matter

Observed by a High Speed X-ray Tomography System

Proefschrift

ter verkrijging van de graad van doctor
aan de Technische Universiteit Delft,
op gezag van de Rector Magnificus Prof.ir.K.C.A.M.Luyben,
voorzitter van het College voor Promoties,
in het openbaar te verdedigen op Woensdag 11 maart 2015 om 10.00 uur

door

Xiaogang Yang

geboren op 8 mei 1984 te Gansu, P.R.China

Dit proefschrift is goedgekeurd door de promotor:

Prof. dr. R. F. Mudde
Copromotor:
Dr. J. R. van Ommen

Samenstelling promotiecommissie:

Rector Magnificus,	voorzitter
Prof. dr. R. F. Mudde	Technische Universiteit Delft, promotor
Dr. J. R. van Ommen	Technische Universiteit Delft, copromotor
Prof. dr. ing. U. Hampel	Technische Universität Dresden
Prof. dr. ir. J. A. M. Kuipers	Technische Universiteit Eindhoven
Prof. dr. A. Schmidt-Ott	Technische Universiteit Delft
Prof. dr. ir. J. J. Derksen	Technische Universiteit Delft
Dr. A. Thorton	Universiteit Twente

Printed by: Proefschriftmaken.nl || Uitgeverij BOXPress

Published by: Uitgeverij BOXPress, 's-Hertogenbosch

ISBN 978-94-6295-130-3

An electronic version of this dissertation is available at
http://repository.tudelft.nl/.

Contents

1

Introduction

1.1. Fluidized Beds

A fluidized bed is a device for fluid-solid contacting. The fluid can be a liquid, but in most cases it is a gas; we will focus on gas-solid fluidized beds in this dissertation. The solid phase consists of particles with a size in the ranges from nanometers to millimeters. The fluid and the particles are contained in a vessel with a gas distributor in the bottom, through which an upward gas flow is blown (see Fig. 1.1(a)). The mixture of gas and particles behaves like a fluid when the gas exceeds a specific superficial velocity, which is called minimum fluidization velocity (U_{mf}): the particles are lifted and start to move around. One of the benefits of the fluid-like behaviour is the intense gas-solid contacting. Fluidized beds are widely applied in the process industry, for example for catalyzed gas phase reaction, combustion and gasification, coating of solid particles, etc. The commercial application of gas-solid fluidized beds started early in 1920s. A large number of studies have been done after that [1]. However, due to the complexity of gas-solid flow system, the hydrodynamics is still a challenging field [2].

For a conventional fluidized bed, when the superficial gas velocity increases, the regime changes from a packed bed, to a homogeneous fluidized bed, bubbling bed, slugging bed and finally a turbulent bed. If the particles become adhesive, channeling and jetting also possibly happen. The bubbling bed is widely used for industrial applications [3]. When the superficial gas velocity increases to a minimum bubbling velocity ($U_{mb} > U_{mf}$), the beds start bubbling in a way that resembles the boiling of a liquid. Rising gas voids in fluidized beds behaves like gas bubbles in fluids. The fluid, the mixture of gas and solid particles, is then the continuous phase. In that state there is a homogeneous mixing of the gas and particles, so there will be no local hot spots. The gas and particles have a very large contact surface area to react.

Understanding the bubble behavior is of key importance when studying the physics and engineering principles of the bubbling fluidized beds, because the rising bubbles cause motion of the particulate phase which is the main source of solids mixing. Freely bubbling beds have been systematically studied [4]. The bubbles coalesce when they move from the bottom to the top of the bed. The size of the bubbles increases when the bubbles rise, because of the coalescence and the gas expansion. The bubbles tend to move to the center of the bed when they are rising [5]. Several correlations for the bubble velocity [6] and size [7] have been developed. Due to the complexity of the gas-particle flow in the beds, modeling the system from first principles is very challenging. A great number of numerical simulations have been carried out [8–11]. However, validation of these methods is a difficult task. The bubbling flow in the fluidized beds cannot be easily visualized.

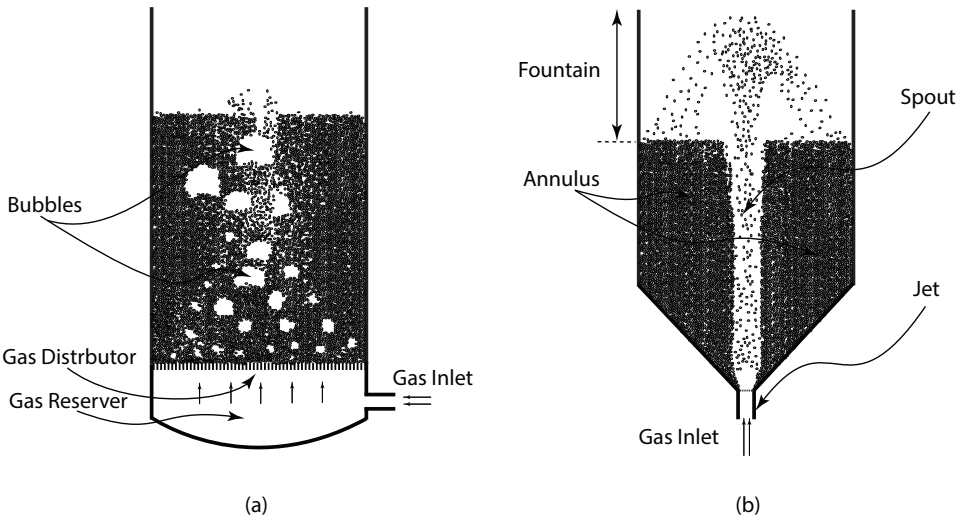

Figure 1.1: The fluidized beds: (a) A bubbling fluidized bed; (b) A spouted bed.

1.2. Gas Jets in the Fluidized Beds

In this dissertation, we use high speed X-ray tomography [12] for measuring the dynamics of the fluidized beds. By this tool, we study the hydrodynamics of two specific types of fluidized beds: a spouted bed and a downward micro-nozzle assisted fluidized bed. These techniques are typically applied to coarse particles and nano-particles, respectively. They are both gas jets in the fluidized beds: a centimeter scale jet and a millimeter scale jet.

For coarse particles (larger than 500 μm in diameter), the space between particles is relatively large in a fluidized bed. The flow rate to attain the minimum fluidized condition is too high in practice [13, 14]. A spouted bed is a better approach to

make the particles circulating with a smaller gas flow rate. Similar to a conventional fluidized bed, there is a vessel to contain the solid particles, and a gas injection from the bottom of the vessel. Differently, all the gas is injected through an orifice in the bottom plate, instead of homogeneously through the distribution plate (see Fig.1.1(b)).

For spouted beds, there is a superficial gas velocity called minimum spouted velocity (U_{ms}). When the superficial gas velocity is higher than U_{ms}, a spout is formed. The gas mainly concentrates in the spout region (see Fig. 1.1), where the gas jet interacts with the particles. The particles are carried from the bottom to the top of the bed through the spout, and move back through the fountain and the annulus. The particle concentration is much smaller, and the velocity is much higher in the spout than in the annulus. These properties can be used to distinguish the spout region from the annular region. The spout size is a key variable for modeling the spouted bed, and for engineering calculation. Spout diameters were measured directly in half-cylindrical beds by Malek et al. [15] and McNab [16]. Later, a fiber optic probe was used to measure spout diameters by He et al. [17, 18] in both half and full columns. The time-averaged spout diameter was measured by Wu et al. [19] with an X-ray CT scanner in a full column. Theoretical predictions were also made [15, 16, 20]. There are deviations for the predicted values between the half-column models and full-column models [18, 21]. The spout size is considered as stationary by the previous studies. A dynamic study lacks for the spout stability.

Nano-particles are typically hard to be fluidized because of their strongly cohesive nature. A downward nozzle is proposed to break-up the agglomerates and assist the fluidization in the bed [22]. The micro-nozzle can provide a very high outlet velocity at a relatively low flowrate. We insert a tube with the nozzle at the outlet from the top of the bed and let it face downward to the bottom of the bed. Consequently, the gas flow from the nozzle is opposite to the gas flow from the distribution plate. An increased intensity of agglomerate collisions as well as high local shear are created in this way, which are likely the mechanism for breaking the agglomerates. We will measure the flow pattern of this downward micro-nozzle system to start the study for this mechanism.

The downward micro-nozzle assisted fluidized bed is barely studied. However, other kind of nozzles are widely applied and studied for assisting the fluidized beds. The nozzle can be placed upwards [23, 24], horizontally [25, 26], and downwards [22, 27] in the bed in a single or multiple number [28, 29]. A fluidized bed with a single upwards nozzle is a very popular setup for validating the experimental and numerical techniques [30], because it can easily form a single bubble with an accurate manipulation for the bubble size and velocity. The gas flow from the downward or horizontal nozzle is rather complicated, since the direction of the gas flow is different for the gas coming from the distribution plate and the nozzle. For the downward nozzle, the gas from the nozzle is blown opposite to the drag force of the particles. It is hard to model such kind of gas/particle turbulent flow. Modeling

for the turbulent gas jet injecting to the open air is already a difficult topic [31]. The accuracy of these models critically depends on the experimental correction for their coefficients. For the more complicated case: the downward or horizontal nozzle in the fluidized bed, a measurement of the gas jet is of key importance to study the fluid flow. A time-resolved observation of the gas distribution is an attractive way to study the gas flow in the particle phase.

1.3. Experimental Methods

There is a big obstacle for observing fluidized beds directly: the opaque nature of the dense gas-solid mixture. Measurement techniques based on visible light or lasers are rather limited. Although, pseudo 2-D beds and half-column beds have been studied with the aid of video techniques [32–35], they cannot accurately represent the 3-D beds. The wall effects in 2-D beds or the half column beds cannot easily be estimated. Such 2-D measurement just has limited use, for instance, for the calibration of other types of measurement equipment and validation of simulation codes. We should be cautious of using them for determining the hydrodynamics. Probe [36–39] measurements can be used in 3-D beds. However, they are intrusive, and only capable of measuring local values. These classical techniques are not sufficient for exploring the flow patterns of fluidized beds in detail.

Advanced experimental techniques are required to elucidate the flow behaviour of fluidized beds in detail, even though numerical methods have contributed significantly to the current understanding [40, 41]. Tomographic techniques such as X-ray tomography and ECT (Electrical Capacitance Tomography), which do not rely on visible light, make it possible to explore the internal motion of fluidized beds [42, 43]. Comparing X-ray tomography and ECT, ECT is cheaper and easier to use, but X-ray tomography is easier to interpret, because X-ray tomography is a so-called *hard-field tomographic technique* while ECT is a *soft-field tomographic technique*. The field lines for *hard-field tomography* are straight, while *soft-field tomography* has non-linear field lines. Consequently, the image reconstruction for ECT is much more troublesome. Moreover, with X-ray CT a higher spatial resolution can be obtained [44].

Although X-ray CT is well developed for medical application, the use in fluidized bed only started in the 1990s; see Kantzas [45]. It was first applied to determine the time-averaged gas hold-up in a gas-solid bed [46, 47]. After that, an X-ray CT system was applied to measure the time-averaged local solids distribution in a circulating fluidized bed by Grassler and Wirth [48]. An X-ray imaging system was developed by Heindel et al. [49] to achieve 3-D visualization for fluidized beds, which can also provide time-averaged CT imaging for the fluidized beds [50, 51]. All the early applications faced a practical limit of X-ray CT: the scanning time of traditional X-ray CT is too long to record the dynamics of the flow of a fluidized bed [52]. Time averaged data is rather limited when analyzing the dynamic phenomena of fluidized beds.

As a fluidized bed is a dynamic system, time-resolved tomographic measurements are highly desirable. A high speed X-ray tomography system has been developed for measuring the bubbling flow in a fluidized bed by Mudde et al. [12]. Three X-ray sources are set up at equal angles around the bed to generate projections simultaneously, so that detector arrays receive the attenuated X-ray signals at the same time. A time resolution of 2500 frames/second can be reached. Meanwhile, another fast X-ray system was built by Bieberle et al. [53] and used with gas liquid flow. They use a fast scanning electron beam to hit a tungsten target bar, creating many independent views from different angles per unit time. The frame rate can be as high as 5000 frames/second [54]. Later, it was also applied to a fluidized bed [55]. Both of these fast X-ray CT systems have high enough time resolution to study multiphase fluid flow. Mudde and co-workers studied fluidized beds with a diameter up to 24 cm. A maximum pixel size of 5 mm is desired to be able to image bubbles as small as 15 mm [56].

1.4. Scientific Questions

The image reconstruction for the high speed X-ray tomography system is an ill-posed inverse problem, for which several studies have been done. *How do the reconstruction techniques perform for the fluidized beds we study?*

Previous studies have just considered the time-averaged spout shape and position in a spouted bed. *If we observed it with high temporal and spatial resolution, is there dynamic behaviour to be found? If so, how does it change when flow conditions change?*

A downward micro-nozzle is expected to assist the fluidization of nano-powders. However, the fluid flow of such gas jet in granular matter has not been studied. *How does the nozzle influence the fluid flow in the bed? What is the flow pattern of the gas from the nozzle?*

1.5. Outline

This dissertation comprises an introduction to the multi-source high speed tomography system, and four papers on studies carried out with this system. Chapter 3 to 6 are thus self-contained.

Chaper 2 is an introduction to the high speed X-ray tomography system. It provides a detailed description of the hardware of this system. The basics of X-ray generation and detecting are introduced. The measuring principle and data calibration procedure are presented.

Chapter 3 and 4 are papers about the tomographic reconstruction algorithms. In

Chapter 3, we evaluate and compare the Simultaneous Algebraic Reconstruction Technique (SART) and Adaptive Genetic Algorithm (AGA). In Chapter 4, a hybrid reconstruction algorithm is developed by combining SART and AGA.

Chapter 5 is a paper on the dynamic measurement of a flat base spouted bed. The hybrid reconstruction algorithm is applied. A novel data processing approach, which processes the raw data directly without reconstruction, is developed for the spouted bed. The time-averaged results are used to validate our measurements and data process. A particle circulation model is developed based on these results. A dynamic analysis is done with the time-resolved spout diameter and position. The conditions are determined for which the spout is stable.

Chapter 6 discusses the measurement of the flow pattern of a downward gas jet in a fluidized bed. The time-averaged and time resolved gas distributions below a downward micro-nozzle are presented. The penetration depth of the jet is also obtained.

In Chapter 7, the overall conclusions are presented and an outlook to future work is given.

References

[1] D. Geldart, Gas Fluidization Technology, A Wiley-Interscience publication, pp. 4–6.

[2] M. Rudisuli, T. J. Schildhauer, S. M. A. Biollaz, J. R. van Ommen, Scale-up of bubbling fluidized bed reactors - A review, Powder Technology 217 (2012) 21–38.

[3] K. S. Lim, J. X. Zhu, J. R. Grace, Hydrodynamics of gas-solid fluidization, International Journal of Multiphase Flow 21, Supplement (1995) 141–193.

[4] D. Geldart, Gas Fluidization Technology, A Wiley-Interscience publication, pp. 53–88.

[5] D. T. Argyriou, H. L. List, R. Shinnar, Bubble growth by coalescence in gas fluidized beds, AIChE Journal 17 (1971) 122–130.

[6] K. Kato, C. Y. Wen, Bubble assemblage model for fluidized bed catalytic reactors, Chemical Engineering Science 24 (1969) 1351–1369.

[7] S. Mori, C. Y. Wen, Estimation of bubble diameter in gaseous fluidized beds, AIChE Journal 21 (1975) 109–115.

[8] N. G. Deen, M. Van Sint Annaland, M. A. Van der Hoef, J. A. M. Kuipers, Review of discrete particle modeling of fluidized beds, Chemical Engineering Science 62 (2007) 28–44.

[9] P. A. Cundall, O. D. L. Strack, A discrete numerical model for granular assemblies, Géotechnique 29 (1979) 47–65(18).

[10] G. A. Bokkers, M. van Sint Annaland, J. A. M. Kuipers, Mixing and segregation in a bidisperse gas–solid fluidised bed: a numerical and experimental study, Powder Technology 140 (2004) 176–186.

[11] T. McKeen, T. Pugsley, Simulation and experimental validation of a freely bubbling bed of fcc catalyst, Powder Technology 129 (2003) 139–152.

[12] R. F. Mudde, J. Alles, T. H. J. J. van der Hagen, Feasibility study of a time-resolving x-ray tomographic system, Measurement Science & Technology 19 (2008). 8th International Symposium on Measurement Technology and Intelligent Instruments, Tohoku Univ, Sendai, Japan, Sep. 24-27, 2007.

[13] N. Epstein, J. R. Grace, Spouted and spout-fluid beds: fundamentals and applications, Cambridge University Press, 2011.

[14] V. S. Sutkar, N. G. Deen, J. A. M. Kuipers, Spout fluidized beds: Recent advances in experimental and numerical studies, Chemical Engineering Science 86 (2013) 124–136.

[15] M. A. Malek, L. A. Madonna, B. C.-Y. Lu, Estimation of spout diameter in a spouted bed, Industrial & Engineering Chemistry Process Design and Development 2 (1963) 30–34.

[16] G. McNab, Prediction of Spout Diameter, British Chemical Engineering and Process Technology 17 (1972) 532–535.

[17] Y. He, C. Lim, J. Grace, J. Zhu, S. Qin, Measurements of Voidage Profiles in Spouted Beds, Canadian Journal of Chemical Engineering 72 (1994) 229–234.

[18] A.-L. He, C. J. Lim, J. R. Grace, S.-Z. Qin, Spout diameters in full and half spouted beds, Canadian Journal of Chemical Engineering 76 (1998) 702–706.

[19] B. Wu, A. Orta, A. Kantzas, Experimental Flow Measurements of a Spouted Bed Using Pressure Transducer and X-Ray CT Scanner, International Journal of Chemical Reactor Engineering 9 (2011).

[20] J. Bridgwater, K. B. Mathur, Prediction of spout diameter in a spouted bed—a theoretical model, Powder Technology 6 (1972) 183 – 187.

[21] E. Zanoelo, S. Rocha, Spout shape predictions in spouted beds, Canadian Journal of Chemical Engineering 80 (2002) 967–973.

[22] J. A. Quevedo, A. Omosebi, R. Pfeffer, Fluidization enhancement of agglomerates of metal oxide nanopowders by microjets, AIChE Journal 56 (2010) 1456–1468.

[23] D. J. Patil, M. van Sint Annaland, J. A. M. Kuipers, Critical comparison of hydrodynamic models for gas–solid fluidized beds—part i : bubbling gas–solid fluidized beds operated with a jet, Chemical Engineering Science 60 (2005) 57–72.

[24] C. Guenther, M. Syamlal, The effect of numerical diffusion on simulation of isolated bubbles in a gas–solid fluidized bed, Powder Technology 116 (2001) 142–154.

[25] S. Ariyapadi, D. W. Holdsworth, C. J. D. Norley, F. Berruti, C. Briens, Digital x-ray imaging technique to study the horizontal injection of gas-liquid jets into fluidized beds, International Journal of Chemical Reactor Engineering 1 (2003). Ariyapadi, Siva Holdsworth, David W. Norley, Chris J. D. Berruti, Franco Briens, Cedric.

[26] T. Li, K. Pougatch, M. Salcudean, D. Grecov, Numerical simulation of horizontal jet penetration in a three-dimensional fluidized bed, Powder Technology 184 (2008) 89–99.

[27] P. Sauriol, H. Cui, J. Chaouki, Gas jet penetration lengths from upward and downward nozzles in dense gas–solid fluidized beds, Powder Technology 235 (2013) 42–54.

[28] T. Li, K. Pougatch, M. Salcudean, D. Grecov, Numerical simulation of single and multiple gas jets in bubbling fluidized beds, Chemical Engineering Science 64 (2009) 4884–4898.

[29] R. Y. Hong, Q. J. Guo, G. H. Luo, J. Y. Zhang, J. Ding, On the jet penetration height in fluidized beds with two vertical jets, Powder Technology 133 (2003) 216–227.

[30] R. P. Utikar, V. V. Ranade, Single jet fluidized beds: Experiments and cfd simulations with glass and polypropylene particles, Chemical Engineering Science 62 (2007) 167–183.

[31] N. Rajaratnam, Turbulent Jets, Elsevier Science, pp. 27–48.

[32] R. F. Mudde, H. B. M. Schulte, H. E. A. van den Akker, Analysis of a bubbling 2-d gas-fluidized bed using image processing, Powder Technology 81 (1994) 149–159.

[33] K. S. Lim, P. K. Agarwal, B. K. O'Neill, Measurement and modelling of bubble parameters in a two-dimensional gas-fluidized bed using image analysis, Powder Technology 60 (1990) 159–171.

[34] M. J. V. Goldschmidt, J. M. Link, S. Mellema, J. A. M. Kuipers, Digital image analysis measurements of bed expansion and segregation dynamics in dense gas-fluidised beds, Powder Technology 138 (2003) 135–159.

[35] M. Horio, H. Kuroki, Three-dimensional flow visualization of dilutely dispersed solids in bubbling and circulating fluidized beds, Chemical Engineering Science 49 (1994) 2413–2421.

[36] J. X. Zhu, G. Z. Li, S. Z. Qin, F. Y. Li, H. Zhang, Y. L. Yang, Direct measurements of particle velocities in gas–solids suspension flow using a novel five-fiber optical probe, Powder Technology 115 (2001) 184–192.

[37] J. M. Schweitzer, J. Bayle, T. Gauthier, Local gas hold-up measurements in fluidized bed and slurry bubble column, Chemical Engineering Science 56 (2001) 1103–1110.

[38] J. Ren, Q. Mao, J. Li, W. Lin, Wavelet analysis of dynamic behavior in fluidized beds, Chemical Engineering Science 56 (2001) 981–988.

[39] J. Liu, J. R. Grace, X. Bi, Novel multifunctional optical-fiber probe: I. development and validation, AIChE Journal 49 (2003) 1405–1420.

[40] H. Arastoopour, Numerical simulation and experimental analysis of gas/solid flow systems: 1999 fluor-daniel plenary lecture, Powder Technology 119 (2001) 59–67.

[41] A. Busciglio, G. Vella, G. Micale, L. Rizzuti, Analysis of the bubbling behaviour of 2D gas solid fluidized beds: Part II. Comparison between experiments and numerical simulations via Digital Image Analysis Technique, Chemical Engineering Journal 148 (2009) 145 – 163.

[42] S. B. Kumar, D. Moslemian, M. P. Dudukovic, Gas-holdup measurements in bubble columns using computed tomography, AIChE Journal 43 (1997) 1414–1425.

[43] C. G. Xie, S. M. Huang, B. S. Hoyle, R. Thorn, C. Lenn, D. Snowden, M. S. Beck, Electrical capacitance tomography for flow imaging - system model for development of image-reconstruction algorithms and design of primary sensors, IEEE Proceedings-G Circuits Devices and Systems 139 (1992) 89–98.

[44] J. R. van Ommen, R. F. Mudde, Measuring the Gas-Solids Distribution in Fluidized Beds-A Review, International Journal of Chemical Reactor Engineering 6 (2008).

[45] A. Kantzas, Computation of Holdups in Fluidized and Trickle Beds by Computer-Assisted Tomography, AIChE Journal 40 (1994) 1254–1261.

[46] A. Kantzas, I. Wright, N. Kalogerakis, Quantification of channelling in polyethylene resin fluid beds using X-ray computer assisted tomography (CAT), Chemical Engineering Science 52 (1997) 2023 – 2035.

[47] I. Wright, K. Hamilton, S. Kruychkov, J. Chen, F. Li, A. Kantzas, On the measurement of hydrodynamic properties of an air-polyethylene fluidized bed system, Chemical Engineering Science 56 (2001) 4085–4097.

[48] T. Grassler, K.-E. Wirth, X-ray computer tomography — potential and limitation for the measurement of local solids distribution in circulating fluidized beds, Chemical Engineering Journal 77 (2000) 65 – 72.

[49] T. J. Heindel, J. N. Gray, T. C. Jensen, An X-ray system for visualizing fluid flows, Flow Measurement and Instrumentation 19 (2008) 67–78.

[50] J. B. Drake, T. J. Heindel, Comparisons of Annular Hydrodynamic Structures in 3D Fluidized Beds Using X-Ray Computed Tomography Imaging, Journal of Fluids Engineering-Transactions of The ASME 134 (2012).

[51] J. B. Drake, T. J. Heindel, Local time-average gas holdup comparisons in cold flow fluidized beds with side-air injection, Chemical Engineering Science 68 (2012) 157–165.

[52] T. J. Heindel, A Review of X-Ray Flow Visualization With Applications to Multiphase Flows, Journal of Fluids Engineering-Transactions of The ASME 133 (2011).

[53] M. Bieberle, F. Fischer, E. Schleicher, U. Hampel, D. Koch, K. S. D. C. Aktay, H.-J. Menz, H.-G. Mayer, Ultrafast limited-angle-type x-ray tomography, Applied Physics Letters 91 (2007).

[54] M. Bieberle, F. Fischer, E. Schleicher, D. Koch, H. J. Menz, H. G. Mayer, U. Hampel, Experimental two-phase flow measurement using ultra fast limited-angle-type electron beam x-ray computed tomography, Experiments in Fluids 47 (2009) 369–378.

[55] M. Bieberle, F. Barthel, U. Hampel, Ultrafast X-ray computed tomography for the analysis of gas-solid fluidized beds, Chemical Engineering Journal 189 (2012) 356–363.

[56] X. Yang, J. R. van Ommen, R. F. Mudde, Comparison of genetic algorithm and algebraic reconstruction for x-ray tomography in bubbling fluidized beds, Powder Technology 253 (2014) 626–637.

2

High Speed X-ray Tomography

A high speed X-ray tomography system is further developed for measuring the dynamics of the gas phase in the fluidized beds. Multiple X-ray sources and detector arrays are used for scanning the cross section of the beds simultaneously. The basics of the high speed X-ray tomography system will be introduced in this chapter. Section 2.1 starts from the classical medical X-ray CT. The particularity of the setup for the high speed X-ray tomography is discussed. Section 2.2 & 2.3 refresh the background of the X-ray generation and X-ray detection. Section 2.4 & 2.5 give the theoretical background and method of translating the X-ray intensity signal to the path length that it travels through specific matter. Section 2.6 is a discussion of the data processing for the high speed X-ray tomography system.

2.1. The Experimental Setup

X-ray computed tomography (X-ray CT) is an imaging technique to detect the density distribution of materials. It is sometimes also named computed axial tomography (CAT) or computer-assisted tomography. It uses X-rays to scan the internal structures of the objects which are not transparent for visible light. X-ray attenuation is the basic principle to measure the thickness of a matter from the measured X-ray intensity. An image reconstruction translates the X-ray attenuation signals to images. Medical imaging is the most common application of X-ray CT. There are also applications in industry, such as flaw detection, failure analysis, metrology, assembly analysis and reverse engineering applications [1].

Typically, X-ray CT is only applied to static objects, because it needs to rotate the X-ray source and detector array for scanning the full angle of the objects (see Fig. 2.1). This procedure requires measuring time on the order of a second. For measuring the change of the phase distribution in multiphase flow, such scanning speed is too low. A multi-source X-ray CT system has been developed [2], which is called a high speed X-ray tomography system.

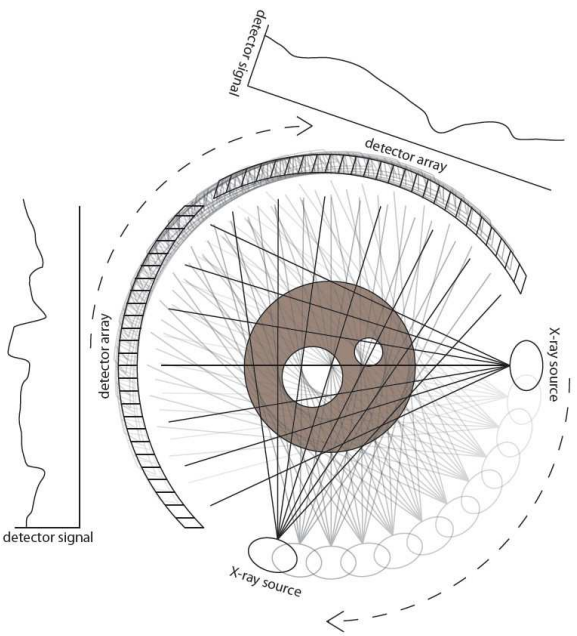

Figure 2.1: Top view of the classical medical X-ray CT system [3].

Different from the traditional X-ray CT in medical use, the high speed X-ray tomography system is composed of 3 X-ray tubes and 3 detector arrays. The X-ray tubes are placed at 120° around the fluidized bed. The detector arrays are placed oppo-

site the X-ray sources. As is illustrated in Fig. 2.2, this design makes it possible to simultaneously obtain the X-ray attenuation information from different directions. This is the basic condition to reconstruct the image of the object's cross section from the projections' attenuation information.

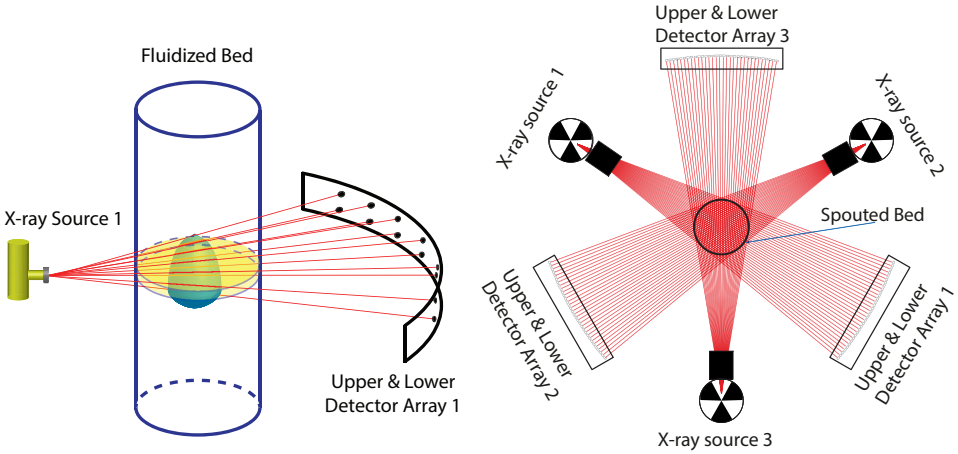

Figure 2.2: Top view of the simulated measurement system with the fluidized bed placed in the center.

The set-up allows instantaneously scanning, but also restricts the total number of X-ray projections, due to the limited space to place the detectors. In traditional X-ray CT, thousands of scanning points can be made with current technology by rotating the source and detector around the object of interest. In the present case, only as many as 96 scanning points are available for one reconstruction.

2.2. X-ray Generation

X-ray is a form of electromagnetic radiation with a wavelength in the range roughly from 0.01 to 10 nm (see Fig. 2.3). It is also called Röntgen radiation, with the name of Wilhelm Röntgen, who is usually credited as its discoverer, and who had named it X-radiation to signify an unknown type of radiation. The high energy photon of X-ray is capable to penetrate matter that is non-transparent to visible light. This feature makes X-ray one of the most important visualization tool for detecting the inside structure of objects that are non-transparent to visible light.

Typically, X-rays are generated from an evacuated tube with a cathode and anode, by which electrons are accelerated to a high voltage (Fig. 2.4). The voltages across the cathode and anode typically range from 30 to 150 kV. Once an electron reaches the anode, it will interact with the anode material. If an electron passes close by the nucleus of an atom of the anode material, it will be deflected because of its charge. This deflection causes the electron to lose energy, which is emitted in the

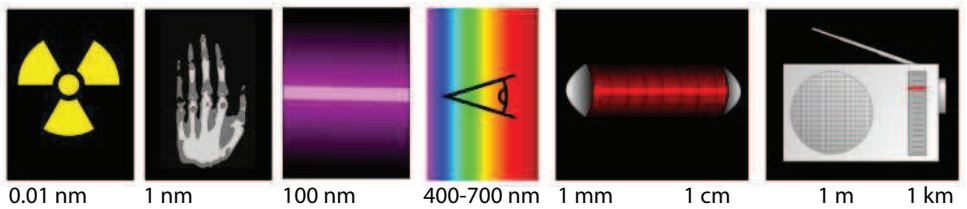

Figure 2.3: Overview of the electromagnetic spectrum. Source: Wikipedia.

form of Bremsstrahlung.

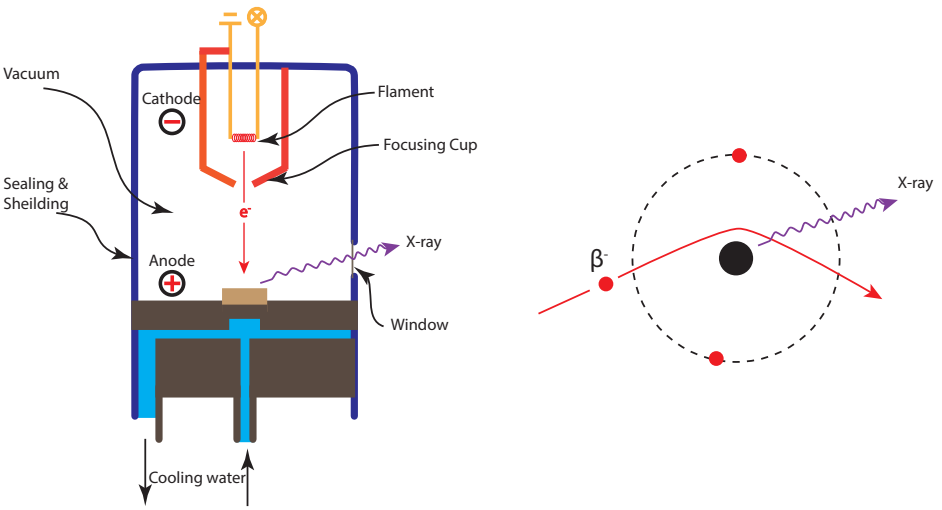

Figure 2.4: Left: Simplified schematic overview of X-ray tube with water cooling; Right: Interaction between incoming electron and nucleus that causes Bremsstrahlung.

Roughly 1% of the energy is converted into X-ray radiation, the rest of the electrons undergo many collisions and convert their energy into heat. The heat focuses on the anode and could melt it. To prevent this, high-melting-point materials such as Tungsten and Molybdenum are commonly used. Moreover, a rotating disc anode or a water cooling system is equipped to protect the anode. Depending on the type of material of the anode and the accelerating voltage, different X-ray spectra can be generated. If an incoming electron has an energy of E_{photon}, the energy of the emitted photons will range from 0 to E_{photon}. A continuous spectrum of photons will be generated. Depending on the type of material used for the anode, several characteristic lines will be visible in the spectrum. These lines are caused by electrons filling holes in the atom shell, which in turn are caused by the incoming electrons interacting with bound electrons and ejecting them.

We use 3 YXLON Y.TU 160-D06 tubes (see Fig. 2.5) in the setup, with a maximum voltage of 160 kV and a maximum current of 12 mA. They are water cooled and are able to operate continuously for an unlimited time. A lead collimator is placed in front of the tube to create a flat measurement plane. It also reduces the amount of scattered radiation. The tubes are controlled by 3 YXLON MGC41 controlling units. This makes it possible to fire all X-ray sources at once, although settings can be set for each tube individually. The tubes are usually set to 150 kV and depending on the type of vessel and particles inside it, a suitable current is selected. A higher current gives a clearer signal, but it might also overexpose the detectors. It is possible to use a higher current and shield the detectors using copper plates. This will absorb part of the radiation and prevent overexposure.

Prolonged exposure to X-rays is dangerous to living organisms. For this reason 5 mm lead plates are mounted on the walls and underneath the floor of the measurement room. The ceiling of the measurement room is fitted with 2 mm lead plating. The experiments are controlled from outside the measurement room. This control room is shielded from radiation and safe to work in during measurements. The doors that close the measurement room have an interlock system that prevents the X-ray tubes from working if they are not closed properly. Also the amount of radiation in the control room is monitored using thermo-luminescence dosimeters which are checked periodically.

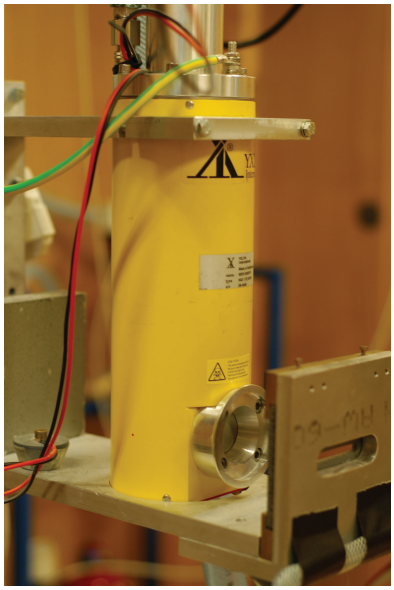

Figure 2.5: Photo for the X-ray tube in our setup.

2.3. X-ray Detecting

X-ray detecting is the procedure to convert the energy of photons to electric current, by which the intensity of the X-ray can be evaluated digitally. There are usually two types of X-ray detectors: an ionization and a scintillation detector [4].

In an ionization detector there are two electrodes, over which a voltage is applied. A photon can be captured and will cause an electron-ion pair to be formed due to ionization. If the voltage is high enough to prevent recombination, the electron will go to the anode and the ion to the cathode. This will create a current which is a measure for the amount of photons. A Geiger-Müller tube of the well-known Geiger counter works by using this principle. There are also solid-state ionization

detectors. Here the ions do not move, but the electrons do and this will also create a current.

Scintillations are flashes of light that are produced by certain materials when they are exposed to high energy photons. There are various materials that can be used to detect X-rays in this way. Scintillators are defined by their short fluorescence decay times ($10^{-5} \sim 10^{-9}$s) and their own transparency to the wavelengths they produce. If a photon interacts with the photocathode electrons will be emitted. These will be focused on the first dynode, which in turn will multiply the electrons by the process of secondary emission. In this way the cascade of electrons will generate a peak signal at the anode. In this way each scintillation pulse will produce a clear signal. Photodiodes are solid-state devices that contain a p-n junction, usually with an intrinsic (undoped) layer in between them. These devices are called PIN photodiodes. Light absorbed by the intrinsic layer generates electron-hole pairs that are collected at the anode and cathode, respectively. This generates a measurable signal. A big advantage of photodiodes is their relatively small size and low price. This allows them to be packed into arrays, for example. They can be operated in counting mode, where individual photons and their energies are detected, however the count rates cannot be too high. But they can also be run in integral mode, where they give an output proportional to the integral radiant energy fluence rate. The number of photons hitting a detector can be modeled as a Poisson process. The stochastic nature of photon counting results in an uncertainty in the measurement values.

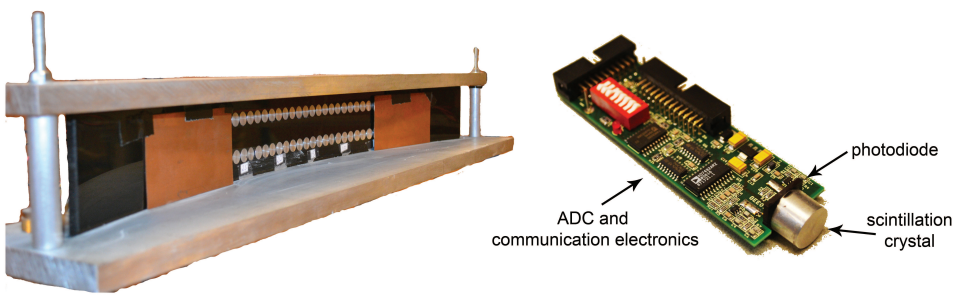

Figure 2.6: Left: Picture of one of the detector banks. The scintillation crystals of the lower and upper arrays can be seen, some with copper plating in front of them. Right: One of the in total 192 detector boards close up [3].

The detector arrays for our setup consist of two planes of each 32 Hamamatsu S1337 - 1010BR detectors (see Fig. 2.6). These are CdWO4 scintillation crystals, which are optically coupled to the PIN photodiode. Their crystal size is 10 mm x 10 mm x 10 mm. These detectors are installed on a small printed circuit board (Fig. 2.6: Right) which are mounted in a curved plastic arc. The curvature of this arc is such that all detectors are aimed directly at the X-ray tube on the opposite side of the setup. The measurement signal of the detectors is fed through a 12-bit ADC at

2.5 kHz and stored on the CompactRIO. This data is later used to reconstruct the tomograms. The detectors arrays are shielded against scattered X-rays using a lead shielded casing. The left of Fig. 2.6 shows one of the three detector banks without the lead shielding. Two copper plates are mounted to prevent overexposure of the outer detectors.

2.4. Measuring Principle

For a monoenergetic beam passing through homogeneous material, we know the attenuation rate. If the attenuation coefficient is defined, the thickness of the matters can be calculated. This is the well-known Lambert-Beer law:

$$\frac{\Phi(x)}{\Phi_o} = exp(-\mu x) \tag{2.1}$$

where Φ_o is the incident X-ray intensity, which is the number of photons registered per second when the system is in vacuum; $\Phi(x)$ is the X-ray intensity after passing a distance through the material; μ is the linear absorption coefficient of the material; and x is the distance of the X-ray passing through the material.

Actually, X-ray radiation has a broad energy spectrum (see Fig. 2.7), forming polychromatic radiation, for which the simple Lambert-Beer law does not work anymore. When a polychromatic beam propagates through a medium, relatively more photons are absorbed in the low energy part than in the high energy part. This phenomenon is known as beam hardening. Consequently, a single attenuation coefficient, that depends only on the photon energy, does not work for an elegant reconstruction.

There are two quantities to describe a polychromatic photon beam: the *spectrally distributed photon fluence rate* Φ_E, and the *spectrally distributed energy fluence rate* Ψ_E. Φ_E is the number of photons per unit area per unit time with energy between E and $E + dE$. Ψ_E is the radiant energy per unit area per unit time carried by photons with an energy between E and $E + dE$. The subscript E denotes the spectral nature (i.e., per energy interval) of a quantity. Here $\Psi_E = E\Phi_E$. With these quantities, the Lambert-Beer law for the attenuation of polychromatic radiation in a homogeneous medium becomes[5]:

$$\Phi(x) = \int (\Phi_E)_0 exp(-\mu(E)x)dE \tag{2.2}$$

It can be derived that [5]:

$$\frac{\Phi(x)}{\Phi_0} = exp(-\int_0^x \langle\mu\rangle_\Phi(x)dx) \tag{2.3}$$

where $\langle\mu\rangle_\Phi$ is the $\mu(E)$ averaged over the local spectrum of the beam at position x. The integral for it is rather difficult to complete. The exact value of $\langle\mu\rangle_\Phi$ for

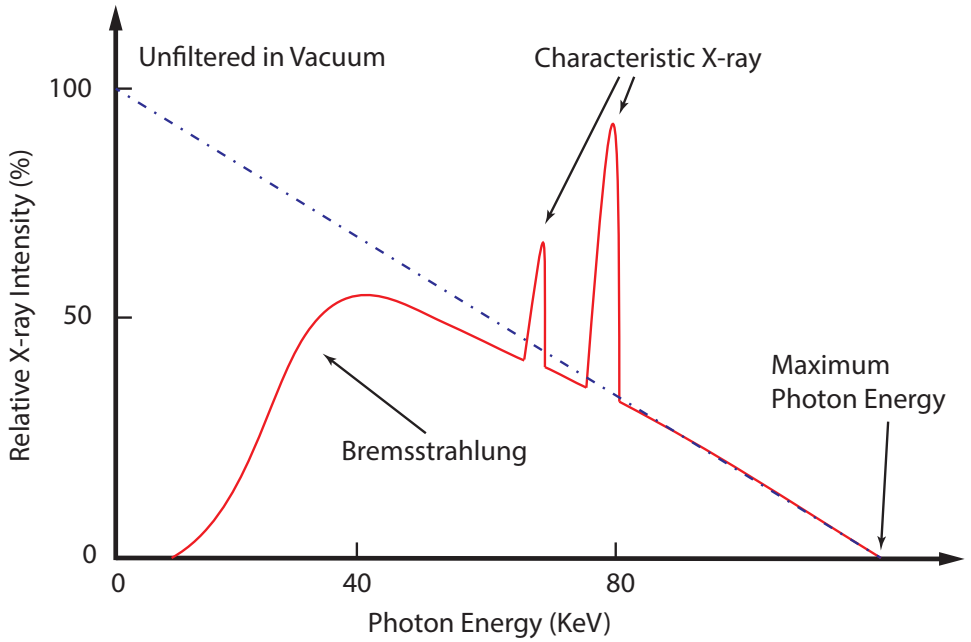

Figure 2.7: Typical X-ray spectrum.

different Φ and x is very difficult to estimate in the real measurement.

Thus, an effective attenuation coefficient is defined by many researchers [5–8]. Bjärngard and Shackford [6] stated that a clear and accepted definition of the attenuation of a broad spectrum of X-rays is lacking. Later Kleinschmidt [8] considered the effects of beam hardening in a formal way. In his paper, Kleinschmidt considers this issue and provides a formal definition of the average attenuation coefficient, $\langle\mu\rangle$. In order to find a semi-analytical expression for the attenuation coefficient as a function of the penetration depth (x), several model functions were tested [8]. However, it is very difficult to determine the parameters of the theoretical or semi-theoretical models in the real measurement. Even for a monochromatic beam, it requires very sophisticated energy discrimination techniques. A detector with such accuracy is too expensive to build arrays for X-ray tomography. For the polychromatic beam, this becomes impossible as one cannot see from a photon whether it is a scattered one that had originally a high energy, or an undisturbed one that has kept its original low energy. Millner et al. [9] suggest a calibration with an effective energy E_{eff}. If the effective energy of a specific setup is known, an approximate attenuation law can be used :

$$\Psi(x)_m \approx \Psi_m exp(-\mu(E_{eff})x) \tag{2.4}$$

Later, Alles and Mudde [5] found that it is possible to use an exponential function to calibrate the measured X-ray intensity I and the path length (l) of the ray passing

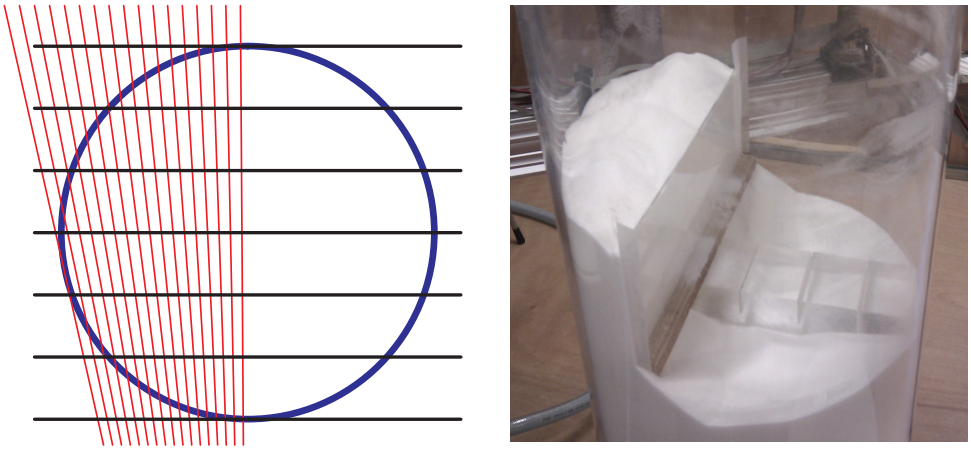

(a) (b)

Figure 2.8: The 7 points calibration: (a) The diagram of the path length, the red line is the X-ray, the blue line is the wall of the column, the black line is the slab to dividing the particles; (b) The real setup for the measurement.

through the packed powders. This fitting is simple and accurate for the measurement of the fluidized bed with the high speed X-ray tomographic system.

2.5. Calibration

In practice, we carry out a calibration process to translate the measured X-ray intensity to the path length, which the X-rays passing through the solid phase in the fluidized bed. All the detectors are calibrated individually to circumvent the effects of beam hardening. We fill the bed with specific amounts of packed powders, by which a specific path length is set for each X-ray. The path length is calculated from the geometric model of the setup (see Fig. 2.8 (a)). We use a perspex slab with the thickness of 2 mm to divide the cross section of the bed (see Fig. 2.8 (b)). The packed powders can be filled for 7 different cross sectional areas, including a completely empty and a completely filled bed. The related X-ray intensities for all the detectors are measured.

An exponential function is applied to fit the functional relation between the measured X-ray intensity (I) and the path length (l) by Mudde et al. [2, 10–13]:

$$I = A_{cal} + B_{cal} exp\left(\frac{-l}{C_{cal}}\right) \tag{2.5}$$

where A_{cal}, B_{cal}, and C_{cal} are calibration coefficients fitted from the measured I and related l.

This equation is capable to fit a smooth curve. With the fitted equations for all the detectors, once we do measurement for the same material, the path length (l) through the material can be calculated from the measured X-ray intensity (I). Note that the exponential function in itself is not relevant. All we need is a smooth function that describes the data points accurately. The only purpose of the fitting is to convert the measured data into a particle fraction on a given X-ray beam. This fitting works well in practice.

However, we notice that the error of l from this fitting is up to 10% for the detectors that are not in the center. This happens because the principle to evaluate the fitting accuracy of Eq. 2.5 is I, not l. The fitting terminates when the error of I is smaller than the tolerance. However, the error of l may still big. Normally, this kind of error only happens for a few of detectors in the two sides of the detector arrays. It leads a few noise pixels for the final reconstruction results, but its influence is not more serious than the system noise. In previous studies, this error was neglected.

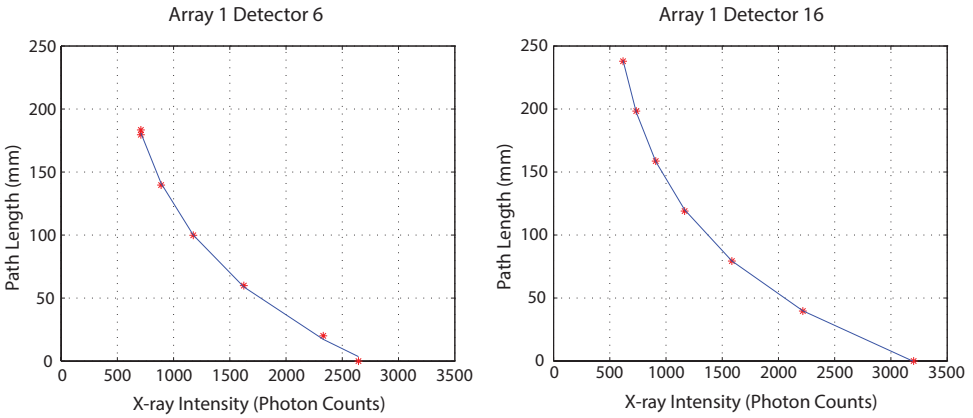

Figure 2.9: Examples of the calibration curves. The red stars are the measured data points. The blue lines are the fitted curves.

However, for a more perfect reconstruction, any possibility to reduce the error should be considered. In this dissertation, we test to fit the inversed function of Eq. 2.5:

$$l = C_{cal} ln \frac{B_{cal}}{I - A_{cal}}. \tag{2.6}$$

The error is significantly reduced by doing so. We test this for the same set of calibration data. The maximum error of l calculated from Eq. 2.6 is smaller than 3%. Figure 2.9 shows two examples of the calibration curves. The red stars are the measured data points. The blue lines are the fitted curves. These curves represent the functional relation between the measured I and input l accurately.

2.6. Data processing

Our purpose of applying the high speed X-ray tomographic system is to obtain the time resolved phase distribution. The simultaneous scanning is realized by multiple X-ray sources and detector arrays at different angles, by which a high temporal resolution is achieved. However, the price is the limited amount of data for each frame of scanning. Traditional tomographic reconstruction algorithms cannot get results accurate enough for this case. Advanced data processing is needed to convert the measured I to the phase distribution of the matter in the cross section of the bed. We develop specific data processing for different cases. Novel reconstruction techniques will be introduced in Chapter 3 and 4. For the measurement of a spouted bed, we develop a novel data processing by determining the spout size and position directly from raw data, which will be introduced in Chapter 5. For the measurement of the flow pattern below a downward micro-nozzle in chapter 6, we use a cross correlation to analyze the raw data, from which the periodical fluctuation of the gas phase can be accurately determined.

References

[1] M. Bartscher, U. Hilpert, J. Goebbels, G. Weidemann, Enhancement and proof of accuracy of industrial computed tomography (ct) measurements, Cirp Annals-Manufacturing Technology 56 (2007) 495–498. Bartscher, M. Hilpert, U. Goebbels, J. Weidemann, G.

[2] R. F. Mudde, J. Alles, T. H. J. J. van der Hagen, Feasibility study of a time-resolving x-ray tomographic system, Measurement Science & Technology 19 (2008). 8th International Symposium on Measurement Technology and Intelligent Instruments, Tohoku Univ, Sendai, Japan, Sep. 24-27, 2007.

[3] G. C. Brouwer, X-ray tomography of a fluidized bed, Master's thesis, Delft University of Technology, 2011.

[4] M. Nikl, Scintillation detectors for x-rays, Measurement Science & Technology 17 (2006) R37–R54. Nikl, M.

[5] J. Alles, R. F. Mudde, Beam hardening: Analytical considerations of the effective attenuation coefficient of x-ray tomography, Medical Physics 34 (2007) 2882–2889.

[6] B. E. Bjärngard, H. Shackford, Attenuation in highenergy x-ray beams, Medical Physics 21 (1994) 1069–1073.

[7] C. Ruth, P. M. Joseph, A comparison of beam-hardening artifacts in x-ray computerized tomography with gadolinium and iodine contrast agents, Medical Physics 22 (1995) 1977–1982.

[8] C. Kleinschmidt, Analytical considerations of beam- hardening in medical accelerator photon spectra, Medical Physics 26 (1999) 1995–1999.

[9] M. R. Millner, W. H. Payne, R. G. Waggener, W. D. McDavid, M. J. Dennis, V. J. Sank, Determination of effective energies in ct calibration, Medical Physics 5 (1978) 543–545.

[10] R. F. Mudde, Double x-ray tomography of a bubbling fluidized bed, Industrial & Engineering Chemistry Research 49 (2010) 5061–5065.

[11] R. F. Mudde, Time-resolved X-ray tomography of a fluidized bed, Powder Technology 199 (2010) 55–59.

[12] R. F. Mudde, Bubbles in a fluidized bed: A fast X-ray scanner, AIChE Journal 57 (2011) 2684–2690.

[13] G. Brouwer, E. Wagner, J. van Ommen, R. Mudde, Effects of pressure and fines content on bubble diameter in a fluidized bed studied using fast X-ray tomography, Chemical Engineering Journal 207–208 (2012) 711 – 717.

3

SART and AGA

The performance of two tomographic reconstruction algorithms, Simultaneous Algebraic Reconstruction Technique (SART) and Adaptive Genetic Algorithm (AGA), is evaluated based on synthetic data mimicking X-ray computed tomography of a bubbling fluidized bed. The simulations are based on a high speed X-ray tomography system, consisting of 3 X-ray sources and 32 detectors for each source. The comparison between SART and AGA is made for image resolutions ranging from 20 × 20 to 50 × 50 pixels, for the cases of 2 phantoms (artificial voids) and 3 phantoms in a 23 cm diameter column. The influence of noise on the reconstructions for both algorithms is also considered. It is found that AGA provides better reconstructions than SART at low resolutions. At high resolutions, the reconstruction quality is comparable, but the calculation times for AGA are much longer. AGA is better at finding the phantom position as it is less sensitive to measurement noise.

This chapter is based on the paper: X. Yang, J. R. van Ommen, R. F. Mudde, Comparison of genetic algorithm and algebraic reconstruction for x-ray tomography in bubbling fluidized beds, *Powder Technology* 2014, 253, 626–637.

3.1. The reconstruction problem

Image reconstruction is the main method to translate the X-ray data to the information of materials distribution for the tomographic measurements. Although virtually all reconstruction problems in CT are ill-posed, this problem in high-speed X-ray CT is particularly serious. In high speed X-ray CT, the number of data points depends on the number of detectors which is restricted by space and detector size. The traditional CT algorithms such as Filtered Back Projection (FBP) are seriously influenced by the ill-posed problem. It is easy to produce unknown errors when the order of the image matrix is much larger than the order of the raw data matrix [1]. The Simultaneous Algebraic Reconstruction Technique (SART) [2] was firstly applied to solve such a problem. Alternatively, the Genetic Algorithm (GA) [3] is introduced to tomographic image reconstruction [4–9]. Wu et al. ([6]) applied GA to fluidized beds. They reconstructed, amongst other cases, four bubbles that were simultaneously in the cross section of the bed. These bubbles were all of roughly the same size, i.e 20% of the bed diameter. They found that GA is superior over filtered linear back projection algorithms, regardless of the number of different viewing angles used for generating the data. The paper also discusses a strategy to refine the reconstruction mesh and showed that high spatial resolution can be reached with GA. Furthermore, they imposed a bonus in the GA algorithm on mutations towards grouped pixels of the same binary value, thereby incorporating the characteristic of a bubbling fluidized bed. This is similar to the so-called one-step-late algorithm that we use in SART.

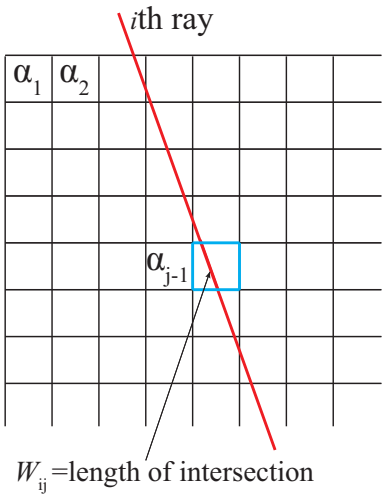

Figure 3.1: Definition of grid and W_{ij} matrix

Tomographic reconstruction is an inverse procedure for computing the solids fraction $\alpha(x, y)$ from the measured X-ray intensity. There are three basic steps.

- Convert the X-ray intensity I_m to solids path length l_s, i.e. the total amount of solids on the measuring line. l_s is usually referred to as the ray sum, $\tilde{p}$. In the real measurement, this procedure requires a calibration [10].
- Mesh the computing domain. We use a uniform meshing in this paper. In the reconstruction, we estimate the solids volume fraction in each pixel of the mesh. The values are stored in a vector (see Fig.3.1) rather than a matrix for computational reasons. When a given X-ray travels through the fluidized bed, it intersects a known length through each pixel of the mesh. All these lengths form the weighting matrix **W**.
- Solve the equation given below to obtain the solid fraction $\alpha_{x,y}$:

$$\tilde{p_i} = \sum_{j=1}^{N} W_{ij}\alpha_j \tag{3.1}$$

  where $\tilde{p_i}$ is the i^{th} ray sum, which is the fraction of the line traveled by the i^{th} beam occupied by solids; W_{ij} is the weighting factor for the j^{th} pixel crossed by the i^{th} beam; α_j is the solid fraction of the j^{th} pixel.

Here the reconstruction problem is thus finding a procedure for solving the linear equations Eq. (3.1). Note that the number of measured ray sums is only 3×32, being restricted by the hardware limitation. The required number of pixels for a reconstruction should be on the order of a thousand to obtain a reasonable resolution of the cross section. Obviously, the above is an ill-posed problem. It is common to treat the solving procedure as finding the best match between the data $\vec{\mathbf{p}}$ and the reconstructed $\mathbf{W}\cdot\vec{\alpha}$, i.e. the above is in essence an optimization problem.

Ill-posed problems either have no solution in the desired class, have many solutions, or the solution procedure is unstable (i.e. arbitrarily small errors in the measurement data may lead to large errors in the solutions) [11]. However, there are additional constrains for the reconstruction problems we consider. These are so-called regularization procedures. In the present case the reconstruction targets are the gas bubbles in the fluidized bed. These bubbles cannot be random single pixels somewhere in the cross section. They always manifest themselves as multiple concentrated pixels. This feature can guide the reconstruction towards the correct results. We will discuss this later as the one-step-late algorithm in SART and seeding the individuals without isolated pixels in AGA.

3.2. Simultaneous Algebraic Reconstruction Technique (SART)

The Simultaneous Algebraic Reconstruction Technique (SART) is an error-correcting procedure with step-by-step approximation [2]. It simultaneously applies to a pixel the average of the corrections generated by all rays, instead of updating the

pixels on a ray-by-ray basis sequentially. This is an improvement from the standard algebraic reconstruction technique (ART) [12] to reduce the accumulated error in the ray-by-ray iteration. The SART algorithm is written as:

$$\alpha_j^{n+1} = \alpha_j^n + \frac{1}{W_{+,j}} \sum_{i=1}^{N} \left(\frac{p_i - \tilde{p_i}}{W_{i,+}} W_{ij}\right) \tag{3.2}$$

where $W_{+,j} = \sum_{i=1}^{N} W_{ij}$, $W_{i,+} = \sum_{j=1}^{M} W_{ij}$, M is the total number of rays and N is the total number of pixels.

A so-called one-step-late algorithm is employed to reduce the pepper and salt noise in the images [13]. For this, an algorithm based on the median root function [14] is implemented in the SART algorithm used in this paper. To this end, an extra step is added to Eq. (3.2):

$$\alpha_{OSL,j}^{n+1} = \frac{1}{1 + \beta \frac{\alpha_{OSL,j}^n - Med(\alpha_{OSL,j}^n)}{Med(\alpha_{OSL,j}^n)}} \alpha_j^{n+1} \tag{3.3}$$

where α_j^n is the value of pixel j after the n^{th} SART step and $\alpha_{OSL,j}^n$ is the same after the n^{th} one-step-late correction. The median filter $Med(\alpha_j)$ replaces the value of the j^{th} pixel by the average pixel value contained in the j^{th} pixel neighborhood. Here we use a 3×3 neighborhood. β is the parameter to control the weight of the correction. It is set to 0.1 in this article as that is the number that gives best results in the tests.

3.3. Adaptive Genetic Algorithm (AGA)

3.3.1. Genetic Algorithm

The evolution of organisms can be seen as a natural optimization without any intricate mathematical theory. However, it is an efficient way to create all kinds of creatures that fit a complicated natural environment. Learning from the organisms' evolution, the Genetic Algorithm (GA) was developed by Holland [3]. In GA, there is a population of vectors, which are called chromosomes, to be randomly generated at the initial step. The chromosomes are also called individuals which are coded as the candidate solution. In our case the chromosomes are strings of 0's and 1's, representing the binary pixel values of an image. The individuals are reproduced with a mating and mutation procedure, that imitates the reproduction of organisms. For every generation of individuals during the reproduction, an object equation is used as the natural environment to select the most suitable individuals to reproduce. The reproducing repeats until an individual fits the object equation with a specific value, or a maximum number of generations is exceeded. GA is a global searching procedure for the fittest result in the solution domain.

In the traditional GA, the elements of the chromosomes are binary vectors related to the variables of the problem. It is, however, possible to use real numbers. The initialization step of GA is to start with initial guesses for the solution. This may be totally random or with more weight in certain areas of the solution domain. If it is totally random, the converging will be rather slow, but it strongly increases the probability that the whole computational domain is searched. If we have some pre-knowledge of the solution, the initial individuals can be tuned to the expected solution. It saves computing time, but has the risk of leading to a local optimization.

After the initialization, an object vector $\vec{V}_o$ is calculated from an object equation, which is the optimization problem we are going to solve. In this article, the object equation is

$$V_o = \sqrt{\sum_{i=1}^{M} (\tilde{p}_i - p_i^*)^2 / \tilde{p}_i{}^2} \tag{3.4}$$

in the above equation, $\tilde{p}_i$ is the set of measured ray sums. Each chromosome is a binary vector $\vec{\alpha}^*$; each element of this vector is a pixel of the reconstructed image. The corresponding ray sums p_i^* of each chromosome are calculated from $p_i^* = \sum_{j=1}^{N} W_{ij}\alpha_j^*$.

The range of $\vec{V}_o$ can show big changes from one generation to the next generation. For easier estimating a chromosome's fitness in the next steps, $\vec{V}_o$ is converted to a so-called fitness value $\vec{f}$. $\vec{f}$ is the scaled $\vec{V}_o$, but keeps relative value weighting of each elements.This procedure is called 'ranking'. In this article, we use a linear ranking method (Eq. (3.5)). The values of $\vec{V}_o$ range from 1×10^1 to 1×10^{-4}, and $\vec{f}$ always stays in the range from 0 to 2.

$$f_i = 2 \cdot \frac{Pos_i - 1}{Nind - 1} \tag{3.5}$$

where f_i is the fitness value of the i^{th} individual; Pos_i is the sorted position of the i^{th} individual, with the sorting based on V_o, from the smallest to the biggest; $Nind$ is the total individual number.

Selection is done after ranking. It follows the principle "survival of the fittest, elimination of the inferior". The individuals are sorted according to their f values. Individuals with a higher rank have a higher probability to be selected as the parents for the next generation.

The next step is the so-called crossover. Here, we exchange part of the chromosome between two parents. The parents are the couple of individuals selected from the ranked population of the previous generation. There are different crossover methods such as single point crossover, two points crossover, scattering crossover,

etc. [15]. We have tested these traditional crossover methods in our reconstruction algorithms. The difference of convergence rate and computing accuracy is not obvious. Especially, they converge very easily to a local optimum. An adaptive crossover [16] is proposed in the literature to improve this. It shows more artificial intelligence of searching the computing domain and improves the accuracy substantially. Therefore, we adopted this approach.

The final step is mutation: a random change of some parts of the chromosome. For the binary strings of chromosomes, it can be done simply by reversing a binary number. There is also an adaptive mutation together with the adaptive crossover for preventing premature convergence [16]. We use adaptive crossover and adaptive mutation together in our GA based tomographic reconstruction. This type of GA is called Adaptive Genetic Algorithm (AGA).

3.3.2. Adaptive Crossover and Mutation

In scattering crossover, the crossover probability P_c influences the genes' exchange rate between two parents. P_c is a value between 0 to 1. When we do the crossover, we randomly generate a number between 0 to 1 for each position of the chromosome. If this random number is smaller than P_c, we exchange the genes from the parents in this position. Otherwise, we keep the gene as it was. Fig.3.2 illustrates this procedure and shows the offspring produced after the exchange of genes between two parents with given P_c.

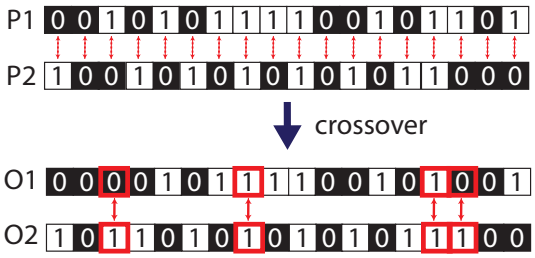

Figure 3.2: The illustration of crossover. P1 and P2 represent the chomosome of parent 1 and parent 2. O1 and O2 represent the chromosome of offspring 1 and offspring 2.

The mutation probability P_m is defined similarly. For each gene of the chromosome, when the randomly generated number is larger than P_m, we reverse the gene. Otherwise, we keep it.

In conventional GA, P_c and P_m keep the same value for the entire calculation procedure. These values have an important influence on the convergence and individual diversity. It is difficult to find the right balance between convergence and individual diversity for GA. High individual diversity causes slow convergence to the required object fitness value. In contrast, low individual diversity leads to the calculation easily dropping into a local optimum, which is called prematurity. In our tests for

the different crossover and mutation methods, prematurity could not be avoided when using constant P_c and P_m.

The prematurity can be partly removed by using adaptive P_c and P_m. The idea comes from the paper of Srinivas and Patnaik [16]. We further developed the method to make it more efficient for tomographic reconstruction. In the Adaptive Genetic Algorithm (AGA), the P_c and P_m values are adjusted in each generation and for each parent as given below:

$$P_c = \begin{cases} P_{c1} - \dfrac{(P_{c1} - P_{c2})(f^{'} - f_{avg})}{f_{max} - f_{avg}}, & f^{'} \geq f_{avg} \\ P_{c1}, & f^{'} < f_{avg} \end{cases} \tag{3.6}$$

and for mutation,

$$P_m = \begin{cases} P_{m1} - \dfrac{(P_{m1} - P_{m2})(f_{max} - f)}{f_{max} - f_{avg}}, & f \geq f_{avg} \\ P_{m1}, & f < f_{avg} \end{cases} \tag{3.7}$$

where $f^{'}$ is the maximum fitness value between two parents in crossover; f_{avg} is the average fitness value of all individuals in one generation; f_{max} is the maximum fitness value in one generation; P_{c1} and P_{c2} are constant parameter of P_c in crossover, which are modified in every generation based on the so-called population diversity (Div); f is the fitness value of the individual for mutation; P_{m1} and P_{m2} are constant parameter of P_m in mutation, which are also modified in every generation based on the Div-value. Div is calculated as:

$$Div = \sum_{i=1}^{N_{ind}} \frac{|V_{o,i} - V_{o,mean}|}{V_{o,max} - V_{o,min}} \tag{3.8}$$

where N_{ind} is the number of individuals; $V_{o,i}$ is the i^{th} individual's object value; $V_{o,mean}$ is the averaged object value in one generation; $V_{o,max}$ is the maximum object value in one generation; $V_{o,min}$ is the minimum object value in one generation. We adjust the constants P_{c1} and P_{c2} for each new generations according to

$$\begin{cases} P_{c1} = C_1 - \sqrt{Div/C_2} \\ P_{c2} = C_3 + \sqrt{Div/C_4} \end{cases} \tag{3.9}$$

and similarly P_{m1} and P_{m2} for mutation,

$$\begin{cases} P_{m1} = M_1 - \sqrt{Div/M_2} \\ P_{m2} = M_3 + \sqrt{Div/M_4} \end{cases} \tag{3.10}$$

where $C_1 \cdots C_4$ and $M_1 \cdots M_4$ are constant values that we found from trial and error.

The principle of Eq. (3.6) and Eq. (3.7) is to use different P_c and P_m values for parents with different fitness values. P_{c1} and P_{m1} are bigger than P_{c2} and P_{m2}. In crossover, when the parents have a fitness value higher than the average value of all individuals, we use a lower P_c value to change fewer genes in their offsprings. Otherwise, we do the opposite. When we do the mutation for the offsprings, the idea is similar.

The values of P_{c1}, P_{c2}, P_{m1} and P_{m2} are chosen by testing different values in different cases. The population diversity is defined to compare the object value distribution in each generation. It is used to monitor whether the object value V_o becomes uniform or diversifies. If the population diversity is outside an ideal range for most efficient convergence, there will be penalties for P_{c1}, P_{c2}, P_{m1} and P_{m2}. These penalty values are based on the population diversity value (Eq. (3.9), Eq. (3.10)).

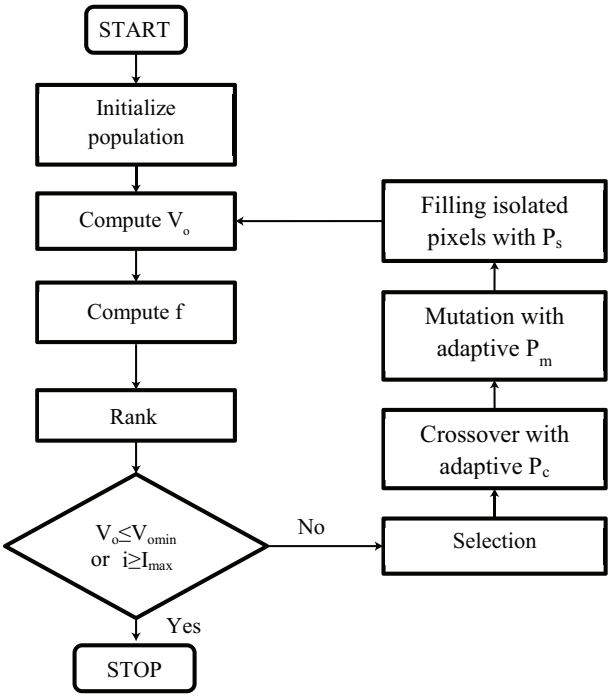

Figure 3.3: Flowchart of AGA

3.3.3. Seeding the Individuals without Isolated Pixels

Mera et al. [17] found that GA cannot be used to regularize an ill-posed problem if the ill-posedness is not dealt with by another method. However, if there is additional information about the solution available, GA can be particularly useful for inverse problems. In fluidized beds, the bubbles' shape in a cross section should not

be very tiny voids randomly distributed everywhere. They tend to be concentrated.

To incorporate this, we add a function for GA that puts a penalty on pepper and salt pixels. This function is only applied once for every 5 generations and changes part of the individuals with the probability P_s. It does not change the evolutionary procedure artificially, but only seeds in the individuals more fitting the physics of fluidized bed. With low probability to manipulate part of the individuals, the majority of individuals are still reproduced naturally under the fitness law. This can avoid some problems such as pixels concentrated to the boundary circle, or producing phantoms that do not exist in reality. The expression we use the P_s is:

$$P_s = 1 - \frac{C_s}{\sqrt{N_{gen}}} \tag{3.11}$$

where C_s is a constant parameter from tests; N_{gen} is the generation number.

In this function, we check each 3×3 pixels matrix in the reconstructed images. If there is no neighbor with the same value of the center pixel (i.e. element $(2, 2)$ in the 3×3 matrix), the center pixel is considered as an isolated pixel. We define the probability P_s (see Eq. (3.11)) to clean the isolated pixels. For each individual in one generation, if the random generated number is bigger than P_s, we change the isolated pixel value to be the same as its neighborhood for this individual. Otherwise, we do nothing. Instead of artificially smoothing it in the final result, we give GA the possibility for the isolated pixels in the reconstructed images. Whether the isolated pixels are 'pepper and salt' noise or small phantoms, depends on whether it can survive with its object value, not on the final artificial decision. P_s decreases when the generation number increases. This helps to speed up the convergence.

Figure 3.4 shows the improvement of the convergence for the modified AGA compared with GA. We used synthetic data to mimic two phantoms in the cross section of a fluidized bed. The reconstruction of AGA is given in Fig. 3.4 (a) (black pixels) together with the real phantoms (red circles). For GA (Fig. 3.4 (b)), the object value (V_o) of the 'Best' individual converges very fast prior to generation 100. From generation 100 to 400, it becomes very slow. After generation 400, the convergence almost stops. The gap between the 'Best' V_o and the 'Mean' V_o becomes bigger and bigger, which means the 'Best' individual separates from the average level of other individuals. When this happens, the 'Best' individual cannot be easily influenced by others, because it has the dominant advantage. The convergence sometimes stops at this point, even though there is still significant deviation from the true objects. This is so-called premature convergence for GA [18]. The situation is improved in AGA (Fig. 3.4 (c)). The 'Best' V_o converge to 0 at generation 240. During the whole convergence, the 'Best' V_o converges relatively uniform. The 'Best' and the 'Mean' also keeps a relatively uniform gap, which means there are effective interactions between the 'Best' individual and the others for all the generations. AGA shows faster convergence than simple GA and also partly solves the premature convergence of simple GA.

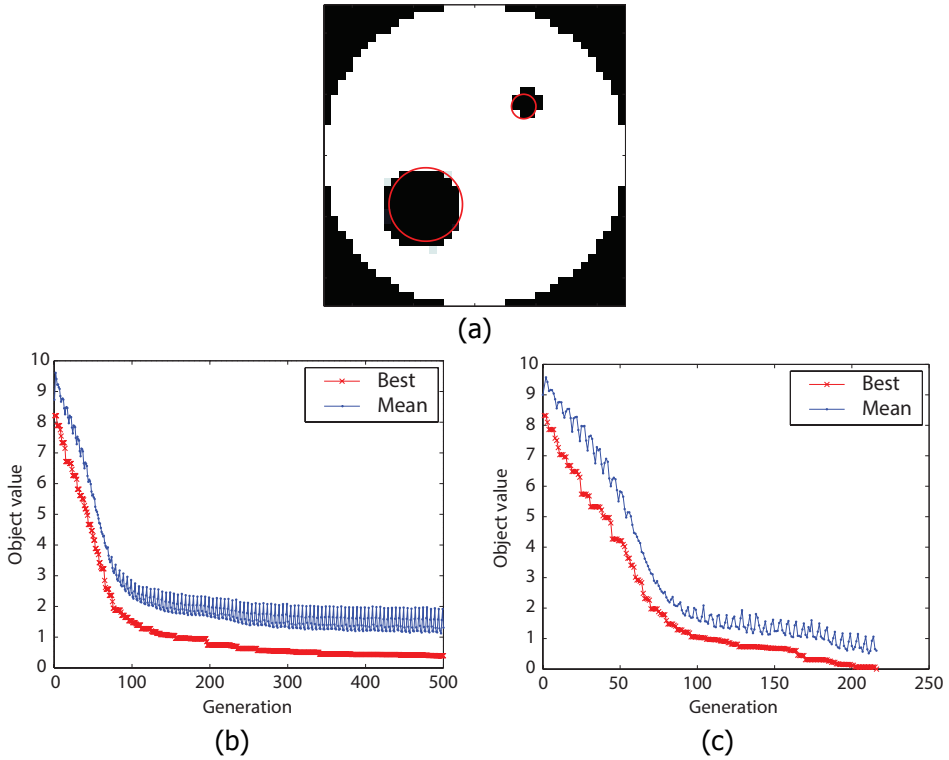

Figure 3.4: The convergence of the object values (V_o). (a) Reconstruction result by using AGA. The red circles are the objective phantoms. The blue circle is the wall of the fluidized bed. The mesh is 40×40 for a diameter of 24 cm cross section; (b) Convergence curve by using simple GA with smoothing isolated noisy pixels. The convergence almost stop after generation 400; (c) Convergence curve by using AGA with smoothing isolated noisy pixels. The 'Best' convergence to 0 at generation 220. The 'Best' is the smallest object value, and the 'Mean' is the average object value, from all the individuals in each generation.

3.4. Results & Discussion

To compare the capability and accuracy of SART and AGA under the same conditions, a comparison has been made using the same reconstruction program, with only a different core reconstruction algorithm. We use circular phantoms as the object to be reconstructed, because these resemble the bubble shape in a cross section of the fluidized bed.

A criterion known as Structural Similarity (SSIM) [19] is employed to estimate the quality of the reconstructed images. SSIM is a combination of luminance comparison, contrast comparison and structure comparison. It corresponds well to the human visual perception. Images are more similar if their SSIM is closer to 1. The pixels' value range of SART is 0 to 1. We threshold the results of SART to binary

images, which makes it comparable with AGA. On the other hand, different AGA runs for the same measured data produce different images for which it is not a priori clear which one represents best reality: all we know is which one has the smallest value of the objective function. Therefore, we also look at the spread in the AGA results obtained from the same data. We will show below the best reconstruction (in the sense of highest fitness value), the worst reconstruction and an average of ten runs, which produces a grey value image like SART does. As far as we know, test like these have not been reported in literature.

For SART, we set the maximum number of iterations to 1500 [20] and the tolerance of error to 10^{-8}. All the cases of AGA are reconstructed 10 times to evaluate the influence of random results. Some important parameters of AGA are given in Table 1.

Table 3.1: Important parameters for AGA

Parameter	Value
N_{ind}	600
I_{max}	2000
V_{omin}	1×10^{-6}
C_1	1
C_2	6×10^4
C_3	0.3
C_4	6000
M_1	0.3
M_2	8000
M_3	0.005
M_4	6×10^6
C_s	0.5

All the parameters are the optimized values for producing the best results in both SART and AGA. SART will always produce the same results for the same inputs. However, AGA is producing varying results for the same input at high resolution reconstructions. So, the reproducibility and application consideration of AGA will also be considered.

3.4.1. Reproducibility of AGA

For reconstruction with low pixel numbers and low complexity, such as meshes of 20×20 and 30×30 pixels, and only 2 or 3 phantoms present, AGA is capable of reconstructing exactly the input image. When the mesh size becomes larger, different runs using the same input data produce different results as is illustrated in Fig. 3.5 and Fig. 3.6. In our case, we find this for meshes of 40×40 pixels and higher. This problem has not been reported in previous studies which apply Genetic Algorithms to do tomographic reconstruction [4–9]. However, it was reported for

a different application of a Genetic Algorithm [21].

In the coming comparison with SART, we repeat each case of AGA 10 times. Both the best results and average results are presented. We quantify the agreement between reconstruction images and the inputs using the SSIM value. While this is possible in our study, it is not possible in the reconstruction of experimental data when the real situation is unknown. We will further discuss this in section 3.4.6.

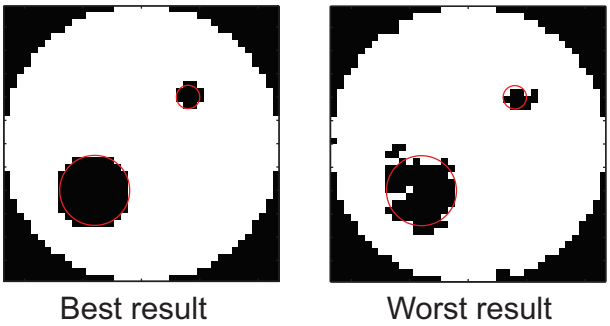

Figure 3.5: The best result and worst result, mesh 40×40, 2 phantoms, with AGA. The red circles indicate the true phantom locations.

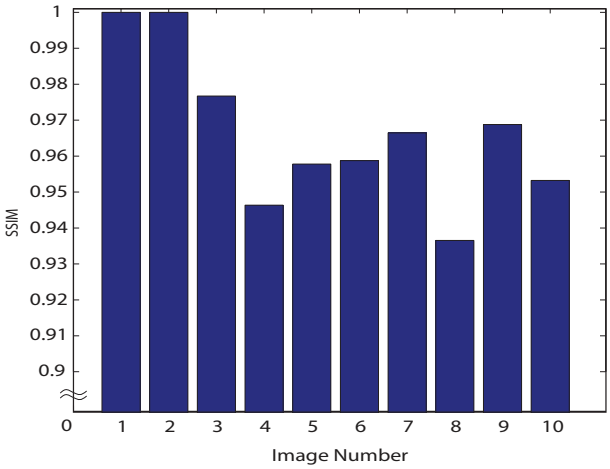

Figure 3.6: The SSIM value for 10 different reconstructions with AGA, on a 40×40 mesh, for the same computing conditions.

3.4.2. Threshold of SART

The SART reconstruction produces grey value images. However, for a bubbling fluidized bed, binary images are sufficient to express the difference between the dense phase and the gas voids. For an easy comparison with AGA, we use thresholding to convert the grey value images to binary images. The grey values (indicated by a

value between 0 and 1) are converted to black (0) or white (1), depending whether they are below or above the threshold, respectively. We investigated the influence of the threshold by varying its value, and comparing the outcome both with the unthresholded reconstructed image and with the input image (see Fig. 3.7).

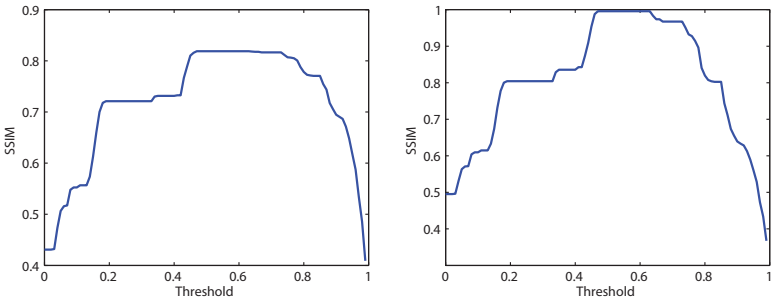

Figure 3.7: The SSIM values when using different threshold for SART: (a) Comparing with the original result; (b) Comparing with the input image. 3 phantoms reconstruction. The mesh is 40 × 40.

Figure 3.7 shows that a threshold around 0.6 yields results that are closest to the unthresholded results and to the input. The effect of using this threshold value is shown in Figure 3.8: it leads to removal of the grey areas (so-called "ghosts") that we frequently find when reconstructing using SART. Removing of the ghosts using the thresholding gives a good representation of the voids.

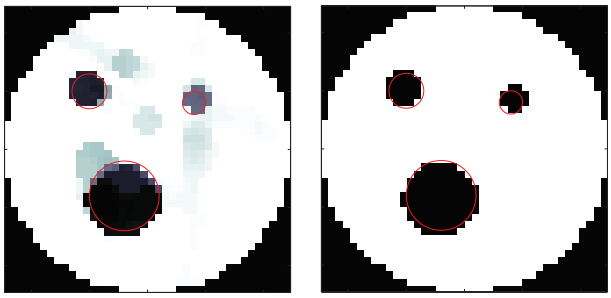

Figure 3.8: The reconstruction result of SART: (a) without threshold; (b) with threshold. The reconstruction for 3 phantoms. Red circles indicate the input phantoms. The mesh is 40 × 40.

3.4.3. Two phantoms reconstruction

We consider the case with two phantoms with a diameter of 2 cm and 6 cm in the fluidized bed. Again synthetic X-ray data are generated. Both the AGA and SART algorithm are employed to reconstruct the images from the mimicked signals. As is shown in Fig. 3.9, when meshes are smaller than 50×50 pixels, both the best and

average results of AGA perfectly match the object shape. For a mesh of 50×50, the position is reconstructed correctly, but the phantoms are out of shape and noisy pixels outside the phantoms appear.

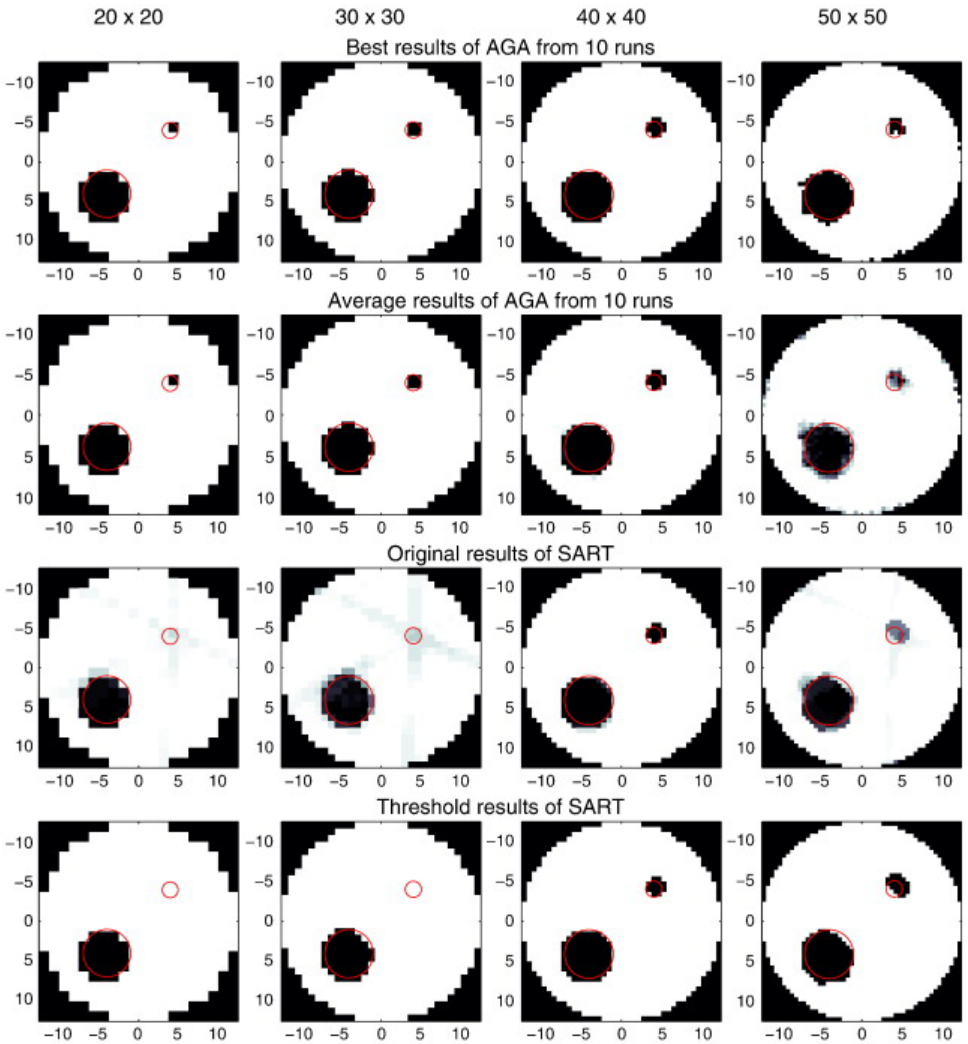

Figure 3.9: Reconstruction results for 2 phantoms with AGA and SART; the mesh ranges from 20×20 to 50×50 pixels. The red circles indicate the true position and shape of the phantoms.

SART only gives a close to perfect shape when the mesh is 40×40. Without prior knowledge, the small phantom (2 cm diameter) cannot be found from the reconstructed images for the meshes of 20×20 and 30×30. With the threshold, the mirrored shadows disappear. The phantoms boundaries become more distinct, but

the small phantom has disappeared in the coarse meshes.

In General, AGA shows its advantage for coarse meshes. It is capable of finding the small phantom, even when this phantom is about the size of two pixels.

In Fig. 3.10, the SSIM values are also plotted to compare the quality of the reconstructions. It is shown that AGA performs better than SART when the meshes are 20×20 and 30×30. Both methods perform nearly perfect for a mesh of 40×40. When the mesh is further refined to 50×50, both methods yield a deteriorated reconstruction, and AGA performs slightly worse in that case.

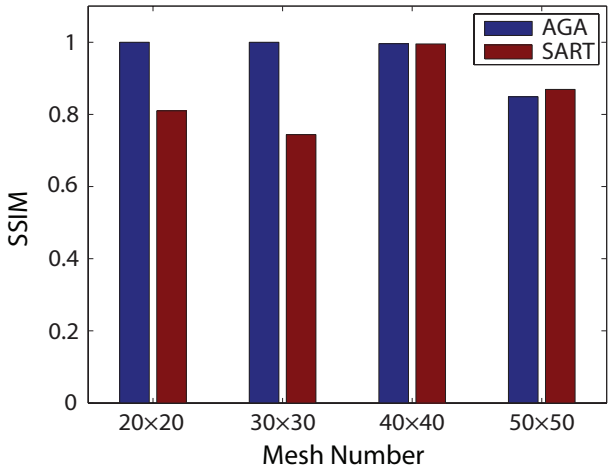

Figure 3.10: The SSIM values of 2 phantoms reconstruction of AGA and SART, the mesh ranges from 20×20 to 50×50 pixels. The SSIM values of AGA are the averaged values over 10 runs. The SSIM values of SART are non-thresholded cases.

3.4.4. Three phantoms reconstruction

To increase the complexity of the image, we simulated three phantoms. These also have a circular shape but with diameters of 2 cm, 4 cm and 6 cm, respectively. The results are given in Fig. 3.11.

For AGA, the best results from 10 runs perfectly fit the inputs from mesh 20×20 to 40×40. It indicates the correct position of all phantoms for a 50×50 mesh, but the shapes are inaccurate. With the average from 10 runs, the images becomes blurred and mirrored shadows appear in the meshes of 40×40 and 50×50. Compared with the situation of 2 phantoms, the accuracy decreases. However, AGA always recognizes the correct position of the phantoms, even for the smallest one.

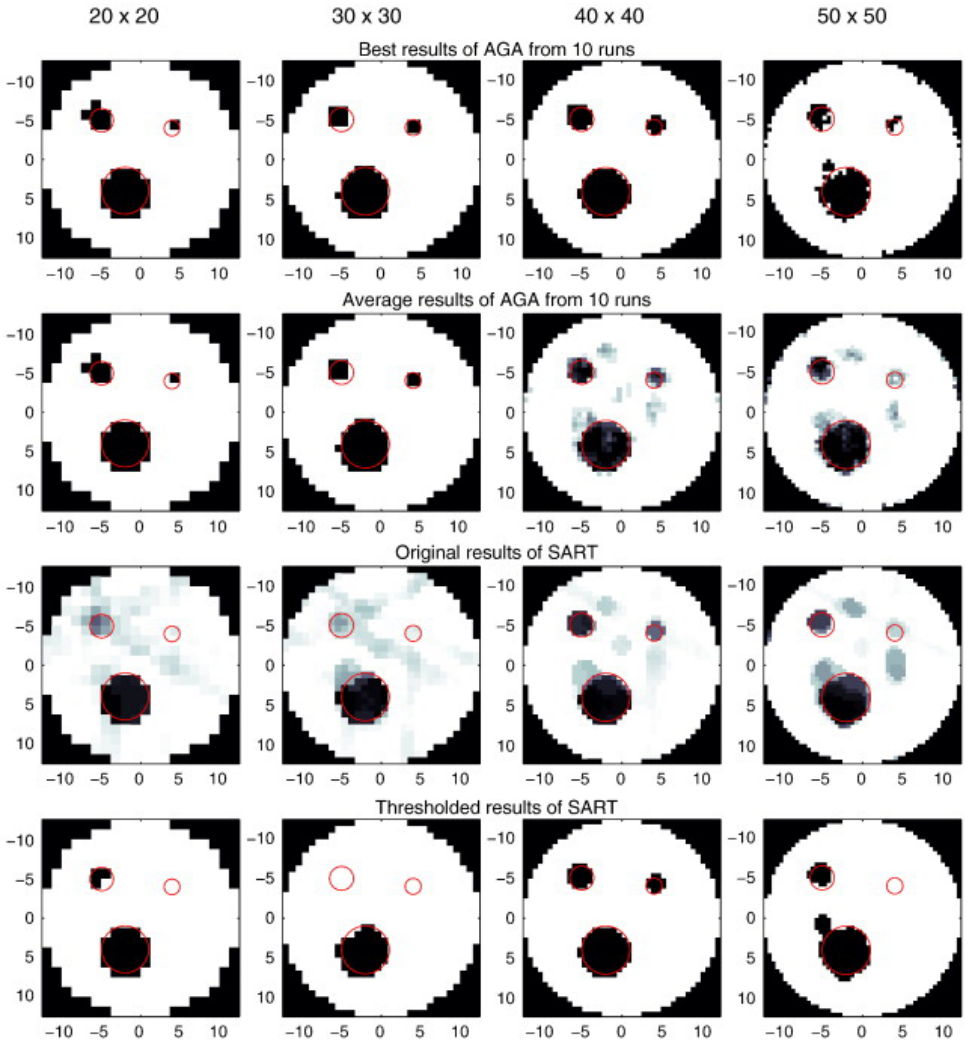

Figure 3.11: Reconstruction results for 3 phantoms with AGA and SART, the mesh ranges from 20×20 to 50×50 pixels. The red circles indicate the true shape and position of the phantoms.

For SART, we always have noisy shadows in the images. Like for the situation with 2 phantoms, SART also obtains the best result on a mesh of 40×40 for 3 phantoms. For meshes other than 40×40, the small phantoms with diameters of 2 cm and 4 cm are poorly reconstructed. With the threshold, the phantoms in the mesh 40×40 are perfectly determined. However, the smallest phantom is difficult to find in the reconstructions: it really depends on the mesh size whether or not we find it back.

In the SSIM value plot (Fig. 3.12), the SSIM values change similar as in the 2 phantoms reconstruction. AGA performs better than SART when the meshes are 20×20

and 30×30. The quality of reconstruction decreases when the number of pixels increases in AGA. For SART, it shows the best reconstruction when the mesh is 40×40.

In the work of Wu et al. [6], 4 phantoms are successfully reconstructed with GA in '3-angle' system, which is similar to our system. However, these phantoms are all similar in size and relatively big. In their paper, the authors did not discuss the reproducibility, which is of prime importance for practical applications.

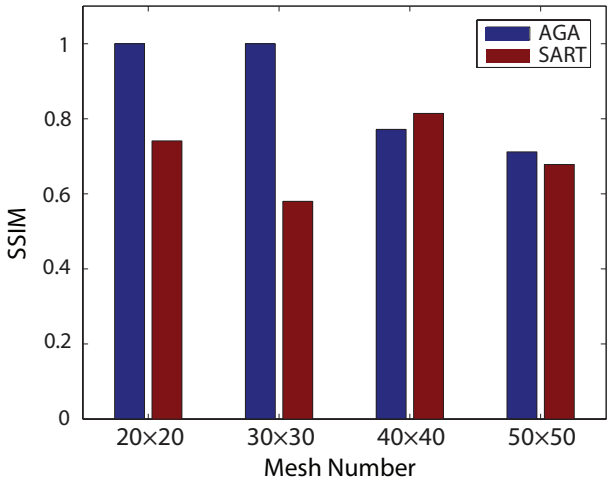

Figure 3.12: The SSIM values of 3 phantoms reconstruction of AGA and SART, the mesh ranges from 20×20 to 50×50 pixels. The SSIM values of AGA are the averaged values over 10 runs. The SSIM values of SART are non-thresholded cases.

3.4.5. Computing time

Table 3.2: The computing times (second) of AGA and SART

Method \ Grid	20×20	30×30	40×40	50×50
2 Phantoms				
SART	16	179	201	407
AGA	35	202	2726	8450
3 Phantoms				
SART	21	191	211	422
AGA	40	1758	6884	16600

The simulations were done on the same computer with a Xeon Quad Core 2.8GHz processor. Table 3.2 shows the CPU times in seconds. The computing time for AGA is the average value for 10 runs of the same case.

It is clear that AGA consumes much more time than SART and the computing time increases significantly when the mesh number increases. In a real experiment on a fluidized bed, the measuring time is easily minutes, providing information for more than 10^5 images. We have not yet optimized AGA for computational speed. But it is clear that the large increase of the computing time with increasing mesh size should be considered when applying the algorithms. As Table 3.2 shows, AGA strongly slows down for large meshes. However, Genetic Algorithms are very suitable for parallel computing [22]. Hence, there is large potential to substantially speed up the AGA reconstructions.

3.4.6. The influence of noise on AGA and SART

In real measurements, system noise is unavoidable. Noise can lead to unexpected errors in the final results. We add random noise to the ideal signal to simulate the signal as real as possible. The ratio between the noise amplitude and the original signal is called the noise fraction. The noise fraction of real data is 0.01 to 0.1 approximately. Synthetic data with a noise fraction of 0.05 is tested and compared with the ideal data. The reconstructions were done by both AGA and SART. For AGA, we selected the best SSIM value from 10 reconstructions.

From the reconstruction results of Fig. 3.13, we can still find the 3 phantoms in their positions with AGA, but also 2 rather small ones that should not be there. However, the image quality reduced a lot for SART. The SSIM value's ratios between the reconstruction with noise and without noise are shown in Fig. 3.14 and Fig. 3.15. A higher ratio indicates a higher similarity and less influence of noise. All these ratios of AGA are higher than SART. AGA was performing much better than SART for 30×30 pixels. When the mesh number increases, the noise influences AGA more seriously.

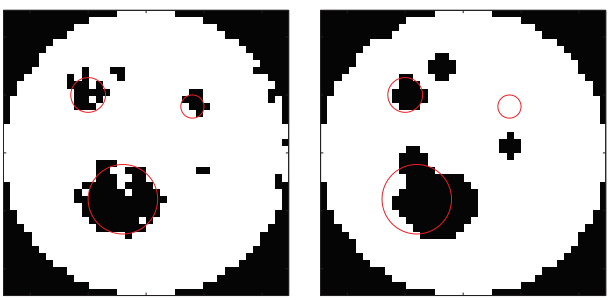

Figure 3.13: Reconstruction results for 3 phantoms with AGA and SART, noise fraction 0.05, mesh 40×40. The red circles indicate the true shape and position of the phantoms.

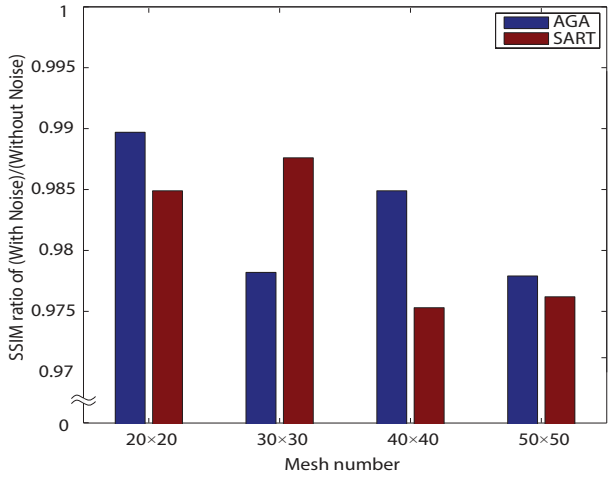

Figure 3.14: The SSIM ratio between the reconstruction with 0.05 noise and without noise, 2 phantoms for meshes of 20 ×20 to 50×50 pixels, AGA and SART.

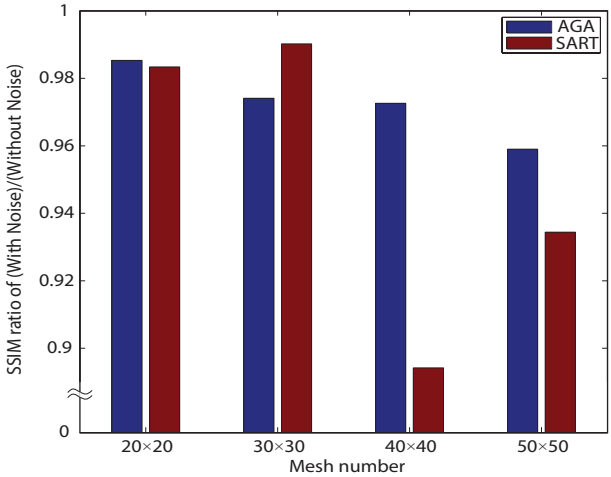

Figure 3.15: The SSIM ratio between the reconstruction with 0.05 noise and without noise, 3 phantoms, the mesh number from 20×20 to 50×50, AGA and SART.

3.4.7. Practical considerations of AGA

Although AGA shows the potential to improve the reconstruction accuracy, the poor reproducibility for refined meshes (40×40 and 50×50 in our case) is a serious drawback when applying it to real measurement data. It is not possible to estimate the influence of noise on the results, making it difficult to compare the results. The most direct solution to reduce the variability of the results is to repeat the recon-

struction for the same case, and subsequently average them.

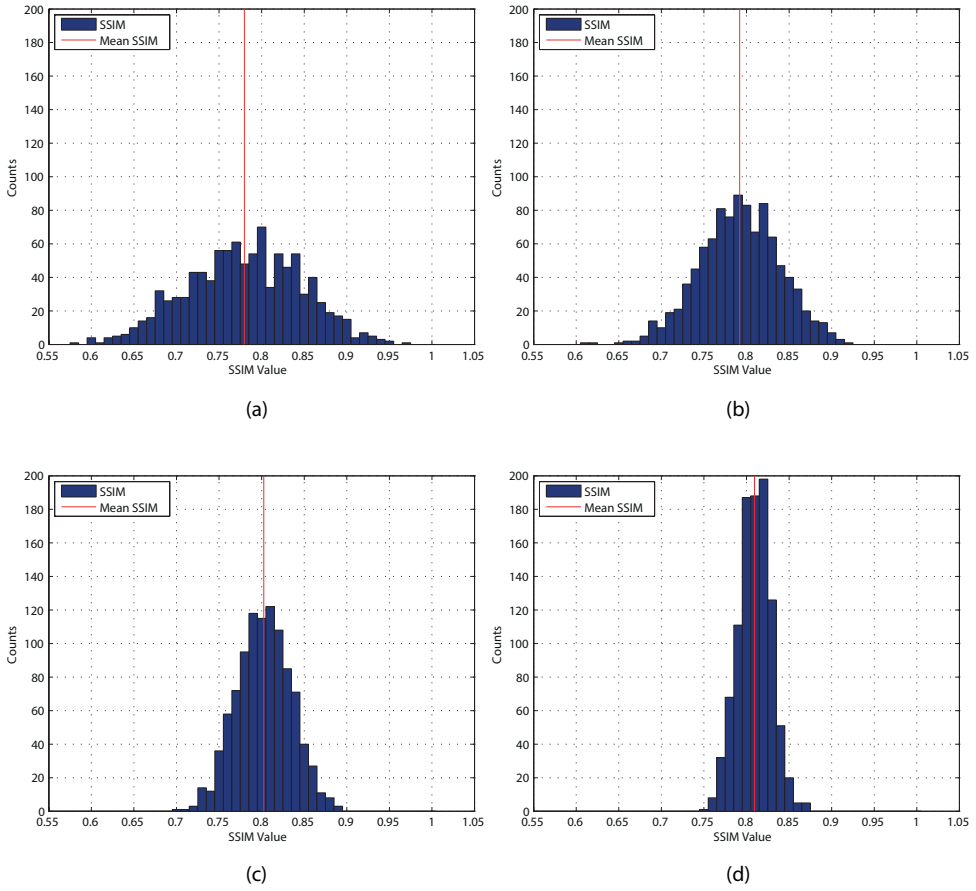

Figure 3.16: SSIM values distribution of averaged results for different amount of samples to be averaged. All the samples are done in the case of 3 phantoms, mesh 40×40. (a) 5 samples; (b) 10 samples; (c) 20 samples; (d) 40 samples.

To estimate the improvement when averaging over more reconstructed images, we calculate the distribution of averaged results according to the following steps:

- Repeat AGA reconstruction for the case (3 phantoms, mesh 40×40) 100 times. Store the final result of each reconstruction in an array $Recon_i$;
- Randomly select n samples from this array for a different value of n, e.g. 5, 10, 20 and 40, and compute the averaged images from the selected samples;
- Calculate the SSIM values of the averaged images. The SSIM values are calculated between the initial input images and the averaged images;

- Repeat step 2 and step 3 for 1000 times to plot the statistic histogram.

As is shown in Fig. 3.16, the SSIM values are widely distributed between 0.58 to 0.97 for the tests of averaging samples ($n = 5$). When we increase the sample size for averaging to $n = 40$, the SSIM concentrates between 0.75 to 0.87. Although it is not possible to obtain a fixed result from averaging the random results of AGA, the variation can be narrowed to a small range by averaging over a large number. In practice, we can repeat the same AGA reconstruction for a large number of times (more than 40 in case of mesh 40×40), then we can obtain an averaged result from these repeated reconstruction. This result can be stable enough for analyzing the real measurement data. However, this procedure will involve very long computational time.

Another approach for applying AGA to real measurement data is to combine it with SART. AGA can reconstruct the images with good accuracy for coarse meshes such as 20×20 and 30×30, while keeping the computational time acceptable. In this case, we can take advantage of the strength of AGA in finding small objects. We can use these results as the initial guesses for SART to do the reconstruction on a refined mesh.

3.4.8. Reconstructing experimental data

We will demonstrate the practical application of SART and AGA using experimental data. This data is obtained by placing two empty cylinders in a packed bed. The column containing the packed bed is a 24 cm inner-diameter Perspex tube. The cylinders have an inner-diameter of 36 and 58 mm, respectively, and a 2 mm Perspex wall. The bed consists of polystyrene particles with a diameter of 0.56 mm. A horizontal cross-section of the voids created with the empty cylinders is measured using the set-up depicted in Fig. 2.2. The reconstruction is carried out with AGA, SART and a combination of AGA and SART (see Fig. 3.17).

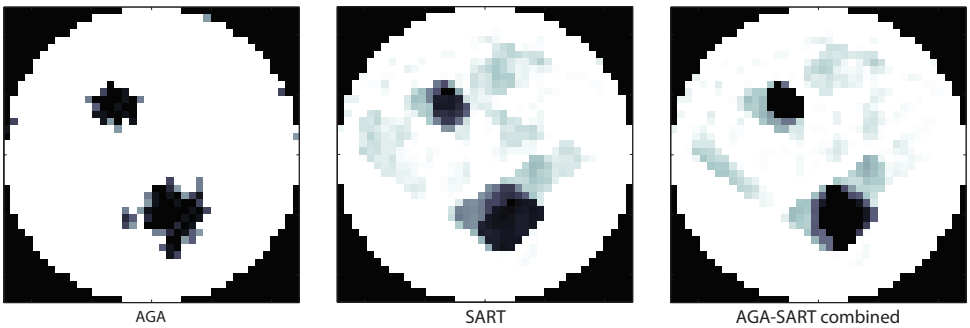

Figure 3.17: Reconstruction results for experimental data with 2 phantoms. The mesh is 40×40.

The results from AGA is the average of 10 reconstruction runs for the same measurement data. The shape of the phantom is not very accurate, and there are some noisy pixels outside the phantom region. However, their positions are correct and the sizes are close to the input. SART also succeeds in finding the voids. The size is correct, and the shape is closer to that of the input. However, there are also ghosts: dark grey areas in dense phase regions. In addition, we applied a reconstruction in which the AGA results were used as the initial guess for SART. This combination shows an improvement compared to the results for SART only: the grey area have decreased in size and darkness.

A more quantitative way to assess the reconstruction outcomes is to plot the histograms of the obtained grey values (see Fig. 3.18). Although the results for a single AGA reconstruction are binary, the averaging over 10 runs leads to a distribution of the grey values. However, most non-white pixels are either black or dark grey (pixel value 0.2). The histogram for SART shows that very few pixels are really black: there is a wide distribution of the grey values, which will make it difficult to choose a proper value for thresholding. The combination of AGA and SART shows a clear improvement: much more pixels are truly black. As a consequence much fewer grey pixels are found, especially in the intermediate range, making thresholding much easier. This demonstrates that combining AGA and SART shows good potential for improving the reconstruction quality.

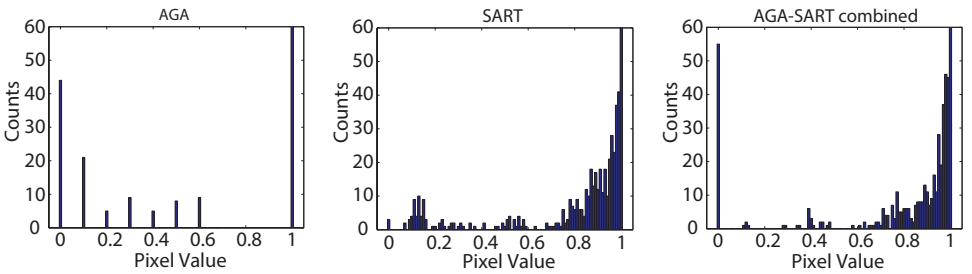

Figure 3.18: Histograms of the pixel values for reconstructed images shown in Fig. 17. Pixel value 0 indicates black and 1 is white. The value for white exceeds 60, but the vertical axis is limited to clearly show all grey values.

The measurement accuracy can be improved by using different reconstruction algorithms. However, the spatial resolution is still limited for measuring complicated bubbling system, especially if there are many small bubbles in one cross section. Also, if the bubbles are closer together than our resolution, they will be reconstructed as one object. The situation can be improved by increasing the number of X-ray sources and detectors.

3.5. Conclusion

The reconstruction of images for X-ray tomography is challenging, since it is an ill-posed problem: the number of grid cells is much higher that the number of data points. In this study, we compared the Simultaneous Algebraic Reconstruction Technique (SART) and an Adaptive Genetic Algorithm (AGA) for this purpose using artificial data for a bubbling fluidized bed. AGA performs much better than SART for low spatial resolution reconstructions (20×20 and 30×30 pixels). The accuracy of AGA goes down for fine meshes (50×50), and the computing time strongly increases. There is not clear trend for SART when the resolution increases. In the cases we tested in this paper, we found always the best performance for a mesh of 40×40 pixels. However, this is different for other cases with different number and sizes of phantoms.

The presence of noise strongly influences SART; AGA is less sensitive to noise. The disadvantage of AGA is its variation in results. Varying results were obtained for the same case when reconstruction images with higher spatial resolutions (40×40 and up in our case). This needs further improvement before AGA can be successfully applied to real measurement data. A next step could be to couple AGA with SART: coarse-mesh AGA reconstructions can serve as the initial guess for SART reconstruction on a refined mesh.

References

[1] F. Natterer, The Mathematics of Computerized Tomography, John Wiley & Sons, pp. 85–118.

[2] A. Andersen, A. Kak, Simultaneous Algebraic Reconstruction Technique (SART): A superior implementation of the ART algorithm, Ultrasonic Imaging 6 (1984) 81 – 94.

[3] J. H. Holland, Genetic algorithms, Scientific American 267 (1992) 66–72.

[4] K. D. Kihm, K. Okamoto, D. Tsuru, H. S. Ko, Adoption of a genetic algorithm (GA) for tomographic reconstruction of line-of-sight optical images, Experiments in Fluids 22 (1996) 137–143.

[5] M. Venere, H. Liao, A. Clausse, A genetic algorithm for adaptive tomography of elliptical objects, Signal Processing Letters, IEEE 7 (2000) 176–178.

[6] C. Wu, Y. Cheng, Y. Ding, F. Wei, Y. Jin, A novel x-ray computed tomography method for fast measurement of multiphase flow, Chemical Engineering Science 62 (2007) 4325 – 4335.

[7] C. Valenti, A genetic algorithm for discrete tomography reconstruction, Genetic Programming and Evolvable Machines 9 (2008) 85–96.

[8] M. Abdoli, M. R. Ay, A. Ahmadian, R. Dierckx, H. Zaidi, Reduction of Dental Filling Metallic Artifacts in CT-based Attenuation Correction of PET Sata Using Weighted Virtual Sinograms Optimized by a Genetic Algorithm, Medical Physics 37 (2010) 6166–6177.

[9] V. Di Gesu, G. Lo Bosco, F. Millonzi, C. Valenti, A memetic approach to discrete tomography from noisy projections, Pattern Recognition 43 (2010) 3073–3082.

[10] R. F. Mudde, Time-resolved X-ray tomography of a fluidized bed, Powder Technology 199 (2010) 55–59.

[11] S. I. Kabanikhin, Definitions and examples of inverse and ill-posed problems, Journal of Inverse and Ill-Posed Problems 16 (2008) 317–357.

[12] G. T. Herman, A. Lent, S. W. Rowland, ART: Mathematics and applications: A report on the mathematical foundations and on the applicability to real data of the algebraic reconstruction techniques, Journal of Theoretical Biology 42 (1973) 1 – 32.

[13] P. Green, Bayesian reconstructions from emission tomography data using a modified EM algorithm, IEEE Transactions on Medical Imaging 9 (1990) 84–93.

[14] S. Alenius, U. Ruotsalainen, Bayesian image reconstruction for emission tomography based on median root prior, European Journal of Nuclear Medicine and Molecular Imaging 24 (1997) 258–265.

[15] D. Whiyley, A genetic algorithm tutorial, Statistics and Computing 4 (1994) 65–85.

[16] M. Srinivas, L. M. Patnaik, Adaptive probabilities of crossover and mutation in genetic algorithms, IEEE Transactions on Systems Man and Cybernetics 24 (1994) 656–667.

[17] N. Mera, L. Elliott, D. Ingham, On the use of genetic algorithms for solving ill-posed problems, Inverse Problems in Engineering 11 (2003) 105–121.

[18] Y. Leung, Y. Gao, Z. B. Xu, Degree of population diversity - a perspective on premature convergence in genetic algorithms and its markov chain analysis, IEEE transactions on neural networks / a publication of the IEEE Neural Networks Council 8 (1997). 18255718.

[19] Z. Wang, A. Bovik, H. Sheikh, E. Simoncelli, Image quality assessment: from error visibility to structural similarity, Image Processing, IEEE Transactions on 13 (2004) 600 –612.

[20] R. F. Mudde, Bubbles in a fluidized bed: A fast X-ray scanner, AIChE Journal 57 (2011) 2684–2690.

[21] R. Wehrens, E. Pretsch, L. M. C. Buydens, The quality of optimisation by genetic algorithms, Analytica Chimica Acta 388 (1999) 265–271.

[22] E. Alba, M. Tomassini, Parallelism and evolutionary algorithms, Evolutionary Computation, IEEE Transactions on 6 (2002) 443–462.

4

A Hybrid Algorithm

This paper compares two techniques for reconstructing images from time-resolved X-ray tomography data: Simultaneous Algebraic Reconstruction Technique (SART) and Adaptive Genetic Algorithm (AGA). The advantages and disadvantages of both are discussed, and we combine them into a hybrid algorithm. The hybrid method uses results from AGA as the starting values for SART. We demonstrate that this leads to improved reconstruction results: less noise than SART and better reconstruction of shapes than AGA.

This chapter is based on the submitted paper: Xiaogang Yang, J. Ruud van Ommen, J. Schoormans and Robert F. Mudde. A hybrid tomographic reconstruction algorithm for a high speed X-ray tomography system, *Computer Physics Communication*.

4.1. Introduction

In many industrial applications particles and gases need to be brought into close contact. In the (bio-)chemical process industry this often concerns production of base materials in large quantities. Economic operation requires large scale equipment and continuous operation. One of the working horses in this industry is the so-called fluidized bed [1]: in essence a large cylindrical container filled with small particles (usually submillimeter in diameter). Gas is flowing through this container from bottom to top. An obvious advantage of working with granular material is the enormous surface area that granular material has: one cubic meter filled with 0.1 mm diameter particles has a total particle surface of 3.0×10^4 m^2, i.e. sufficient to cover 6 soccer fields. For catalytic reactions carried out in the container, this increases the efficiency of the process enormously.

For a certain window of gas flow rates, the drag force exerted on the particles by the gas flow will be able to balance gravity on the particles. This makes these particles 'float'. As a consequence the powder inside the container starts behaving like a quasi-fluid, hence its name fluidized bed. Fluidized beds are part of the family of multiphase flows in which two or more different gases/liquids/solids are present. A peculiar feature of fluidized beds is the formation of gas bubbles inside the powder. This is a consequence of a natural instability that develops inside the bed. These bubbles or voids are virtually free from particles. This makes them light, like air bubbles in water. Consequently, they will rise to the top of the bed. Their presence has advantages and disadvantages at the same time: they mix the particles, but at the same time lead to a decreased gas-particle contact. For proper operation of these fluidized beds a good description of the bubbles (their size and velocity distribution, spatial distribution, etc.) is of great importance and a lively area of research.

A particular problem in studying the behaviour of bubbles in a fluidized bed is the opacity of the system, denying the use of laser and camera based techniques. Alternatively, intrusive probes cause disturbances in the flow and bubble behaviour. Therefore, non-intrusive techniques based on electrical properties (Electrical Capacitance and Electrical Resistivity Tomography) have been developed [2, 3]. Although these are fast techniques, capable of generating 1000 tomograms per second or more, the resolution in the interior of the fluidized bed is problematic. Nuclear based measuring techniques via γ or X-rays, promise a better spatial resolution. However, they are generally speaking slow and it is difficult to reach 100 tomograms per second. In the last decade a few groups have developed fast X-ray tomographic scanners [4, 5]. The measurements make use of the attenuation of X-rays by the material in the fluidized bed: the particles absorb much more radiation than the gas phase. Consequently, if a bubble passes through the imaging plane, some of the detectors will see an increased radiation intensity, while others don't.

Image reconstruction using the Algebraic Reconstruction Technique (ART) has been developed in the last century for medical applications of X-ray tomography [6]. In these applications, the object to be imaged is radiated through from many angles

by rotating the source-detector pair around the object. This is a rather slow procedure that typically generates data for a few tomograms per second. This is clearly insufficient for studying flow phenomena. As a consequence of the required speed, only a limited amount of viewing angles are available in high speed X-ray tomography and the reconstruction problem is ill-posed. Consequently, the well know Linear Back Projection and Filtered Back Projection can not be applied as these will produce blurry images [7]. The Simultaneous Algebraic Reconstruction Technique (SART) [8] has been applied to overcome these problems. However, SART is rather sensitive to noise. The Genetic algorithm (GA) [9] is a promising method to solve the ill-posed inverse problems [10]. It is recently introduced for tomographic image reconstruction [11–16]. It is shown that GA can perform well in reconstructing images from ill-posed and noisy data. Simple GA faces a premature convergence in such ill-posed inverse problem, which can be prevented by an Adaptive Genetic Algorithm (AGA) [17]. We have compared both SART and AGA for high speed X-ray tomography [18]. Both approaches have their advantages and disadvantages. The combination of GA with other optimization algorithms has been proposed by e.g. [19–21].

In this paper, we present a hybrid algorithm for image reconstruction of the high speed X-ray tomography. We study the improvements of AGA compared with simple GA for tomographic reconstruction. The limitations of AGA are also discussed. We use the results of AGA as the initial guess for SART. The reconstruction accuracy is improved by this hybrid approach. We demonstrate the performance of SART, AGA, and the hybrid algorithm by using synthetic data. We also compare these methods with real measurement data. The advantage of the hybrid algorithm is discussed.

4.2. Methods

Both SART and AGA have advantages and disadvantages. We use the synthetic data to mimic a case with rather small phantoms and a case with small distance between the phantoms. The reconstruction results of SART and AGA are shown in Fig. 4.1. Because AGA produces varied results for different runs of the same input, we use the average from 10 runs for each case of AGA. For the reconstruction results of SART, we find that small phantoms blur. There are a lot of grey areas outside the phantoms, with pixel values close to those of the reconstructed phantoms. We cannot determine whether these grey areas are objects or noise without prior knowledge. When two phantoms have a small distance, we find that the boundary of the two phantoms cannot be easily distinguished. For the reconstruction results of AGA, all the small phantoms are reconstructed. The boundary between the two phantoms is clearer. However, the shape of the phantoms are coarse, with wrong pixel values appearing at irregular positions inside and around the phantoms. This makes identification of the phantom shape difficult.

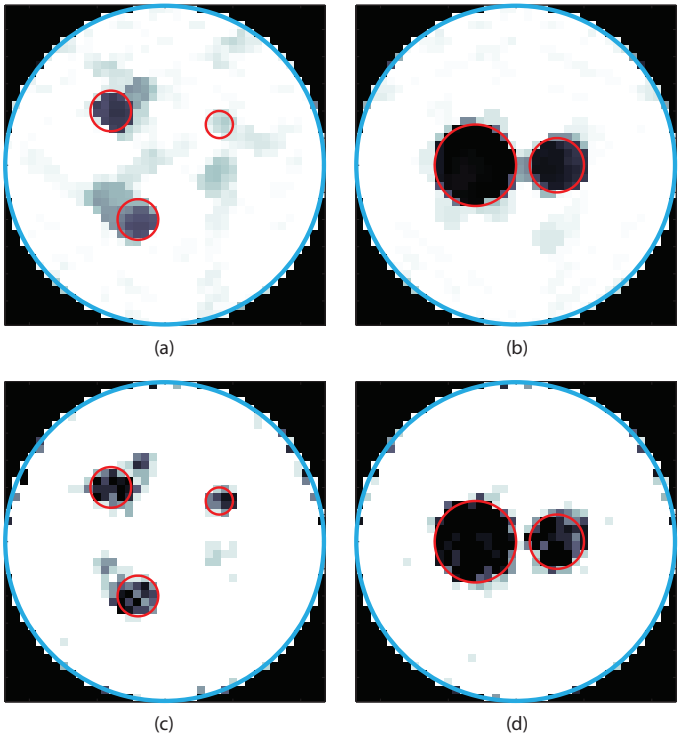

Figure 4.1: Comparison between SART and AGA. (a) and (b) are reconstructed by SART. (c) and (d) are reconstructed by AGA. (a) and (c) are the case for small phantoms. (b) and (d) are the case for small distance between phantoms. The results of AGA are the average from 10 runs for the same inputs, thus the grey-scale images is obtained from the average of 10 binary images.

We evaluate the variance of the pixel value during a AGA reconstruction to determine the reason for the coarseness. For a Binomial variable X, the variance $\tilde{Var}$ of the pixel value is:

$$\tilde{Var}(X) = N_{ind}\tilde{A}_i(1 - \tilde{A}_i) \tag{4.1}$$

where N_{ind} is the number of the individuals (600 for this article); i is the generation number; $\tilde{A}_i$ is defined as:

$$\tilde{A_n} = \frac{1}{N_{ind}} \sum_{j=1}^{N_{ind}} Chrom_{i,j} \tag{4.2}$$

where j is the individual number; $Chrom$ is the pixel values of each chromosome.

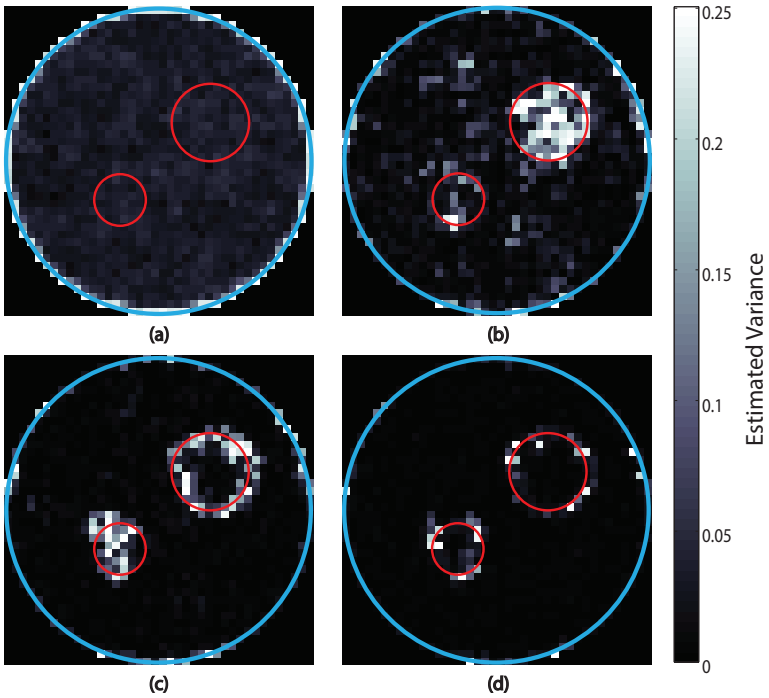

Figure 4.2: Estimated variance of every pixel during a regular AGA reconstruction. The red circle indicates the true shape and position of the phantoms. The blue circle is the wall of the fluidized bed. (a) The first generation; (b) After 50 generations; (c) After 100 generations; (d) After 150 generations.

A higher value of the estimated variance means that the pixel values of the individuals are more spread out around the average of the population. If a pixel has a higher estimated variance, it means it has higher probability to change during the iteration of AGA. At generation 1 (Fig. 4.2 (a)), the variance is smaller than 0.1 and roughly homogeneous, for the bulk of the image. This variance comes from the initial random chromosomes where the AGA reconstruction started with. For the subsequent generations (Fig. 4.2 (b) & (c)), black regions appear where the variance is very low. These low-variance regions signify that the majority of the population shares the value for these pixels, which can be either 0 or 1. For generation 150 (Fig. 4.2 (d)), there is low variance in the bulk phase of the reconstruction, and inside the phantoms. Only the boundary areas of the phantoms and some spots near the wall of the fluidized bed have a high-variance. This means the searching pixel space focuses on a few pixels around the boundary of the phantoms. In principle, AGA is a global optimization algorithm that considers all the pixel values at the same time. However, the searching space is possibly trapped in a few pixels when most of the pixels are close to their true value. This makes that the reconstructed shapes deviate from the original phantom shape.

The reproducibility for AGA is a problem when the number of pixel is big (bigger

than 40×40 pixels for our current setup) or the phantom number is too high (more than 3 phantoms) [18]. We tested the same case with exactly the same phantoms for 100 runs of AGA. The 100 different results are averaged to give the final reconstruction; see Fig. 4.3 (a). Although, most of the reconstructed phantoms match their true shape and position, there are still noisy pixels or phantoms produced from a few of the results. We use the SSIM value (Structural Similarity) [22] to estimate the similarity between the reconstructed images and the input image. It is a criterion, which combines luminance comparison, contrast comparison and structure comparison, to estimate the similarity of two images. The fiducial value is 1: images are more similar, if their SSIM is closer to 1. The histogram of the SSIM values for all 100 runs is plotted as Fig. 4.3 (b). We found that about 25% of the results are perfectly reconstructed. There are reconstruction errors for the rest of the results. These errors are randomly produced, which we cannot quantitatively predict for the cases without prior knowledge. Averaging the results from different runs has been proved as a reasonable way to partly solve this problem [18].

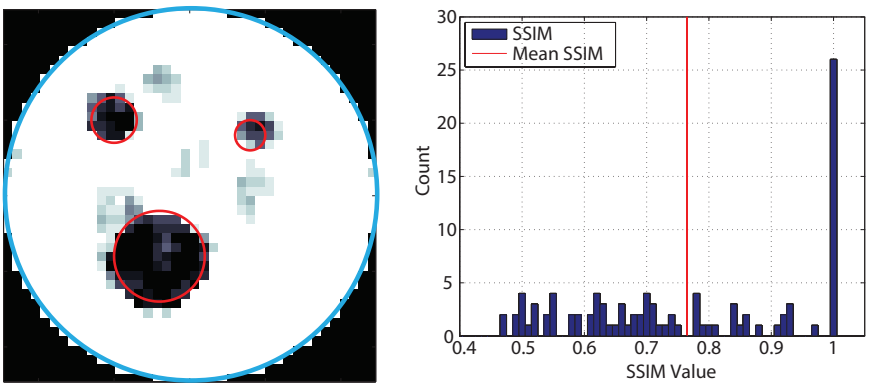

Figure 4.3: The reproducibility of AGA. (a) Averaged results for the same input from 10 different runs; (a) Histogram of SSIM value for the same case from 100 runs.

AGA distributes pixel values by considering all the pixels at the same time, but is not accurate at the level of a single pixel. SART accurately updates each pixel value, but it has high possibility to be trapped in a local minimum. Once in a local minimum, SART tries to group the pixels. AGA does not get easily trapped in a local minimum, but cannot converge to smooth shapes. They have complementary characteristic. Therefore, we developed a hybrid algorithm to combine their advantages:

- Reconstruct multiple images with AGA. We first use AGA to run the reconstruction for 10 times. The number of individuals is 600. We choose the best result from each run, thus 10 reconstructed images are obtained with the same input. We have tested different meshes with different cases. A maximum mesh for which AGA is capable to give a reasonable result is about

50×50 for our current setup [18];

- Average the results from AGA. The reproducibility problems can be partly solved by averaging the results from different runs of AGA. We have studied this earlier [18]. The averaging of 10 results from AGA is a compromise between accuracy and efficiency;
- Threshold the averaged image. We threshold all pixels with a threshold of 0.65. If a pixel value is larger than 0.65, it is set to 1, otherwise to 0. This procedure makes the result binary again and it removes part of the noise;
- Refine the image with SART. We use the thresholded result from the above step as an initial input for SART. We run SART only for 100 iterations. We have tested different cases for different number of iterations. Once we use the result from AGA as the initial input for SART, SART quickly converges in less than 100 iteration.

4.3. Results & Discussions

We use synthetic data to estimate the performance of the different algorithms. We simulate the X-ray signal of circular phantoms in a circular cross section (diameter 24 cm), which mimics the flow of bubbles through a cross section in our real system. Bubbles in a fluidized bed have the shape of a spherical cap, i.e. the look like an open umbrella, but instead of having a flat base, they have a curved inwards base as a consequence of a low pressure zone in their wake. When cutting horizontally through these bubbles, the top part is seen as a sphere, while their bottom part shows up as a ring. By using synthetic data, the reconstruction results can be easily compared with inputs. The results of the different approaches can be found in Fig. 4.4. The hybrid approach produces less noisy pixels outside the object phantoms than SART. The small hole in the big phantom can be clearly determined by reconstruction. The hybrid approach also reconstructs the phantom shape more accurate than AGA. The advantages of SART and AGA are efficiently combined. We estimated the SSIM [22] values of the 3 approaches with the input image. The reconstruction result of the hybrid algorithm has a higher value (0.836) than SART (0.796) and AGA (0.734).

To quantitatively compare the reconstruction accuracy of the 3 different algorithms, we evaluated the average pixel value around the calculated centroids of the reconstructed phantoms (see Fig. 4.5). This is an average from 1 to 360 degree around the calculated centroids and is plotted for the radius to the centroids. For both reconstructed phantoms, the hybrid algorithm reconstructs sharper boundary, illustrated by a change from one to zero over a shorter distance. Furthermore, the hybrid reconstruction is closer to the perfect values of one inside the phantom and zero outside the phantom. The hybrid algorithm shows its advances from both the visually and quantitatively point of view.

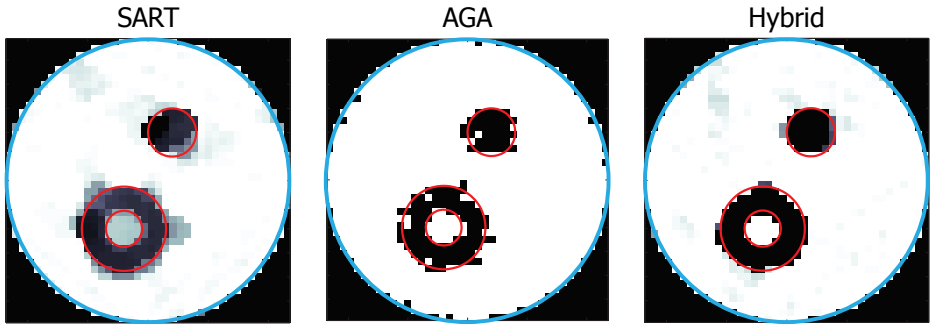

Figure 4.4: Comparison of the hybrid algorithm with SART and AGA. The results are computed from a synthetic data. The red circles indicates the true shape and position of the phantoms. The blue circle is the simulated cross section of the fluidized bed.

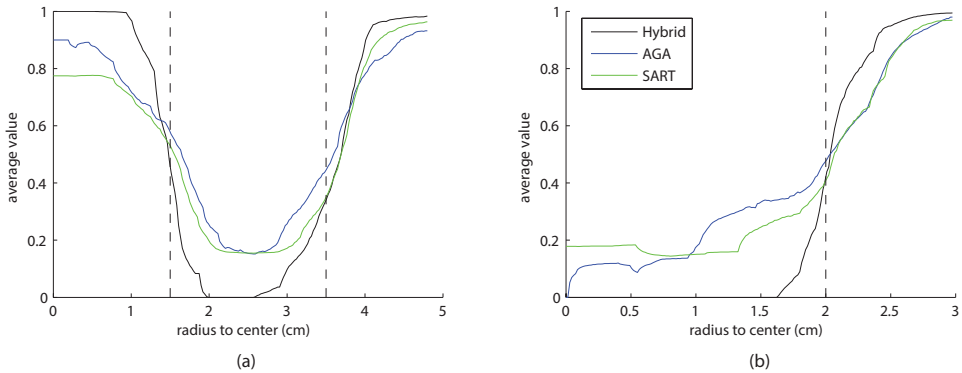

Figure 4.5: Average pixel value around the calculated centroids of the reconstruction phantoms. (a) The phantom at bottom left; (b) The phantom at top right. The dotted lines indicate the radius of the phantoms used for input.

Table 4.1: Diameter (mm) of the phantoms for each case.

Case	Phantom 1	Phantom 2	Phantom 3
1	36	17	None
2	36	58	None
3	9	36	58

A further assessment of the hybrid approach is carried out with reconstructions of real measurements. We place empty cylinders in a packed bed. The column containing the packed bed is a 24 cm inner-diameter Perspex tube. The particles are 0.56 mm sized polystyrene (standard deviation of particle size distribution is 0.16 mm). We use the round cross sectional voids of these cylinders to mimic the gas voids of bubbles in the cross section. The diameter of the phantoms is given in

Table 4.1. The location of the phantoms is shown as the red circle in Fig. 4.6.

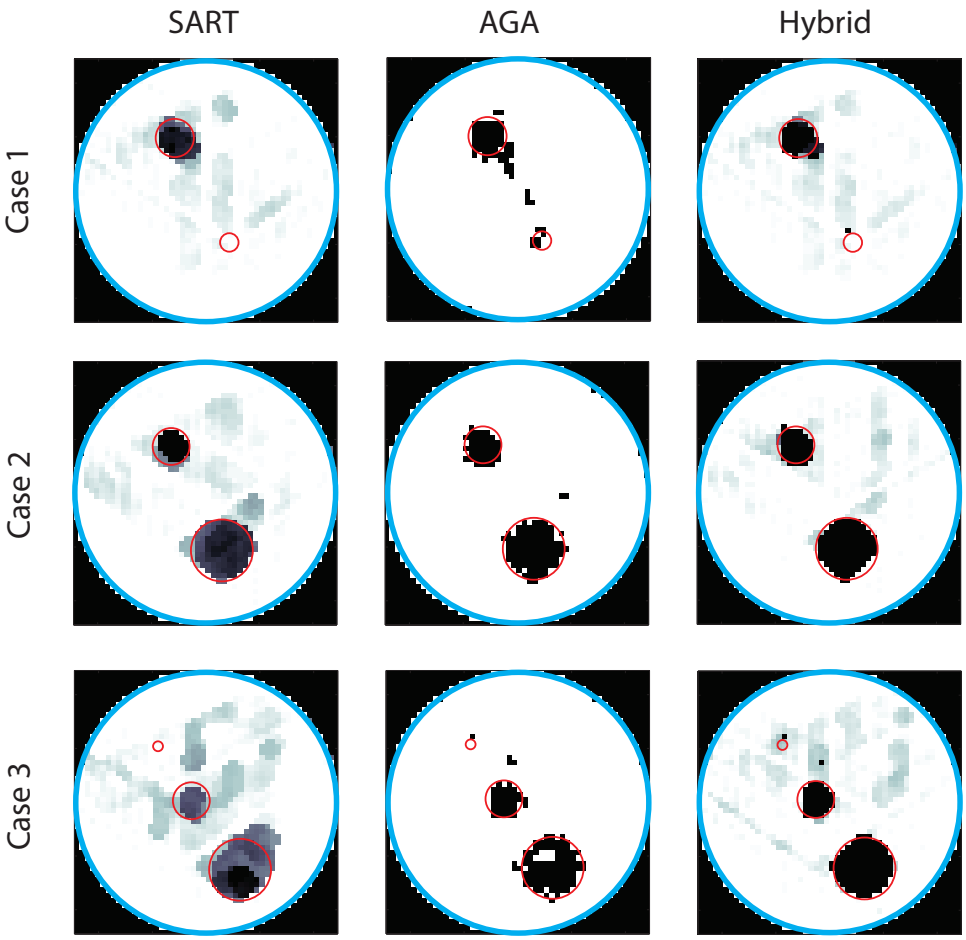

Figure 4.6: The reconstructions from the measurement data. The mesh is 50×50 pixels. The blue circle is the wall of the fluidized bed. The red circle is the true location of the phantoms.

We reconstruct images for each case with SART, AGA, and the Hybrid approach respectively (see Fig. 4.6). The average cross-sections of the reconstructed phantoms are shown in Fig. 4.7. For case 1, SART only reconstructed the larger phantom. AGA reconstructed multiple phantoms: we cannot distinguish these noise-phantoms and the true phantom. The hybrid algorithm reconstructed the big phantom and a single pixel for the small phantom: it is also unknown whether it is just noise or a true phantom. However, the noise-phantoms between the big phantom and small phantom disappear. For case 2, the hybrid and AGA reconstructions are of similar quality, both with a sharp boundary, and values of zero near the center, and values of one outside the phantoms, indicating well-defined phantoms. The-

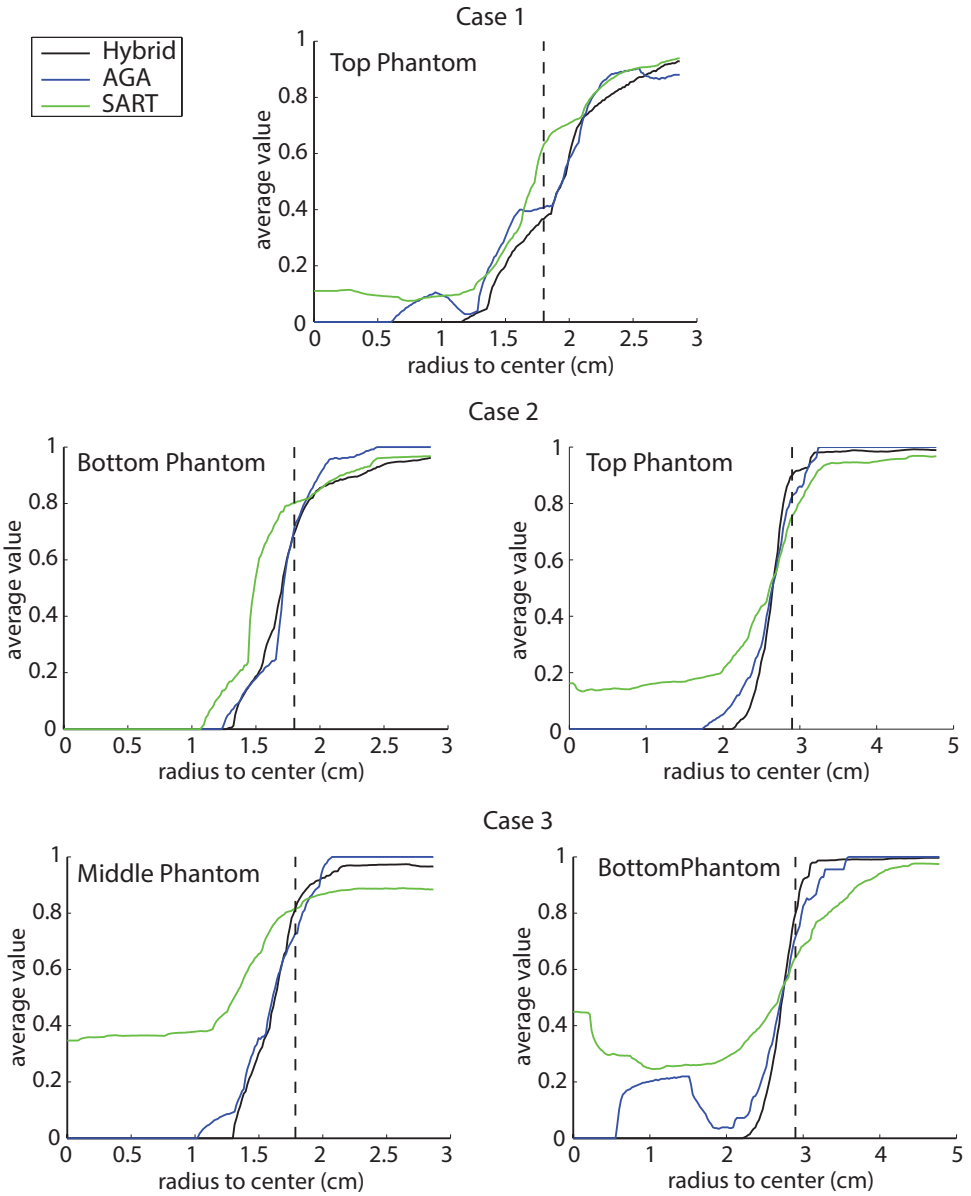

Figure 4.7: Average of cross-sections through the center of the reconstructed phantoms for the reconstructions based on measurement data.

SART reconstructions are a little worse: a less well-defined boundary indicated by a less steep rise in value, and the larger phantom is not completely zero inside the phantom. For case 3, the reconstruction of the smallest phantoms is unclear at best for all reconstructions. Given the area for the smallest phantom is less than

the area of 3 pixels in the current resolution, it is hardly to be recognized as phantoms by our reconstruction algorithms. AGA and the hybrid algorithm have a similar reconstruction quality for the smaller phantom shown here, better than SART. For the largest phantom, hybrid is better than both others. With respects to all these cases, the hybrid algorithm improves the reconstruction accuracy. The advantages of SART and AGA are efficiently combined.

The hybrid algorithm reconstructs more accurate results than SART or AGA. However, it is very time-consuming. The computing time for the hybrid algorithm is $(10 \times AGA + 0.2 \times SART)$. AGA consumes much more time than SART [18]. We use Matlab to test the algorithms. The hybrid algorithm consumes several hours for 1 image, which also depends on the number of phantoms in the fluidized bed. This algorithm is only used for accurately checking the results. The optimization of the coding and the parallel computing is recommended for its further application.

4.4. Conclusion

The image reconstruction for the high speed X-ray tomography is an ill-posed inverse problem. SART and AGA have been used for it. SART has the advantage to reconstruct an accurate shape of the phantoms, but produces too much noisy pixels outside the true objects. It also smears the small objects. AGA is improved compared with simple GA for convergence. However, the reconstructed shape of AGA is not accurate, because of its global estimation of such a system with so many variables. Also, genetic algorithms are confronted with the problem of reproducibility. A combination of AGA and SART is favorable to minimize their disadvantages while combining their advantages. The hybrid algorithm shows good potential of reconstructing images from very limited data.

References

[1] D. Geldart, Gas Fluidization Technology, A Wiley-Interscience publication, pp. 4–6.

[2] T. Dyakowski, R. B. Edwards, C. G. Xie, R. A. Williams, Application of capacitance tomography to gas-solid flows, Chemical Engineering Science 52 (1997) 2099–2110.

[3] W. Warsito, L. S. Fan, Ect imaging of three-phase fluidized bed based on three-phase capacitance model, Chemical Engineering Science 58 (2003) 823–832.

[4] R. F. Mudde, Time-resolved X-ray tomography of a fluidized bed, Powder Technology 199 (2010) 55–59.

[5] M. Bieberle, F. Fischer, E. Schleicher, D. Koch, H. J. Menz, H. G. Mayer, U. Hampel, Experimental two-phase flow measurement using ultra fast

limited-angle-type electron beam x-ray computed tomography, Experiments in Fluids 47 (2009) 369–378.

[6] A. C. Kak, M. Slaney, Principles of Computerized Tomographic Imaging, 1988.

[7] F. Natterer, The Mathematics of Computerized Tomography, John Wiley & Sons, pp. 85–118.

[8] A. Andersen, A. Kak, Simultaneous Algebraic Reconstruction Technique (SART): A superior implementation of the ART algorithm, Ultrasonic Imaging 6 (1984) 81 – 94.

[9] J. H. Holland, Genetic algorithms, Scientific American 267 (1992) 66–72.

[10] N. Mera, L. Elliott, D. Ingham, On the use of genetic algorithms for solving ill-posed problems, Inverse Problems in Engineering 11 (2003) 105–121.

[11] K. D. Kihm, K. Okamoto, D. Tsuru, H. S. Ko, Adoption of a genetic algorithm (GA) for tomographic reconstruction of line-of-sight optical images, Experiments in Fluids 22 (1996) 137–143.

[12] M. Venere, H. Liao, A. Clausse, A genetic algorithm for adaptive tomography of elliptical objects, Signal Processing Letters, IEEE 7 (2000) 176–178.

[13] C. Wu, Y. Cheng, Y. Ding, F. Wei, Y. Jin, A novel x-ray computed tomography method for fast measurement of multiphase flow, Chemical Engineering Science 62 (2007) 4325 – 4335.

[14] C. Valenti, A genetic algorithm for discrete tomography reconstruction, Genetic Programming and Evolvable Machines 9 (2008) 85–96.

[15] M. Abdoli, M. R. Ay, A. Ahmadian, R. Dierckx, H. Zaidi, Reduction of Dental Filling Metallic Artifacts in CT-based Attenuation Correction of PET Sata Using Weighted Virtual Sinograms Optimized by a Genetic Algorithm, Medical Physics 37 (2010) 6166–6177.

[16] V. Di Gesu, G. Lo Bosco, F. Millonzi, C. Valenti, A memetic approach to discrete tomography from noisy projections, Pattern Recognition 43 (2010) 3073–3082.

[17] M. Srinivas, L. M. Patnaik, Adaptive probabilities of crossover and mutation in genetic algorithms, IEEE Transactions on Systems Man and Cybernetics 24 (1994) 656–667.

[18] X. Yang, J. R. van Ommen, R. F. Mudde, Comparison of genetic algorithm and algebraic reconstruction for x-ray tomography in bubbling fluidized beds, Powder Technology 253 (2014) 626–637.

[19] T. M. Gwizdałła, The hybrid algorithm for the study of geometric configurations of 2d clusters of uniformly charged classical particles, Computer Physics Communications 183 (2012) 1899–1903.

[20] I. G. Tsoulos, I. E. Lagaris, Genmin: An enhanced genetic algorithm for global optimization, Computer Physics Communications 178 (2008) 843–851.

[21] J. L. Klepeis, M. J. Pieja, C. A. Floudas, A new class of hybrid global optimization algorithms for peptide structure prediction: integrated hybrids, Computer Physics Communications 151 (2003) 121–140.

[22] Z. Wang, A. Bovik, H. Sheikh, E. Simoncelli, Image quality assessment: from error visibility to structural similarity, Image Processing, IEEE Transactions on 13 (2004) 600 –612.

5

The Dynamics of a Spouted Bed

Time-resolved measurements are carried out for determining the spout shape and position in several cross sections of a flat-base spouted bed filled with 2 mm polystyrene particles. A high speed X-ray image system, consisting of 3 X-ray sources and 2 layers of 32 detectors for each source, is employed to measure the spout shape with a temporal resolution of 2500 fps. The X-ray attenuation data are analyzed by both tomographic reconstruction and raw data analysis. The averaged spout diameters show good agreement with literature. A particle circulation model is made for validating the measured data. The fluctuations of the spout diameter are analyzed from the computed power spectral density. It is shown that the spout is most stable for $U/U_{ms} = 1.20 - 1.37$*. From measuring the center movement of the spout, we found an oscillation of the spout position. Its intensity is related to the bed height and gas flow rate.*

This chapter is based on the paper: Xiaogang Yang, J. Ruud van Ommen, E. Wagner, and Robert F. Mudde., Time-resolved Characterization of a Flat-Base Spouted Bed with a High Speed X-ray System, *Chemical Engineering Journal* 2014, 254, 143-152.

5.1. Introduction

A spouted bed is a system for contacting coarse granular solids (larger than $500\mu m$ in diameter) and fluids. It is widely used in gas-solid processes such as drying, coating and granulation. The study of spouted beds started early by Mathur and Gishler [1]. Several systematic studies have been carried out for it. However, there are divergent predictions and measurements for the size of the spout region. Moreover, direct observations of the stability of the spout are limited. The stability of the spout is important for industrial application, in which it is crucial to keep the gas-solids contacting constant.

A horizontal cross-section of a spout is typically considered to be of circular shape. Spout diameters were measured directly in half-cylindrical beds by Malek et al. [2] and McNab [3]. Later, a fiber optic probe was used to measure spout diameters by He et al. [4, 5] in both half and full column beds. Time-averaged spout diameters were measured by Wu et al. [6] with an X-ray CT scanner in a full column. Theoretical predictions were also made [2, 3, 7]. There are deviations for the predicted values between the half-column models and full-column models [5, 8]. The principles to distinguish the boundary of the spouts also differ from model to model.

In the early studies, three flow regimes of spouted beds were distinguished: packed, stable spouting, and unstable spouting. However, limited attention has been given to the dynamics of spouted beds. Malek et al. [2] mentioned that sometimes the spout oscillates around the axis of the column. The design factors to maintain the spouted bed in the stable mode were discussed by Olazar et al. [9, 10]. Fluctuations of the pressure drop in spouted beds were measured by Xu et al. [11], Lopes et al. [12], Wu et al. [6] and Mollick and Sathiyamoorthy [13]. The standard deviation and PSD (Power Spectrum Density) are used for further analysis of these measurements. They found that the fluctuations of the pressure drop in different flow regimes are different.

X-ray tomography is an attractive tool for spout region measurements, since it can measure the interior of a non-transparent medium in a non-invasive way. It has been applied to the measurements of the fluidized beds [14–18] to find the time averaged solid concentration or gas hold-up. It has also been used for measuring the time-averaged spout diameter by Wu et al. [6]. For dynamic measurements, a high temporal resolution is required. The high speed X-ray tomography approaches developed by Mudde et al. [19] and Bieberle et al. [20] can provide a temporal resolution as high as 2500 - 7000 fps. These approaches are applied in time-resolved measurements of fluidized beds [21–24] with good potential of exploring the dynamics of those systems. This also suggests a good capability for time-resolved measurements of a spouted bed.

In the present paper, a novel approach is proposed to study the dynamics of spouted beds. We developed a raw data process, which provides much higher precision than the typical tomographic reconstruction, to obtain the spout diameter and position

from the measurement of the high speed X-ray tomography system. A case study for a flat-base spouted bed is presented. The time-averaged spout diameter ($\overline{D_s}$) is compared with the prediction of McNab [3]. A particle circulation model is built based on $\overline{D_s}$. The time-resolved spout diameters (D_s) are analyzed with spectral methods. The motion of the spout center of gravity will be presented. The fluctuations of the spout size and the oscillation of the spout position will be discussed based on these observations.

5.2. Experimental Setup

The experimental setup is composed of a flat-base spouted bed and a high speed X-ray tomography system, which is as shown in Fig. 5.1 (a). A digital mass flow controller (Bronkhorst E-7100-AAA) provides the inlet gas flow rate with specific flow rates, with a maximum error of 2%.

5.2.1. The spouted bed

The flat-base spouted bed is a 0.24 m inner diameter perspex tube (wall thickness 5 mm). The gas inlet is a round hole with a diameter of 0.02 m in the center of the column's bottom plate. The bed is filled with 2 mm sized polystyrene particles (solids density $1.05\times10^3 kg/m^2$), which is a Geldart group D particle. The static bed height H is 0.40 m. The superficial velocity at minimum spouting U_{ms} is $0.54 m/s$. It is calculated with Olazar et al. [25]'s correction of Mathur's method [26] for a nearly flat-base bed:

$$U_{ms} = \left(\frac{d_p}{D}\right)\left(\frac{D_i}{D}\right)^{0.1}\sqrt{\frac{2gH(\rho_p-\rho)}{\rho}} \tag{5.1}$$

The gas flow rate (Q) is 1400 to 2100 L/min. The ratio between superficial gas velocity and minimum spout velocity (U/U_{ms}) is 0.96 to 1.44.

Table 5.1: The gas flow condition

Q (L/min)	1400	1450	1500	1550	1600	1750	2000	2100
U/U_{ms}	0.96	0.99	1.03	1.06	1.10	1.20	1.37	1.44

For each flow condition, we do measurements at 7 vertical positions from 0.05 to 0.35 m above the bottom plate, with steps of 0.05 m. The vertical position here is the middle of the upper and lower detector layer (see Fig. 5.1 (b)). The distance between two detector arrays is 0.02 m. Thus, we collect X-ray data of two cross sections from two detector layers for each measurement. For instance, the measurement heights (H_m) are 0.04 and 0.06 m at vertical position 0.05 m. In the time-averaged analysis, we use the data points from each detector layer. In the time-resolved analysis, the mean values from two detector arrays are used, in

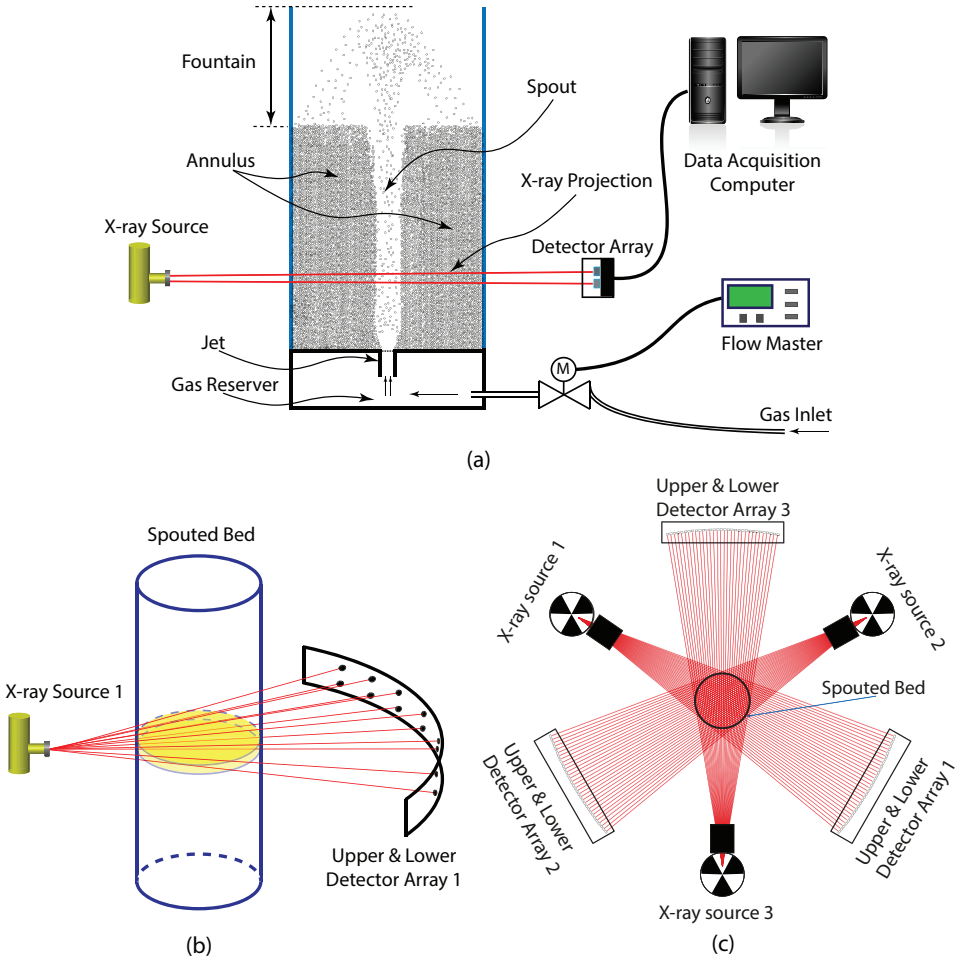

Figure 5.1: Schematic diagram of experimental setup. (a) Overall; (b) 3 - D view of X-ray source 1 and detector array 1 with double layers; (c) Top view of measurement system with spouted bed placed in the center.

order to reduce the system noise from the detectors.

5.2.2. The measurement device

The high speed X-ray tomography system developed by Mudde et al. [19] has been applied earlier for bubbling fluidized bed measurements [22, 23, 27]. It has been shown that this system is able to measure individual bubbles with an equivalent diameter larger than 0.02 m in a fluidized bed of 0.24 m diameter. We use this hardware for data acquisition, but developed a dedicated data processing procedure for the spouted bed.

Different from the traditional X-ray CT in medical use, the high speed X-ray tomography system in this paper is composed of 3 X-ray tubes and 3 detector arrays. The X-ray sources are placed at 120° around the fluidized bed. The detector arrays are placed opposite the X-ray sources. There are 2 parallel layers of 32 detectors placed as arches in each detector array. Fig. 5.1 (b) shows the structure of one X-ray source and detector array. As is illustrated in Fig. 5.1 (c), this design makes it possible to simultaneously obtain the X-ray attenuation data from different directions, enabling reconstruction of the image of the object's cross section.

The X-ray sources are X-ray tubes manufactured by Yxlon International GmbH, with a maximum energy of 150 KeV. The tubes currents are set at 2 mA in these measurements. The detectors are $CdWO_4$ scintilation detectors which are manufactured by Hamamatsu (type: S 1337 - 1010BR). The crystal size of the detector is 10 mm $\times$ 10 mm $\times$ 10 mm. The detectors are connected to a micro-computer to synchronize the data from all the detector arrays simultaneously, with a sampling frequency of 2500 Hz. After each measurement, the data is transferred to the data acquisition workstation.

5.3. Tomographic Reconstruction

Image reconstruction is the most typical way to obtain the phase distribution from the X-ray CT measurement. It has been applied in our high speed X-ray tomographic system for the bubbly flow of the fluidized beds [21, 23, 27]. It is an inverse procedure for computing the solids fraction from the measured X-ray intensity in a discrete domain. The image reconstruction for the high speed X-ray tomography system is a serious ill-posed inverse problem. We recently have compared two reconstruction techniques: a Simultaneous Algebraic Reconstruction Technique (SART), and a Genetic Algorithm (GA). We proposed a hybrid approach combining the two methods for improved reconstruction [28].

In the current paper, we also use the hybrid approach of SART and GA to reconstruct the time-resolved data. The temporal resolution is 250 fps, by averaging every 10 measurements for each image. Because the first and the last detectors for each detector array are not inside the bed, only 3×30 efficient detectors are used for reconstruction. A better image quality is obtained than only using SART or GA. However, the spatial resolution is rather limited to determine the spout changes in a time series. Figure 5.2 shows the reconstruction results for one experiment at different moments. Since the effective spatial resolution is only about 10 mm, it is not possible to detect the shape changes smaller than this size. Figure 5.2 only demonstrates that the spout shape is approximately round for these experiments.

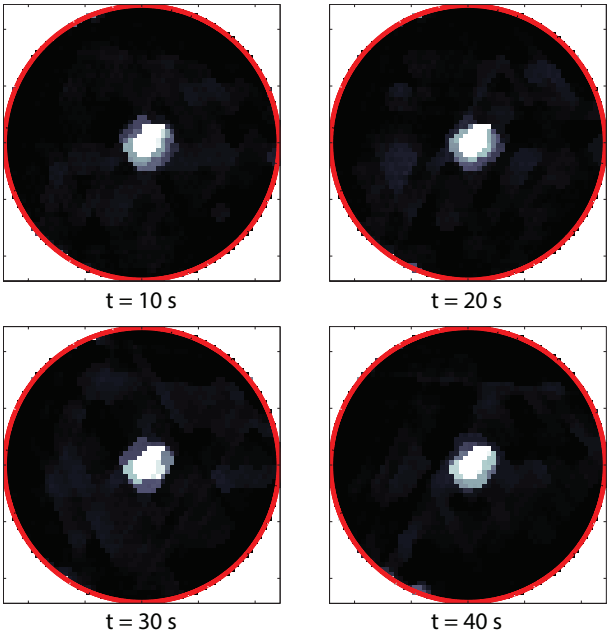

Figure 5.2: The reconstructed spout shape for different moments. Measurement condition: $H_m = 0.05m$, $Q = 2100L/min$

5.4. Raw Data Process

Direct analysis of the X-ray data is possible for a spouted bed, because of its simple shape in a cross section. We assume that:

- The spout shape stays round;
- The changes over time of the spout can be decomposed into two aspect: diameter expansion and shrinkage, and position oscillation.

The raw data process includes three main steps: (1) normalization; (2) fitting the curve and searching the spout; (3) measuring the spout from 3 detector arrays. The following description applies only for one measurement point in the time series. Step (1) and (2) are only for one detector array.

5.4.1. Normalize measured data

To correct the X-ray attenuation difference due to different detectors, the raw data I is normalized by the reference data I_{ref}.

$$y_{raw} = I/I_{ref} \tag{5.2}$$

y_{raw} is the normalized data for one of the three detector arrays. I is the measured data. I_{ref} is the reference data, which is measured when the bed is fully filled with

particles.

5.4.2. Curve fitting & Spout Searching

Fig. 5.3 shows the normalized data y_{raw} for one detector array. With the different value of y_{raw} for different detectors, we can roughly determine where the spout appears. The ratio of I and I_{ref} indicates the X-ray attenuation ratio of measurement and full bed. When the bed is full, the initial value should be 1. If there is a gas void in the path of the projection for one detector, the ratio should be higher than 1. However, in the real measurement, there are errors in these values, due to the measurement noise. Therefore, it is not possible to distinguish the spout position directly with y_{raw}. We carry out three steps for determining the boundary points of the spout among one detector array:

- Smooth the noise due to detector differences: the sensitivity of each detector is slightly different, which leads to noisy variation of y_{raw} among the different detectors. We treat the data from one detector array as a spatially distributed signal. A low pass filter is applied to reduce the noisy variation between neighbouring detectors. We obtain y_{smooth} from y_{raw}, given as the blue line and the cross in Fig. 5.3.
- Fit the data of the spout with a parabolic function: we search for the global peak in y_{smooth}. The curve around the peak is the spout region. Its shape is very close to the parabolic curve. We fit it with a parabolic function to obtain y_{fit} from y_{smooth}, given as the red line in Fig. 5.3.
- Determine the boundary position of the spout by solving the equation $y_{fit} = y_{mean}$. y_{mean} is the average value of all detectors (green line in Fig. 5.3). The intersection points of y_{fit} and y_{mean}, which are the two solutions of the above equation, are considered as the boundary of the spout over one detector array. The dashed lines (Fig. 5.3) shows the boundary line of the spout from one detector array.

We repeat the above steps for 3 X-ray sources. The interpolated locations (N_{s11}, N_{s12}, N_{s21}, N_{s22}, N_{s31}, and N_{s32}) for the spout boundary are obtained.

5.4.3. Defining the spout

The spout size and position are finally defined by combining the boundary lines from the three detector arrays at different angles. As shown in Fig. 5.4 (a), when we plot all the projections of the spout boundaries, a hexangular star is formed. The spout size and position is inside the constrains of the lines. We form a Cartesian coordinate system for defining the spout size and position (see Fig. 5.4 (b)). The origin is the geometrical center of the 3 X-ray sources. The angles (β_{s11}...β_{s32}) in the coordinate system for the boundary lines (L_{s11}...L_{s32}) can be calculated from N_{s11} ...N_{s32} and the angle ($\Delta\alpha$) between the projections for two neighboring detectors. The equations of the boundary lines (L_{s11}...L_{s32}) can be defined from the position

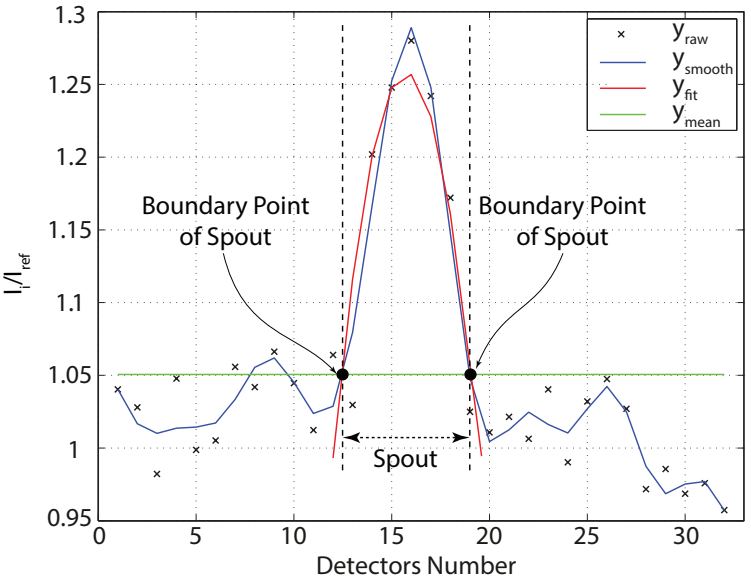

Figure 5.3: Procedure to define the boundary points of the spout from measured data and reference data. Plot of raw data, smoothed data and fitted data.

of X-ray sources ($S_1(x_{s1}, y_{s1})$, $S_2(x_{s2}, y_{s2})$, and $S_3(x_{s3}, y_{s3})$), and $\beta_{s11}...\beta_{s32}$.

The projections of the boundaries form $\triangle ABC$ and $\triangle A'B'C'$ (Fig. 5.4 (b)), where A, B, C, A', B', C' is calculated by finding the intersection points of $L_{s11}...L_{s32}$. The radius r_1 and r_2 and center (x_1, y_1) and (x_2, y_2) of two incircles can be determined. The averaged $r = (r_1+r_2)/2$ and $(x, y) = ((x_1, y_1)+(x_2, y_2))/2$ fit all the boundaries for three of the detector arrays. We consider the circle $(radius = r, center = (x, y))$ as the spout we measured in the cross section.

With repeating the process of sections 5.4.1, 5.4.2 and 5.4.3 for all the measurement points in a $40s$ time series, the spout diameter D_{sH} and center (X, Y) are obtained as a function of time.

The spout diameter as calculated in the current paper is expected to be a little underestimated (5 to 10 %), because we use the average value of the whole cross section as the threshold. This value is around 1.05 to 1.10, which is a dynamic value. In principle, the threshold should be constant 1. However, the X-ray intensity and detectors sensitivity change from time to time during the measurement. If we use the constant threshold, this change generates a strong system noise, which can be reduced by using the dynamic threshold.

The raw data process improves the spatial resolution significantly. The efficient resolution is about 10 mm from the tomographic reconstruction. However, in the

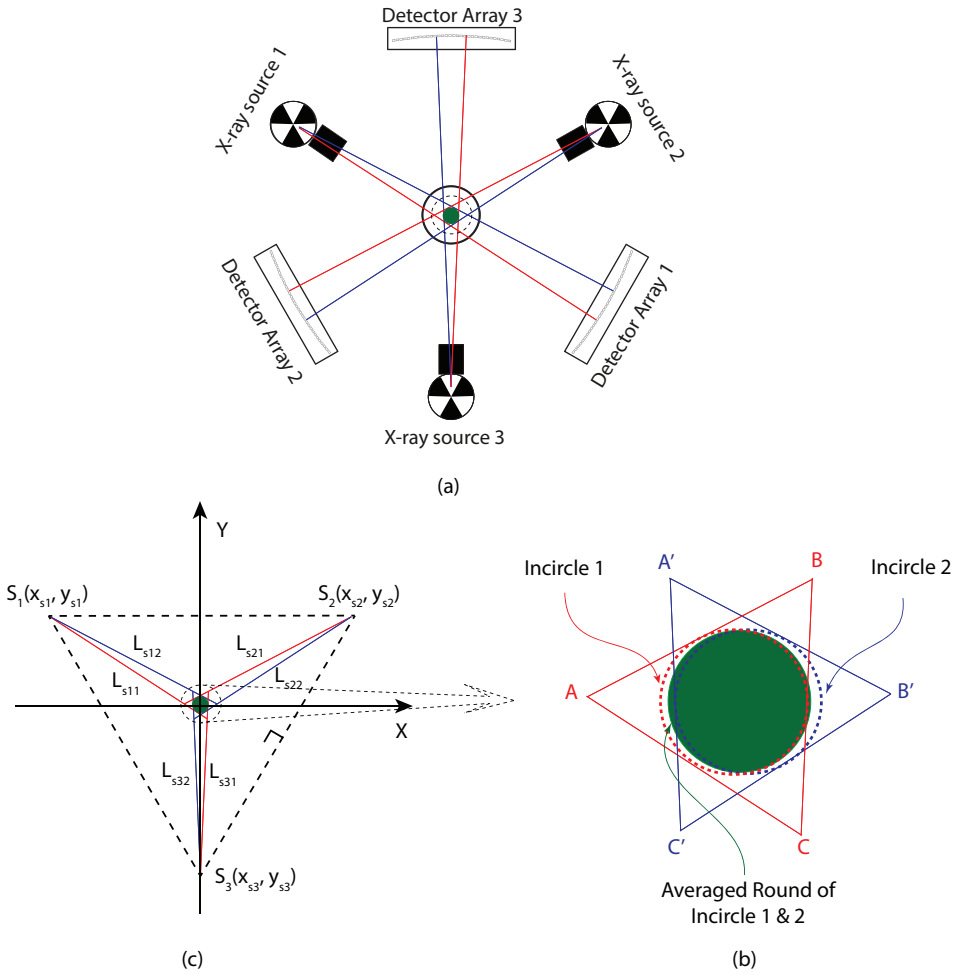

Figure 5.4: Top view of defining spout: (a) define spout from 3 direction with 3 X-ray sources and detector arrays, the red lines and blue lines are the projections of the spout boundary; (b) the coordinate of the computing system; (c) zoom in of defining spout with the incircle of 2 triangles, $\triangle ABC$ and $\triangle A'B'C'$.

raw data process, we interpolate the value of the spout from the fitted curve of the spout region (see Fig. 5.3). The interpolation is estimated from more than 18 detectors (the detector inside the spout region) for 3 detector arrays. Because the assumption of the round shape of the spout, the resolution does not depend on the distance between neighboring detectors anymore. It depends on the sensitivity of the X-ray detector. The range of the X-ray intensity change for our X-ray detector is from 200 to 4000 counts, which indicates the thickness of the bulk phase from 240 to 100 mm for our measurements. The efficient resolution thus becomes sub-

millimeter.

5.5. Time-averaged Spout Size

To enable a comparison with previous experimental and theoretical findings, we first present the time-averaged results of the measurements.

5.5.1. The spout profiles in vertical direction

The spout profiles are sketched from the mean diameter of the spout for different measurement heights. The mean diameter of the spout is calculated from D_{sH} for each measurement. As is shown in Fig. 5.5 (a), the spout grows fast when it is close to the bottom, and keeps an almost cylindrical shape for a height above 0.04 m. When we zoom in the plot (Fig. 5.5 (b)), we find that the spout profiles are slightly different for different gas flow rates. For the cases $U/U_{ms} < 1$, the spout expands from bottom to the top in general, but the gradient is not a constant value. For the cases $U/U_{ms} = 1.03$ to 1.20, the spouts keeps expanding when the height increases. The relations between the diameter of the spout and the measurement height is almost linear, except when it is close to the bottom. For the cases $U/U_{ms} > 1.20$, the spout is fat in the middle. There is a neck when it is close to the surface, and then it expands with a larger gradient. Because there are flanges and bolts that attenuate the X-ray, no data is available from the bottom plate to H_m = 0.04 m.

We estimate the spatial uncertainty of our results by comparing them from different time length and average rate. For all the averaged spout diameters, we compute 8 groups of data and calculate the standard deviations between them. A maximum standard deviation of 0.25 mm is found. We also estimate the absolute error by computing the effects of the system noise for the measurement results. There is a high frequency (>1000 Hz) system noise from our X-ray system, the maximum noise intensity is about 1.2% of the measured X-ray intensity. A maximum error of $\pm$1.5 mm is expected.

The equation of the average spout diameter $\overline{D}$, based on a half-cylindrical bed, as given by McNab [3] is:

$$\overline{D}_s = 2.0G^{0.49}D^{0.68}/\rho_b^{0.41} \tag{5.3}$$

where G is the mass flux of gas (kg/m^2s); D is the diameter of the bed (m); ρ_b is the bulk density in the annulus (kg/m^3).

We listed $\overline{D_s}$ according to McNab, the measured average spout diameter $\overline{D}_{sExp}$ and average deviation Δ_{mean} in Table 5.2.

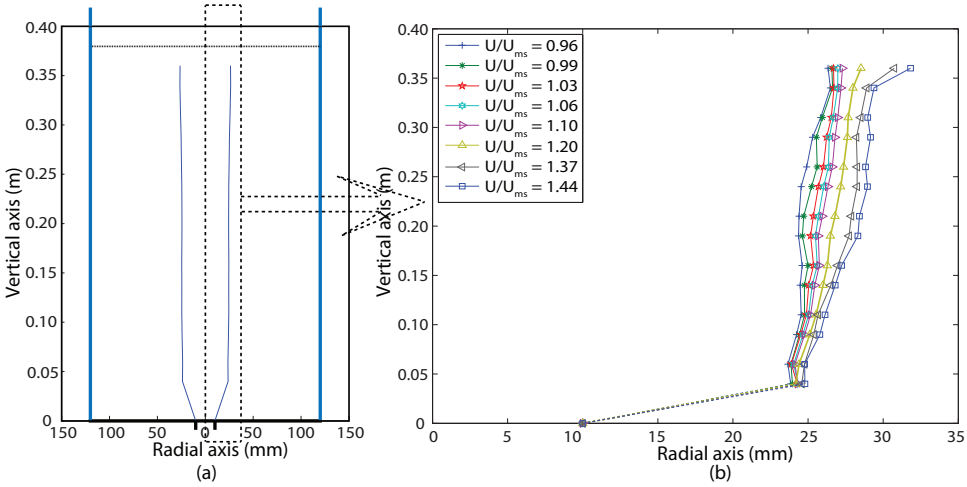

Figure 5.5: The spout profiles in vertical direction. The absolute error is ± 1.5 mm

Table 5.2: Comparison between experimental data and prediction by McNab's method for average spout diameter

U/U_{ms}	0.96	0.99	1.03	1.06	1.10	1.20	1.37	1.44
$\overline{D_s}(mm)$	43.0	43.7	44.5	45.2	45.9	48.0	51.2	52.4
$\overline{D}_{sExp}(mm)$	47.7	48.2	48.9	49.3	49.7	50.8	52.3	53.2
$\Delta_{mean}(\%)$	10.9	10.3	9.9	9.1	8.2	6.0	2.2	1.6

There is a 1.6 to 10.9% of deviation for $\overline{D}_{sExp}$ compared with $\overline{D_s}$ for different flow conditions. However, another measurement using fiber optic probe for a full-column bed was done by He et al. [5]. They found that McNab' s method underestimates the average spout diameter with an average deviation of 35.5%. Their measurements are for $U/U_{ms} = 1.1, 1.2, 1.3$. The McNab' s method is based on the half-column bed, so deviations compared with a fully cylindrical bed are possible. Our measurement results are smaller than those by He et al. [5], in which they define the sudden change of particles velocity as the spout boundary. We use the sudden change of particles concentration as the spout boundary. We also use a higher threshold which is leading to a slight underestimation of the spout diameter (see section 5.4.3).

5.5.2. A particle circulation model

To obtain better insight into the involved phenomena, we developed a simple flow model to describe the particle circulation inside the bed based on the average spout diameter. As in Fig. 5.6, the particles are injected from the bottom part of the annulus into the spout. They are blown upwards in the spout by the gas flow from the bottom jet. Above the bed they form a fountain. The gas flow is too small to

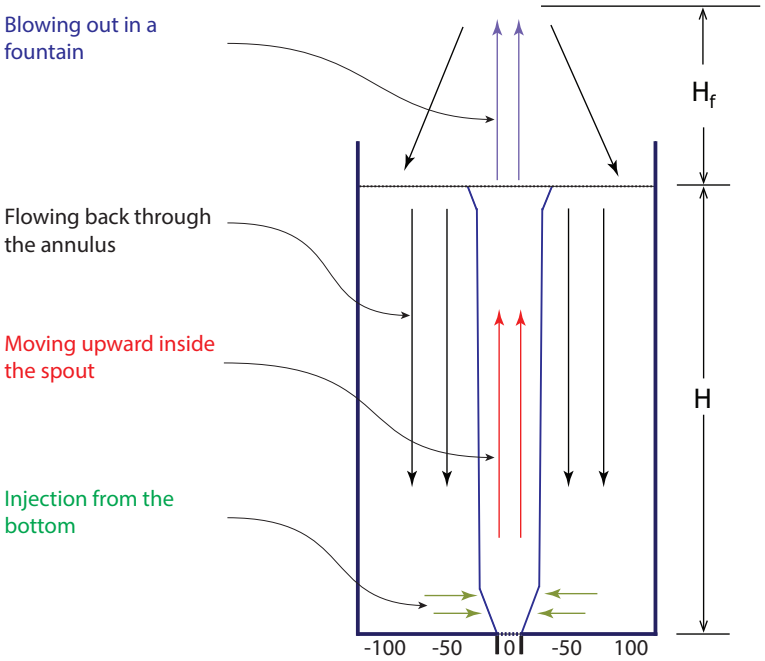

Figure 5.6: The model of particles circulation

carry the particles in this region. The particles fall down from the top of the fountain and move back to the bottom through the annulus. The particle trajectory in the bed is divided into four sections :

(1) Injection from the bottom of the spout:
We assume that the particles inside the spout are all fed from the bottom. As is shown in Fig. 5.5, the spout diameter increases when $H_m = 0 - 0.04$ m. When it is higher, it keeps a fairly constant diameter. So, we suppose that the particle transfer between the annulus and spout mainly happens in the conical surface of the spout in the bottom part ($H_m = 0 - 0.04$ m). The particle transfer can be written with mass conservation equation as:

$$v_r A_{in} \epsilon = n_{inj} V_p \tag{5.4}$$

where v_r is the radial velocity of the particles; A_{in} is the surface area for the particles injection; ϵ is the solid fraction at the surface; n_{inj} is the number of particles injection per unit time; V_p is the volume of a particle.

(2) Moving upward inside the spout:
We assume that the gas flow is mainly concentrated inside the spout. The

gas velocity in the inlet of the spout follows from the gas inflow rate:

$$(1-\alpha)A_o u_o = A_s u_s \tag{5.5}$$

where A_o is the cross section area in the spout inlet; u_o is the mean velocity of the gas in the spout inlet; A_s is the cross sectional area of the spout; u_s is the mean velocity of the gas inside the spout; α denotes the fraction of the gas leaking from the spout to the annulus. It is 0.23 in the present article, which we take from Takeuchi et al. [29] .

We ignore the frictional pressure drop and gravity on the gas inside the spout. The gas/particles flow follows momentum conservation. The incoming momentum of the gas is redistributed over the gas and the particles flowing in the spout:

$$A_o \rho_g u_o u_o = A_s \rho_g u_s u_s + n_{inj} m_p v_s \tag{5.6}$$

where ρ_g is the gas density; m_p is the mass of a particle; v_s is the particle velocity in the spout.

A particle is accelerated by the gas flow inside the spout via the drag force and slowed down by gravity. At the end of the spout the particle kinetic energy follows from the work done by the drag force and gravity:

$$\frac{1}{2} m_p v^2 = \int_0^H (F_D - m_p g) dh \tag{5.7}$$

where v is the velocity of the particle at the end of the spout; H is the bed height; F_D is the particle's drag force generated by the gas flow, which is as follow:

$$F_D = \frac{1}{2} C_D \rho_g A (u_s - v_s)^2 \tag{5.8}$$

where C_D is the drag coefficient; A is the cross sectional area of the particle.

(3) Blowing out in a fountain:
The particle in the fountain mainly moves because of its inertia at the outlet of the spout. The velocity of gas flow drops suddenly from the spout to the fountain. The acceleration by the gas flow becomes very small. The particle flow in the fountain can be written from energy conservation as below:

$$m_p g H_f = \frac{1}{2} m_p v^2 + \int_0^{H_f} F_{Df} dh \tag{5.9}$$

where H_f is the fountain height; F_{Df} is the particle's drag force in the fountain, which is as follow:

$$F_{Df} = \frac{1}{2} C_D \rho_g A (u_f - v_f)^2 \tag{5.10}$$

where u_f is the gas velocity in the fountain. It is calculated from a free jet theory [30]; v_f is the particle velocity in the fountain.

(4) Flowing back through the annulus:
The particle flow rate in the annulus is:

$$v_a A_a \epsilon = n_{inj} V_p \tag{5.11}$$

where v_a is the average velocity of the particles in the annulus; A_a is the average cross area of the annulus.

Thus, by solving Eq. 5.4 to 5.11, the fountain height H_f and particles velocity in the annulus can be calculated from the measured spout diameter. H_f can be measured via direct observation. The calculated H_f and measured value are compared in Fig. 5.7. Given the simplicity of the model, the agreement for $U/U_{ms} \geq 1.03$ is quite reasonable. There are big deviations for $U/U_{ms} < 1$, because our flow model is only valid in the case of stable particle circulation: a condition that is not satisfied at low gas velocities.

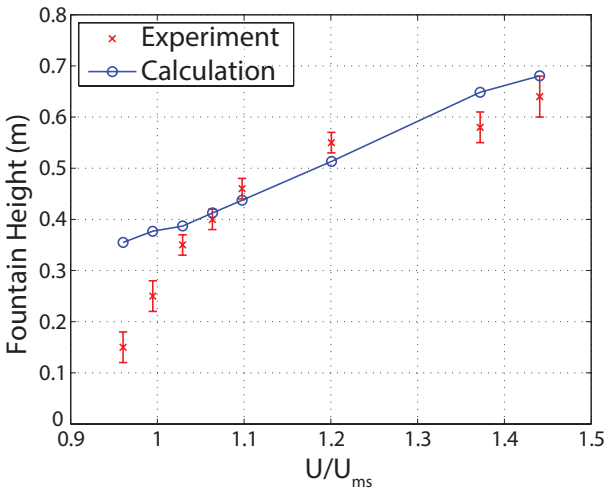

Figure 5.7: The fountain heights of the spouted bed from the prediction and direct measurement.

5.6. Spout stability

The time-resolved spout diameter and position is obtained from the raw data process, which provides high enough spatial resolution to distinguish the variations of in the scale of millimeter. In the evaluations of the stability for spout diameter, we only use the power spectral density (PSD) for low frequency range (0 to 50 Hz), which is far smaller than the frequency of the system noise. In the evaluation of the stability of the spout position, we reduced the sample frequency by averaging every 20 samples, reducing the sample frequency from 2500 Hz to 125 Hz. The system noise is reduced a lot by such method.

5.6.1. Stability of the spout diameter

We use the standard Welch's method [31] to estimate the PSD of the fluctuations of the spout diameter. Its basic principle is the discrete Fourier transform. In addition, the signal is divided into segments to increase the accuracy of the estimated PSD.

We use the PSD to determine the stability of the spout diameter as a function of the gas velocity and measurement position. The fluctuation of the spout diameter does not show a very regular pattern (see Fig. 5.8). Therefore, we do not evaluate the fluctuation energy at specific frequencies. We only compare the average power spectral density in the frequency range of 0 to 50 Hz, for the following reasons:

- The gas velocity in the bed is low, i.e. less than $1m/s$. The frequency of the fluctuation of spout diameter should not be very high.
- The sampling frequency is 2500 Hz. Thus, we can estimate the spectra up to a frequency of 1250 Hz. However, the total energy in the PSD for $f > 50$ Hz is much smaller than for $0 < f < 50$ Hz (see Fig. 5.8).
- In the pressure fluctuation measurements by Lopes et al. [12], Mollick and Sathiyamoorthy [13] and Wu et al. [6], the pressure fluctuations mainly happen for $f < 40$ Hz.

We calculate the average PSD value for U/U_{ms} = 0.99 to 1.44 and H_m = 0.05 to 0.35 m. The frequency range is from 0 to 50 Hz. The average PSD values are illustrated with colored blocks in Fig. 5.9. Red indicates strong fluctuations and blue weak fluctuations.

We found that for all flow rates, the middle position is most stable. The location of the spout close to the surface for very low flow rates and very high flow rates is slightly less stable than in the middle. Overall, the most stable state is found in $U/U_{ms} = 1.2 - 1.37$. Ren et al. [32] and Mollick et al. [33] suggested to use $U/U_{ms} \geq 1.2$ as a stable spout condition, which agrees with our measurement results.

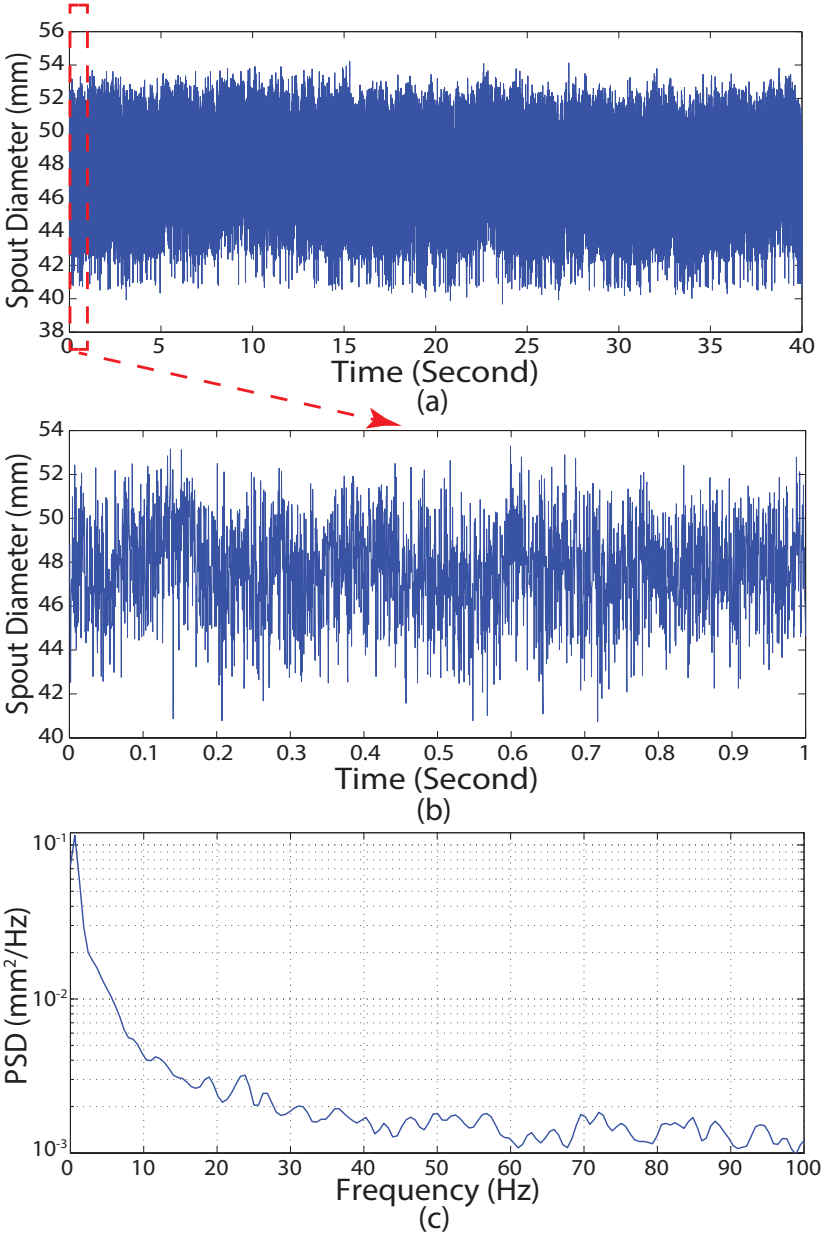

Figure 5.8: The fluctuation of spout diameter and PSD. $U/U_{ms} = 0.99$, $H_m = 0.04m$, sample frequency = 2500 Hz. (a) The spout diameter changes in 40 s; (b) The spout diameter changes in 1 s; (c) PSD of the spout diameter for 40 s.

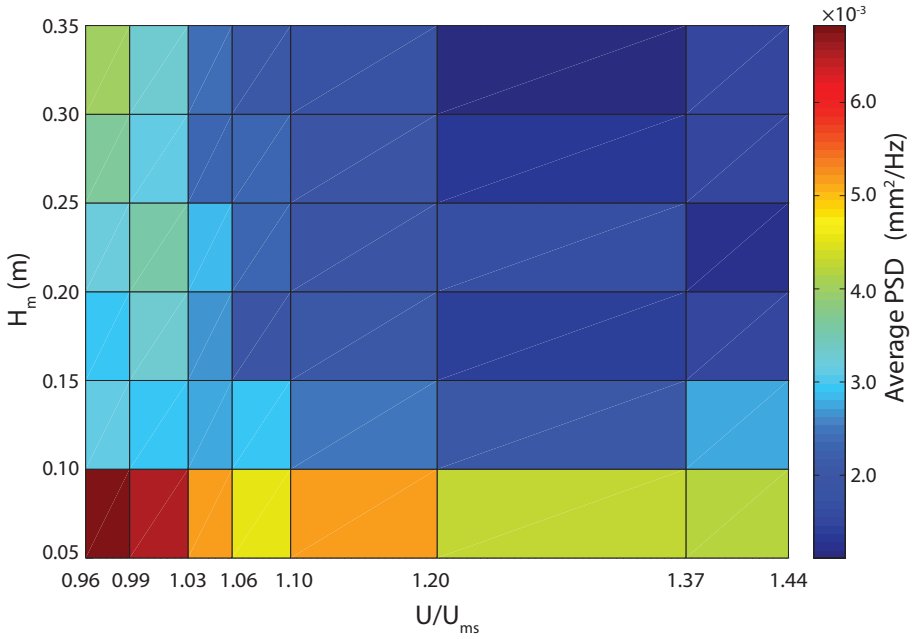

Figure 5.9: The average power spectral of spout diameter (0 to 50 Hz), U/U_{ms} = 0.99 to 1.44 , H_m = 0.05 to 0.35 m

5.6.2. The stability of spout position

The stability of the spout position is estimated from the movement of the spout center of gravity. The spout center $P(x, y)$ is a 2-D coordinate in the cross section of the bed. The bed is not always perfectly placed in the center of the measurement place. $P(x, y)$ is first rescaled by subtracting the mean value $\overline{P(x, y)}$. This step artificially moves $P(x, y)$ for different measurements to the same center. Then we average $P(x, y)$ for every 20 measurement points, to reduce the influence of system noise. By doing so, the sample frequency becomes 125 Hz. For easier visualization of the motion, we transfer $P(x, y)$ to polar coordinates $P(r, \theta)$.

In the bottom of the bed, the area visited by the jet is hardly influenced by the gas velocity. In the upper part of the bed, this area increases with increasing gas velocity (see Fig. 5.10)

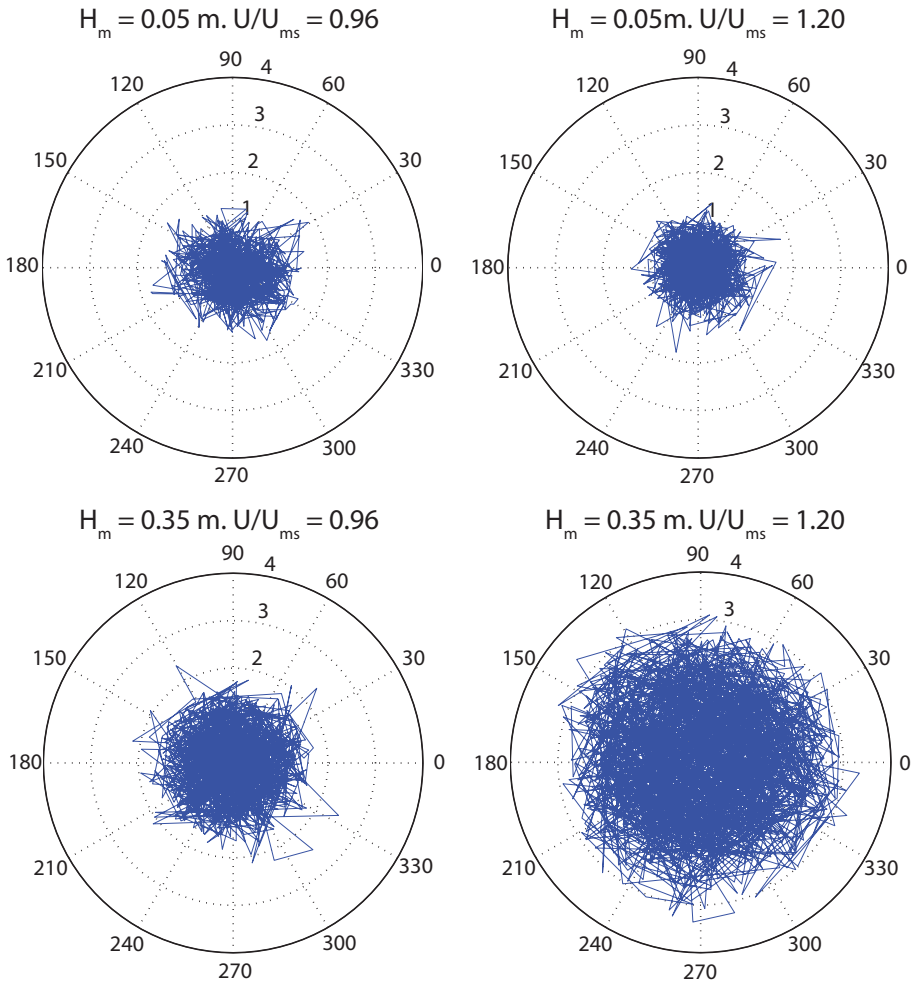

Figure 5.10: The trajectory for the movement of the spout gravity center. The unit of polar angle is degree. The unit of radius is mm. Sample frequency = 125 Hz. T = 10 s.

We plot the radial coordinate r and angular coordinate θ separately in Fig. 5.11. When $H_m = 0.05m$ and $U/U_{ms} = 0.99$, θ fluctuates randomly with a high frequency, and r mostly is smaller than 1 mm. The fluctuation of r has a high frequency and seems quite random. Because there is system noise from the measurement, we conclude that $P(r, \theta)$ stays the same position for this measurement condition. When $H_m = 0.35m$ and $U/U_{ms} = 1.20$, we observe in Fig. 5.11 from θ that the gravity center moves clockwise, and r fluctuates with a low frequency.

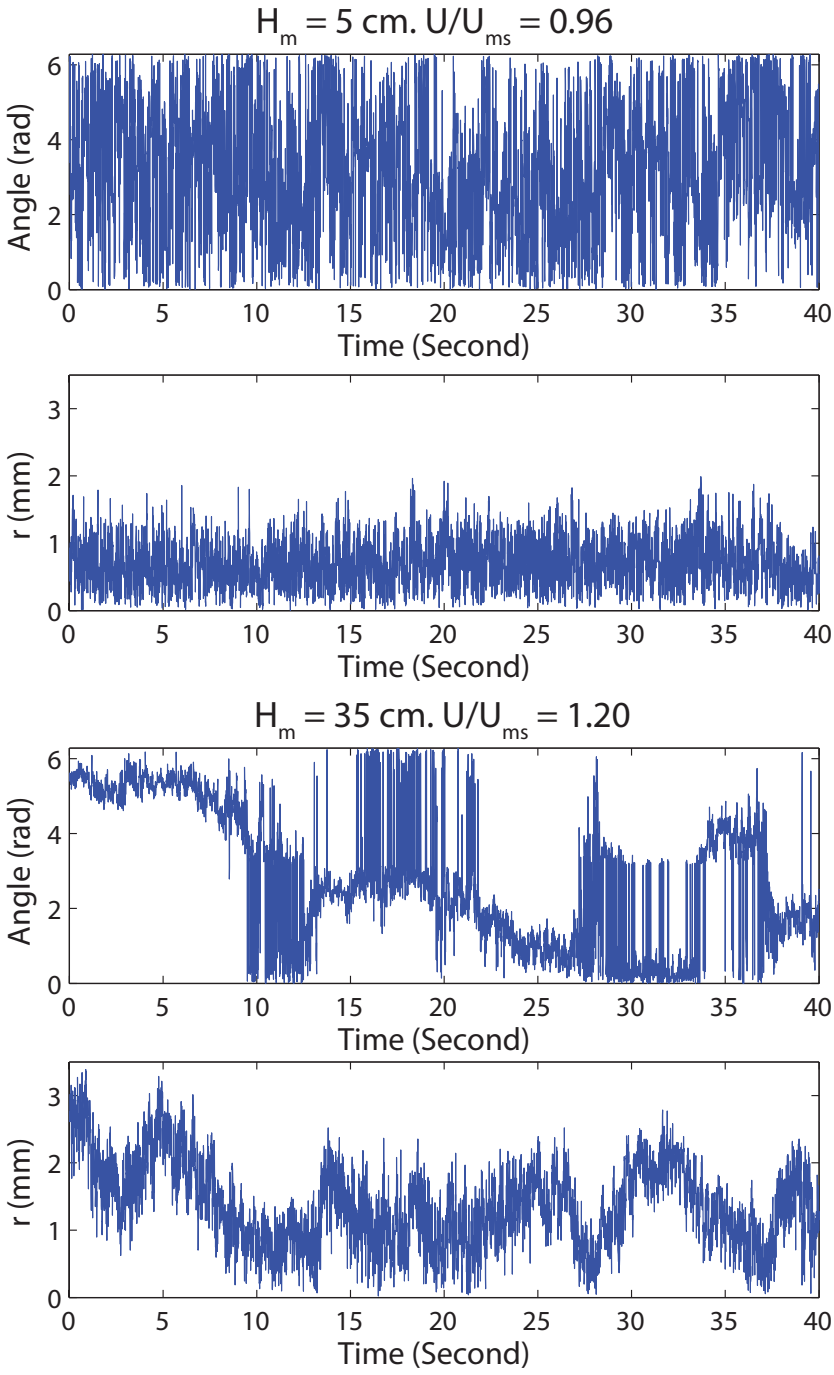

Figure 5.11: The spout position plotted with polar coordinate. Sample frequency = 125 Hz.

We compared the measurements for U/U_{ms} = 0.99 to 1.44 and H_m = 0.05 to 0.35 m. Opposite to the stability of the spout diameter (Fig. 5.9), the spout position is more stable at the bottom than at the surface. At the bottom position, the motion of the center of gravity is in a small area, with the radius mostly smaller than 1 mm. More likely, $P(r, \theta)$ is due to system noise. When H_m increases, the area of the spout motion increases. The radius is up to 3.5 mm when H_m = 0.35 m. Stronger fluctuations with low frequency can be found for the angle and radius when H_m increases.

5.7. Conclusion

The spout size and position in a spouted bed are considered constant in most of the literature. However, there are also reports about the pressure fluctuations in spouted bed. We use our high speed X-ray tomographic system to observe the spout dynamics directly. The tomographic reconstructions show that the spout size and position may change over time. However, the spatial resolution is too limited to estimate the change.

A more accurate analysis using the raw data was developed to obtain a sub-millimeter resolution. The time-averaged spout size shows rather good agreement with literature. We also developed a simple gas/solid flow model, by which the measured spout size is validated with the observed height to which particles are thrown up in a fountain by the spout.

The time-resolved spout size and position are also obtained from the raw data process. We found that the spout size fluctuates with a low amplitude. The most stable vertical position is in the middle of the bed. The most unstable position is close to the inlet of the jet. The most stable state happens for $U/U_{ms} \sim 1.3$ for the entire spout. The spout position is stable for low gas flow rates close to the bottom of the bed. There is a low frequency motion of the spout center of gravity in the upper part of the bed for higher gas flow rates. The case study shows good potential to detect the spout dynamics with the high speed X-ray system.

References

[1] K. B. Mathur, P. E. Gishler, A technique for contacting gases with coarse solid particles, Aiche Journal 1 (1955) 157–164.

[2] M. A. Malek, L. A. Madonna, B. C.-Y. Lu, Estimation of spout diameter in a spouted bed, Industrial & Engineering Chemistry Process Design and Development 2 (1963) 30–34.

[3] G. McNab, Prediction of Spout Diameter, British Chemical Engineering and Process Technology 17 (1972) 532–535.

[4] Y. He, C. Lim, J. Grace, J. Zhu, S. Qin, Measurements of Voidage Profiles in Spouted Beds, Canadian Journal of Chemical Engineering 72 (1994) 229–234.

[5] A.-L. He, C. J. Lim, J. R. Grace, S.-Z. Qin, Spout diameters in full and half spouted beds, Canadian Journal of Chemical Engineering 76 (1998) 702–706.

[6] C. Wu, Y. Cheng, Y. Ding, F. Wei, Y. Jin, A novel x-ray computed tomography method for fast measurement of multiphase flow, Chemical Engineering Science 62 (2007) 4325 – 4335.

[7] J. Bridgwater, K. B. Mathur, Prediction of spout diameter in a spouted bed—a theoretical model, Powder Technology 6 (1972) 183 – 187.

[8] E. Zanoelo, S. Rocha, Spout shape predictions in spouted beds, Canadian Journal of Chemical Engineering 80 (2002) 967–973.

[9] M. Olazar, M. Sanjose, F. Penas, A. Aguayo, J. Bilbao, Stability and Hydrodyanmics of Conical Spouted Beds with Binary-Mixtures, Industrial & Engineering Chemistry Research 32 (1993) 2826–2834.

[10] M. Olazar, M. Sanjose, A. Aguayo, J. Arandes, J. Bilbao, Design Factors of Conical Spouted Beds and Jet Spouted Beds, Industrial & Engineering Chemitray Research 32 (1993) 1245–1250.

[11] J. Xu, X. Bao, W. Wei, G. Shi, S. Shen, H. Bi, J. Grace, C. Lim, Statistical and frequency analysis of pressure fluctuations in spouted beds, Powder Technology 140 (2004) 141 – 154.

[12] N. Lopes, V. Moris, O. Taranto, Analysis of spouted bed pressure fluctuations during particle coating, Chemical Engineering and Processing: Process Intensification 48 (2009) 1129 – 1134.

[13] P. K. Mollick, D. Sathiyamoorthy, Assessment of stability of spouted bed using pressure fluctuation analysis, Industrial & Engineering Chemistry Research 51 (2012) 12117–12125.

[14] A. Kantzas, Computation of Holdups in Fluidized and Trickle Beds by Computer-Assisted Tomography, AIChE Journal 40 (1994) 1254–1261.

[15] A. Kantzas, I. Wright, N. Kalogerakis, Quantification of channelling in polyethylene resin fluid beds using X-ray computer assisted tomography (CAT), Chemical Engineering Science 52 (1997) 2023 – 2035.

[16] T. Grassler, K.-E. Wirth, X-ray computer tomography — potential and limitation for the measurement of local solids distribution in circulating fluidized beds, Chemical Engineering Journal 77 (2000) 65 – 72.

[17] T. J. Heindel, J. N. Gray, T. C. Jensen, An X-ray system for visualizing fluid flows, Flow Measurement and Instrumentation 19 (2008) 67–78.

[18] J. B. Drake, T. J. Heindel, Comparisons of Annular Hydrodynamic Structures in 3D Fluidized Beds Using X-Ray Computed Tomography Imaging, Journal of Fluids Engineering-Transactions of The ASME 134 (2012).

[19] R. F. Mudde, J. Alles, T. H. J. J. van der Hagen, Feasibility study of a time-resolving x-ray tomographic system, Measurement Science & Technology 19 (2008). 8th International Symposium on Measurement Technology and Intelligent Instruments, Tohoku Univ, Sendai, Japan, Sep. 24-27, 2007.

[20] M. Bieberle, F. Fischer, E. Schleicher, U. Hampel, D. Koch, K. S. D. C. Aktay, H.-J. Menz, H.-G. Mayer, Ultrafast limited-angle-type x-ray tomography, Applied Physics Letters 91 (2007).

[21] R. F. Mudde, Time-resolved X-ray tomography of a fluidized bed, Powder Technology 199 (2010) 55–59.

[22] R. F. Mudde, Bubbles in a fluidized bed: A fast X-ray scanner, AIChE Journal 57 (2011) 2684–2690.

[23] G. Brouwer, E. Wagner, J. van Ommen, R. Mudde, Effects of pressure and fines content on bubble diameter in a fluidized bed studied using fast X-ray tomography, Chemical Engineering Journal 207–208 (2012) 711 – 717.

[24] M. Bieberle, F. Barthel, U. Hampel, Ultrafast X-ray computed tomography for the analysis of gas-solid fluidized beds, Chemical Engineering Journal 189 (2012) 356–363.

[25] M. Olazar, M. S. José, A. Aguayo, J. Arandes, J. Bilbao, Hydrodynamics of nearly flat base spouted beds, The Chemical Engineering Journal and the Biochemical Engineering Journal 55 (1994) 27 – 37.

[26] K. B. Mathur, P. E. Gishler, A technique for contacting gases with coarse solid particles, Aiche Journal 1 (1955) 157–164.

[27] R. F. Mudde, Double x-ray tomography of a bubbling fluidized bed, Industrial & Engineering Chemistry Research 49 (2010) 5061–5065.

[28] X. Yang, J. R. van Ommen, R. F. Mudde, Comparison of genetic algorithm and algebraic reconstruction for x-ray tomography in bubbling fluidized beds, Powder Technology 253 (2014) 626–637.

[29] S. Takeuchi, S. Wang, M. Rhodes, Discrete element simulation of a flat-bottomed spouted bed in the 3-d cylindrical coordinate system, Chemical Engineering Science 59 (2004) 3495–3504.

[30] N. Rajaratnam, Turbulent Jets, Elsevier Science, pp. 27–48.

[31] P. D. Welch, The use of fast fourier transform for the estimation of power spectra: A method based on time averaging over short, modified periodograms, Audio and Electroacoustics, IEEE Transactions on 15 (1967) 70–73.

[32] B. Ren, Y. Shao, W. Zhong, B. Jin, Z. Yuan, Y. Lu, Investigation of mixing behaviors in a spouted bed with different density particles using discrete element method, Powder Technology 222 (2012) 85–94.

[33] P. K. Mollick, D. Sathiyamoorthy, P. T. Rao, V. G. Rao, Modeling of chemical vapor deposition of pyrolytic carbon in a gas-spouted bed reactor, Industrial & Engineering Chemitray Research 50 (2011) 13313–13321.

6

The Flow Pattern of a Downward Micro-Jet System

A downward micro-nozzle system is investigated for the fluidization of fine particles. To study the impact of the gas flow from the nozzle on the fluidization, the gas distribution below the nozzle is measured in a bed filled with 76 μm Puralox particles. A high speed X-ray tomography system, consisting of 3 X-ray sources and 2 layers of 32 detectors for each source, is employed to visualize the gas distribution with a temporal resolution of 2500 fps. Both the time-averaged and time resolved results are analyzed by combining the tomographic images from different measurement heights. A bubbling area, diluted area, and compacted area are found from the time averaged results. From time-series analysis, a stable bubbling flow is detected from both the cross-correlation of the raw data and image reconstruction. The penetration depth is also estimated. The results are validated with correlations from literature.

This chapter is based on the paper: Xiaogang Yang, J. Ruud van Ommen, and Robert F. Mudde. *Gas Distribution of a Downward Micro-nozzle Assisted Fluidized Bed of Fine Powder, Chemical Engineering Journal* 2015, 264, 945-953.

6.1. Introduction

A downward micro-nozzle system is a device to assist the fluidization by adding a second gas input via the nozzle for an additional shear force. There are two main features of this system: a downward gas flow from the nozzle, and a high gas injection velocity of the nozzle. Downward jets in 2-D fluidized beds have been studied by Shen et al. [1] and simulated by Hong et al. [2]. Better mixing and contacting of gas and solid is concluded from their research. In the study of a high velocity gas jet in a fluidized bed, Li et al. [3] suggest that a higher throughput is achieved at a low gas flow rate. Quevedo et al. [4] proposed a downward micro-nozzle system to enhance the fluidization of nano-particles.

Fluidization of nano-particles is often hampered by agglomeration problems, which make the gas-solid contacting inhomogeneous. Techniques such as mechanical vibration [5], sound vibration [6], alternating electric fields [7], and flow pulsation [8] have been developed to break the agglomerates. Alternatively, a downward micro-nozzle [9] was proposed to solve this problem. It is simple and works with only gas flow. Additional forces are not required, making it promising for industry application. However, voidage distribution in such a system has not yet been studied. The impact area and the flow pattern of the gas jet from the nozzle is difficult to predict. Direct observation of the gas-solid flow with a downward micro-nozzle has not been done. The conditions for fluidization of the nano-particles is rather difficult. To make an easy and equivalent observation for agglomerated nano-particles, we study a downward micro-nozzle assisted fluidized bed filled with a Geldart A particle.

In this paper, measurements of the dynamic flow pattern for a downward micro-nozzle system are carried out. Powders with mean size of 76 μm are used. We keep the fluidized bed at minimum fluidization and inject the gas through the micro-nozzle, which allows us to observe the influence from the nozzle only. A high speed X-ray tomography system [10, 11] is applied to scan the solid fraction distribution at several cross sections below the nozzle. We reconstruct 3-D images of the solid fraction to study the bed volume below the nozzle that is influenced by the gas coming from the nozzle. We reconstruct time-resolved pseudo 3-D images to show the gas flow through specific cross sections. The gas-particle flow pattern below the nozzle is discussed. To validate these measurements, the penetration depths of the jet in the fluidized bed is compared with correlations from literature.

6.2. Experimental Setup

6.2.1. The downward micro-nozzle system

The fluidized bed is held in a 14 cm inner diameter tube (perspex, wall thickness 5 mm). There are two gas inlets: a downward facing micro-nozzle and a distribution plate. The micro-nozzle is inserted from the top of the bed. It is directed downwards along the vertical axis of the bed. Its inner diameter at the outlet is 1.6 mm. The distribution plate which also supports the particles, is a porous plate

made from sintered bronze. The pore size is 30 to 70 μm and its thickness is 7 mm.

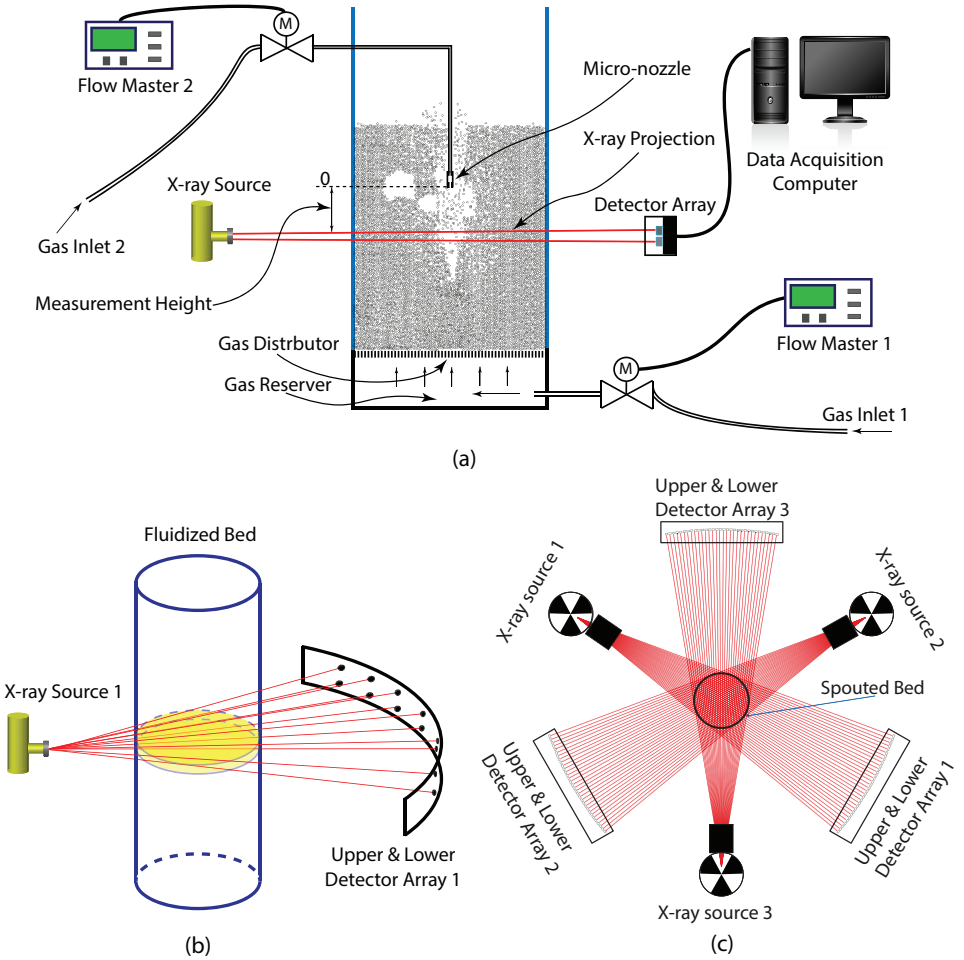

Figure 6.1: Setup of the downward nozzle system and high speed X-ray tomography system.

The column is filled up to a height of 45 cm with Puralox particles, with a mean diameter of 76 μm. The powder is Geldart type A. The bulk density is $1.29 \times 10^3 kg/m^3$. The mean density of packed Puralox is $710 kg/m^3$. The solid fraction of a packed bed is 0.55. In one set of experiments, we use tap water instead of particles in the same column.

The gas flows are provided by the distribution plate and micro-nozzle, respectively. The gas flow from the distribution plate keeps the particles at minimum fluidization condition: $U_{mf} = 0.21 cm/s$. The micro-nozzle provides an additional gas flow with a gas velocity at the nozzle exit ranging from 0.8×10^2 m/s to 3.3×10^2 m/s. Two

digital mass flow controllers (Bronkhorst E-7100-AAA) are used to set the gas flow rate, with a maximum error of 2%.

For the different nozzle diameters, we have prepared 4 sizes: 1.6mm, 0.8mm, 0.4mm, 0.2mm. With the maximum gas supply (7bar) in our lab, we cannot detect the difference from the X-ray measurement compared to the case without gas injection for the 0.4mm and 0.2mm nozzle. Apparently, the gas flow from these nozzles is too small to form a gas jet in the fluidized bed. For the 0.8mm nozzle, the gas flow of the nozzle is only stable when the flow rate is smaller than 10 L/min. It is very difficult to obtain series of data to compare with the 1.6mm nozzle. So we only present results of the 1.6mm nozzle in this article.

6.2.2. High speed X-ray tomography

The high speed X-ray tomography system developed by Mudde et al. [10] has been applied earlier for bubbling fluidized bed measurements [12–14]. It has been shown that this system is able to measure individual bubbles with an equivalent diameter larger than 2 cm in a fluidized bed of 24 cm diameter. For measuring the 14 cm fluidized bed in the current paper, the distance between X-ray sources and detector arrays are decreased. In this way, the concentration of the X-ray projection in the cross section of the bed is increased. As a consequence, gas voids which are larger than 1 cm can be detected with the current system.

In medical X-ray CT, the source and detector combination rotates slowly around the patient. This way sufficient viewing angles are gathered for a reconstruction with high spatial resolution. However, typically the rotation speed is 3 rounds per second which is way too low for studying dynamic phenomena such as bubble motion. Therefor, we use a high speed X-ray tomographic system that is composed of 3 X-ray tubes and 3 detector arrays. The X-ray sources are placed at 120° around the fluidized bed. The detector arrays are placed opposite to the X-ray sources. There are 2 parallel layers (10.8mm apart) of 32 detectors placed as arches in each detector array. Figure 6.1(b) shows the X-ray source and detector array. As is illustrated in Fig.6.1(c), this design makes it possible to simultaneously obtain the X-ray attenuation data from different directions, enabling reconstruction of the image of the object's cross section.

The X-ray sources are X-ray tubes manufactured by Yxlon International GmbH, with a maximum energy of 150 KeV. The tubes currents are set at 2 mA in the present measurements. The detectors are $CdWO_4$ scintilation detectors which are manufactured by Hamamatsu (type: S 1337 - 1010BR). The crystal size of the detector is $10mm \times 10mm \times 10mm$. The detectors are connected to a micro-computer to synchronize the data from all the detector arrays, with a sampling frequency of 2500 Hz. After each measurement, the data are transferred to a data acquisition workstation.

6.3. Tomographic Reconstruction

6.3.1. Calibration

The measured data is the X-ray intensity. We use the intensity difference to determine the attenuation difference of the X-ray traveled through different length of the object material. Mudde et al. [10] applied an exponential function to calculate the equivalent length (x, mm) of the X-ray traveled through the solid phase, from the X-ray intensity (I). In the current study, we found that a higher accuracy can be obtained by directly fitting the inversed function. It becomes:

$$x = C_{cal} \ln\left[\frac{B_{cal}}{I - A_{cal}}\right] \tag{6.1}$$

Here A_{cal}, B_{cal}, and C_{cal} are calibration coefficients. We fill 6 different parts of the cross sectional area, in order to have 6 specific values of x for each detector. After the related I is measured, A_{cal}, B_{cal}, and C_{cal} can be fitted from x and I in a calibration step for each detector individually.

6.3.2. Reconstruction process

We use a uniform Cartesian mesh to divide the computing domain in pixels. In the reconstruction, we estimate the solids volume fraction in each pixel. The values are stored in a vector (see Fig.3.1) rather than a matrix for computational reasons. When a given X-ray travels through the fluidized bed, it intersects a known length through each pixel of the mesh. All these lengths form the weighting matrix **W**. The solid fraction α_j is obtained by solving:

$$\tilde{p_i} = \sum_{j=1}^{N} W_{ij}\alpha_j \tag{6.2}$$

where $\tilde{p_i}$ is the i^{th} ray sum, which is the fraction of the line traveled by the i^{th} beam occupied by solids; W_{ij} is the weighting factor for the j^{th} pixel crossed by the i^{th} beam; α_j is the solid fraction of the j^{th} pixel.

A Simultaneous Algebraic Reconstruction Technique (SART) [15] is used for solving Eq.6.2. A One Step Late (OSL) [16] method is employed to eliminate the 'pepper and salt' noise [10]. SART works best for grids around $50 \times 50\ px^2$ for our conditions. OSL works better when the number of grid cells is bigger, because there is more freedom for OLS to smooth the 'pepper and salt' noise. We first use SART only to do reconstruction for a 50×50 pixel grid, see Fig.6.2(a) and (b). After 600 iterations, we double the grid to 100×100, and use OSL assisting SART for 50 iterations, see Fig.6.2 (c) and (d). The final reconstruction results, Fig. 6.2 (c) and (d) show similar patterns for the gas distribution as Fig. 6.2 (a) and (b), but without 'pepper and salt' noise. The maximum solid fraction also decreases to a reasonable range. The cross sectional images for the following analysis are all reconstructed

using the method of Fig. 6.2 (c) and (d).

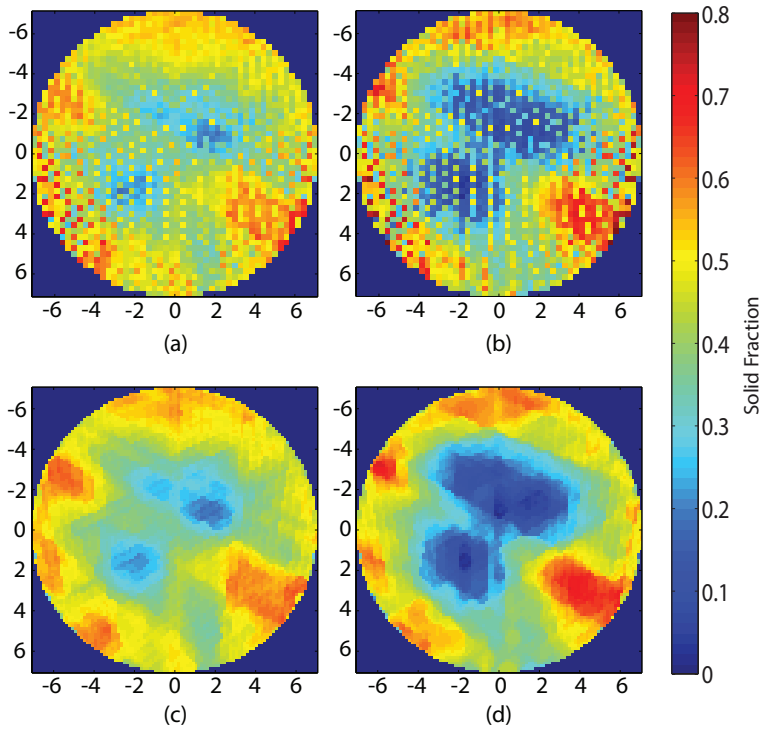

Figure 6.2: Examples of reconstructions from the double detector layers. The unit of the axis of the images is cm. (a) and (b) are the upper and lower plane reconstructed without OSL for the grid 50×50. (c) and (d) are the further reconstruction of (a) and (b) with a doubled grid and OSL. The maximum solid fraction for (a) and (b) is 0.8. It is 'pepper and salt' noise. The maximum solid fraction for (c) and (d) is 0.6.

We recently developed an alternative reconstruction approach based on a genetic algorithm [17], but in this case that approach is less suitable because it is only capable of reconstructing a binary image in current stage. It cannot determine transition areas and compacted areas in a fluidized bed, which we find in the current study.

Figure 6.2 shows 4 different regions for the solid fraction (α): the gas void (deep blue, $\alpha < 0.3$), the diluted area (green, $0.3 < \alpha < 0.5$), the fluidized area (yellow, $0.5 < \alpha < 0.55$), and the compacted area (red, $\alpha > 0.55$). The simultaneous results from the two detector layers show a phase difference for the same object at different measurement heights, which is the premise of the dynamic analysis of the gas voids. The accuracy of the reconstructions is not high enough to be absolutely sure about the solids fraction in the compacted area. However, the raw data show unambiguously that there are regions in the bed, that are more compact than the reference packed bed case (see below in section 6.4.1).

We collect the data at the maximum temporal resolution (2500 Hz). Every 10 samples are averaged for reconstructing an image. The temporal resolution thus reduces to 250 Hz. This is high enough to represent the dynamical changes of the bubbles, meanwhile, the system noise is reduced considerably.

6.4. Results & Discussions

6.4.1. Time-averaged solid fraction

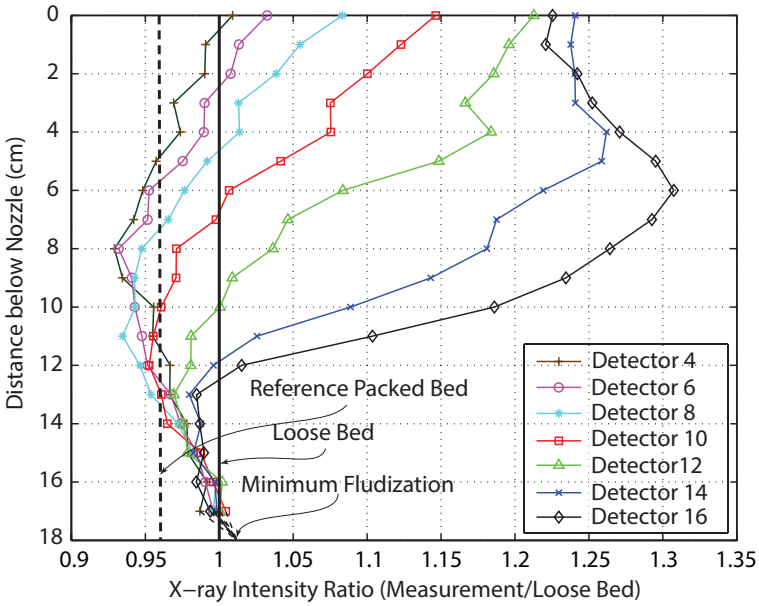

Figure 6.3: Ratio of X-ray intensity distribution. $v_n = 3.3 \times 10^2 m/s$. The detector number is the X-ray projections passing through a specific area of the cross section. The distribution of the X-ray projections is as Fig. 6.1 (c). For the number from 4 to 16, it represents the projection lines from very close the wall to the center of the bed.

We first present the influence of the jet by averaging 2 minutes of data.Coarsely speaking, the measured X-ray signals fluctuate periodically due to the presence of the jet (see Section 4.2). The oscillation period is roughly 0.1 s. So, averaging for 2 minutes effectively removes the periodic component.

Each detector measures the X-ray attenuation over a single line through the fluidized bed. There are 32 detectors for each source. All lines corresponding to a single X-ray source start in a point (the source) and form a fan-beam through the measuring plane. Detector 1 measures over a line that goes just through the 'left side' of the bed. Line two is passing through the bed slightly more to the center, but starts at

the same point in the source. Line 16 and 17 measure almost over a diameter of the bed and line 32 goes just through the 'right side' of the bed.

In Fig.6.3 we show the intensity ratio's as measured by the individual detectors of one of the sources. The ratio of detector i is made by dividing the measured intensity of detector i by the intensity measured by detector i for a loose bed. We plot only data from the left half of the bed; the right half gives very similar results. A higher value of the X-ray intensity ratio indicates a lower solid fraction on a measured line. The following is used to asses the phase distribution:

- when the ratio is higher than 1, there may be gas voids on the related line;
- when it is lower than 1 (the solid black line in Fig.6.3), there are areas on the line that are more compact than a loose bed;
- if it is lower than packed bed value (the dash line in Fig.6.3), part of the line is in a more compact state than the packed bed.

For each detector we measured the X-ray intensity for several reference states: packed bed, loose bed and minimum fluidization. We put the particles into the column without any additional force and consider this as the reference packed bed. We fluidize the bed fully for more than 5 minutes and slowly reduce the gas supply to the minimum fluidization condition, creating the reference for the minimum fluidization. The loose bed is measured after slowly shutting down the gas flow. For the packed bed, we find that the bed can be more compact by additional forces. The bed height decreases 1.6cm when we shake the packed bed. The average X-ray intensity for all the detectors decreases 4% approximately, which roughly agrees with the change of the solid fraction.

The superficial velocity through the bottom plate is set to the minimum fluidization velocity. The gas velocity through the nozzle is 3.3×10^2m/s. In Fig.6.3 it can be seen that 18 cm below the nozzle, the intensity ratio is higher than 1, i.e. the solids fraction is less then for the loose bed in agreement with the increase in voidage of a minimum fluidized bed with respect to the loose packed state. Closer to the nozzle there is a big air void in the central region of the bed (see Fig.6.3 e.g. detectors 14 and 16). This void disappears at a measurement height of about 12 cm below the nozzle. The other detectors also show gas voids close to the nozzle. When they are far away from the nozzle (below 13 cm), the particles may be more compact than loose bed. At the measurement height 5 to 12 cm, it is even a little more compact than the reference packed bed for the area close to the wall.

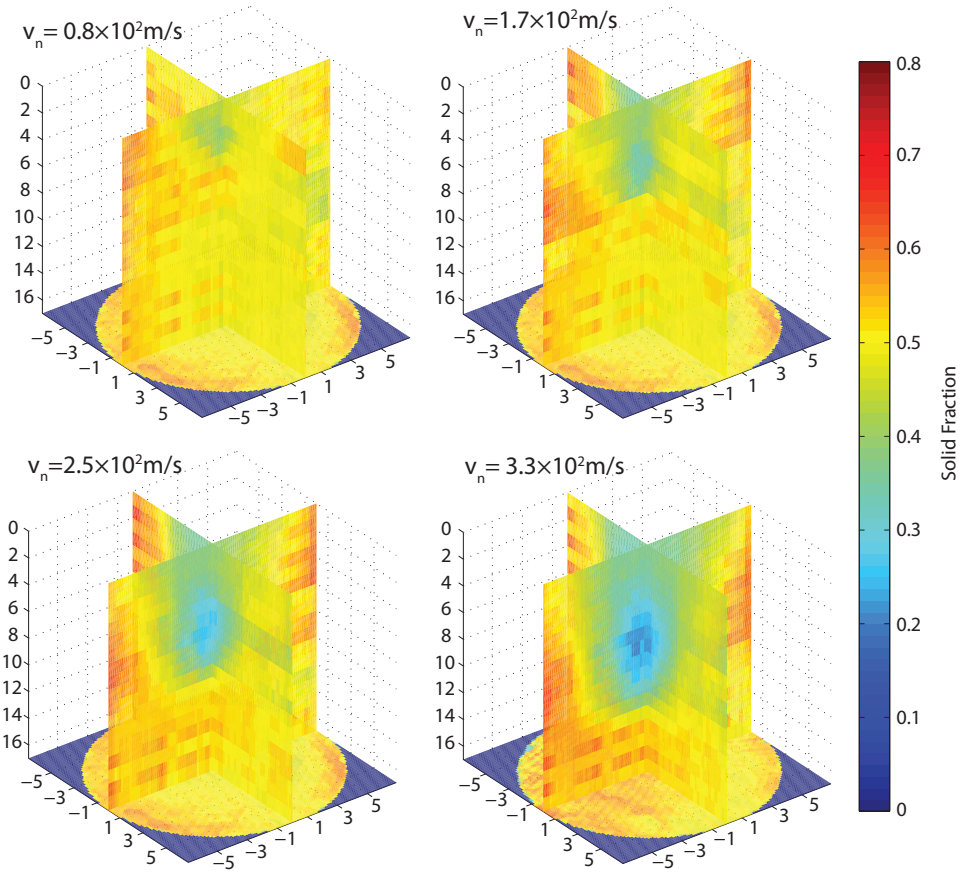

Figure 6.4: The solid fraction distribution below the nozzle for different nozzle gas velocities. The results are averaged over 2.5×10^5 frames ($2500fps \times 100s$). The maximum fraction is about 0.6. The unit for x,y,z axes of the images is cm.

We also reconstructed a 3-D image of the time-averaged solid fraction distribution below the nozzle (Fig.6.4) for cross sections from 0 to 17 cm below the nozzle, 1 cm for each step. The 3-D image of the solid fraction is reconstructed from the slices of different cross sections. The results show good agreement with the raw data analysis shown in Fig.6.3 for the outlet velocity of the nozzle (v_n) of 3.3×10^2 m/s. We find on average a big void at a height of 4 to 10 cm below the nozzle. There is a diluted area around the void. Also a compacted area around the diluted area is found. It is the same as we obtained from the raw data analysis.

For $v_n = 2.5{\times}10^2 m/s$, the phase distribution is similar as that for $v_n = 3.3{\times}10^2 m/s$. Only the void and diluted area are smaller and the gas fraction is a little less. The compact area is also less compacted. For $v_n = 0.8 \times 10^2$ and $1.7 \times 10^2 m/s$, wo do not see the void in the time-averaged results. Only the diluted area is found. However, this does not mean that there is no air bubble for these flow conditions.

We can determine the impact area of the nozzle from the time-averaged results, but the dynamic void is eliminated by the averaging. For all the flow conditions, we did not find a stream of gas blown out in a thin jet from the nozzle into the bubble. The reason may be that the outlet of the nozzle is very small (diameter 1.6 mm). The gas jet is too small to be determined with our X-ray system, which cannot image gas voids smaller than about 1 cm.

6.4.2. Dynamics of gas voids

The double layer of detectors allows us to do measurements simultaneously for two parallel cross sections. We apply cross-correlation to the detector layers to determine the phase lag and the regularity of the gas void fluctuations. The cross-correlation of the upper and lower plane $\gamma_{UL}(\tau)$ is calculated as:

$$\gamma_{UL}(\tau) = E[\epsilon_U(t)\epsilon_L(t+\tau)] \tag{6.3}$$

Here ϵ_U and ϵ_L are the line averaged solid fractions relative to reference data (loose bed) for the upper and lower plane, calculated as:

$$\epsilon(t) = \frac{1}{N}\sum_{n=1}^{N}\frac{L_n(t)}{\langle L_{refn}\rangle} \tag{6.4}$$

where L_n is the equivalent solid length of the n^{th} X-ray projection during measurements with the jet; $\langle L_{refn}\rangle$ is the equivalent length of the n^{th} X-ray projection for reference data, which is an averaged value over 100 s; N is the total number of detectors in one detector layer.

We obtain the direction of the void motion from the cross-correlation of the double plane. If a negative lag is obtained, the void moves from the lower to the upper plane. If it is positive, the motion is from upper to lower. When the lag is 0 and a periodic fluctuation of the correlation is observed, the void may oscillate up and down. With the help of this information, we reconstruct a pseudo 3-D image from the time-series slices, which are the tomographic images in a cross section. The pseudo 3-D image presents the change of the gas void, fluidized region, and compact region. Its vertical axis is time, rather than space.

The upper and lower detector plane are not parallel, but under a small angle as the two planes are formed from a fan beam of X-rays that is a collimated cone of photons coming out of the X-ray source. The plane-plane distance varies from 8.5 mm closest to the sources to 13.2 mm at the detector side of the column, with an average of 10.8 mm. We use the latter and the lag of the cross-correlation peak (which in itself is also an average of the cross-correlations of the corresponding pairs in the upper and lower plane) to estimate the velocity of the voids. The uncertainty in the velocity depends on further knowledge of the position of the void which can be found from the tomographic reconstructions. In the present work,

the voids travel through the center of the column with an estimated uncertainty in the position of their center of gravity of 10 mm. This gives an uncertainty in the plane-plane distance of 3%. The uncertainty in the estimated time lag is about 5%. This amounts to an uncertainty of 6% in the estimated velocity.

When $v_n = 3.3 \times 10^2 m/s$, regular fluctuations of the solid fraction can be found at H_m = 2 to 9 cm (Fig.6.5). A negative lag is found for H_m = 0 to 9 cm. It is about 0.014 s. This indicates bubbles moving upwards from H_m = 9 cm with a velocity of about $v_{bub} = 77$ cm/s. The amplitude of the fluctuations increase from lower to higher position. The period (T) of the fluctuations is about 0.12 s, which increases slightly from lower to higher position. These indicate that the equivalent size of the bubbles increases when they rise. The cross-correlations show a slowly decaying sinusoidal oscillation. This means that the bubbles pass the measurement planes at regular intervals, i.e. the bubble-bubble distance is fairly constant. From the period of 0.12 s and the estimate of the bubble velocity it thus follows that the bubble-bubble distance is $T \times v_{bub} = 8$ cm. The fluctuations disappear when H_m is bigger than 11 cm. We conclude that the influence of the gas jet ends at H_m = 11 to 12 cm. We call this the penetration depth (H_p). Summarized, we find that the gas jet penetrates to a depth of 11-12 cm below the nozzle into the bed. Around and above that depth bubbles are formed in a fairly regular process. These bubbles rise upwards at a velocity of about 77 cm/s. During one period one bubble is formed. Assuming that all gas that is injected during this period ends up in the bubble, we can estimate the equivalent bubble size. This gives $D_{eq} \approx 5.3$cm which is smaller than the estimated bubble-bubble distance as it should. From these estimates we can conclude that most of the gas that is injected via the nozzle ends up in bubbles.

The reconstructed results (Fig.6.9) show a similar pattern. Multiple bubbles in the cross sections of H_m = 0 to 3 cm are found. The bubble shape, size and distance between bubbles are not stable at H_m = 0 to 5, most likely due to coalescence and break up. The position of the center of gravity of the bubbles in the cross sections is mostly out of the center and fluctuates at these measurement heights. For H_m = 6 to 9 cm, single bubbles with quite regular size and shape are found. They are always in the center of the cross sections. The single bubbles from the different moments are attached to each other at H_m = 7 and 8 cm. For H_m = 10 and 11 cm, single gas voids with irregular patterns are found in the center of the cross section. We conclude that the jet reaches a depth of about 11 cm and there bubbles are formed that rise upwards while being 'pierced' by the downward jet. The jet itself cannot be seen in our reconstructions as it is most likely still thinner than our spatial resolution of 1 cm.

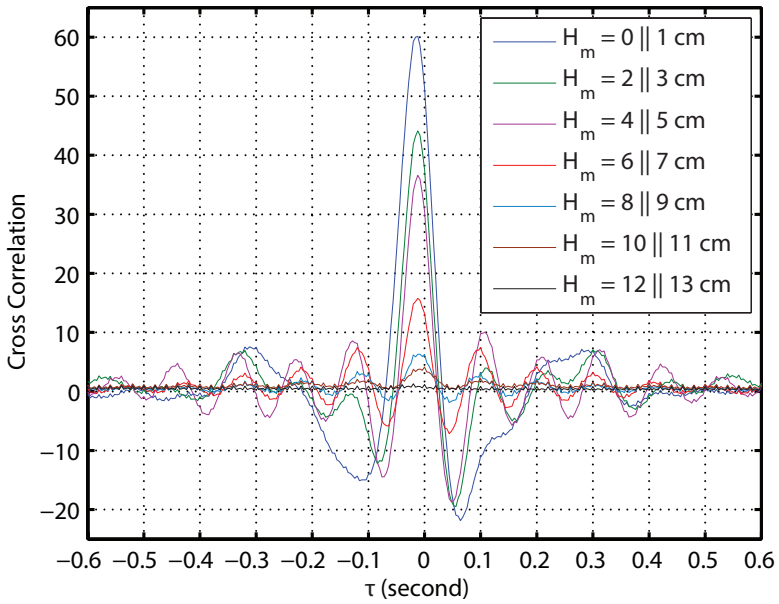

Figure 6.5: The cross correlation of the mean ratio of X-ray intensity between two measurement planes. $v_n = 3.3 \times 10^2 m/s$

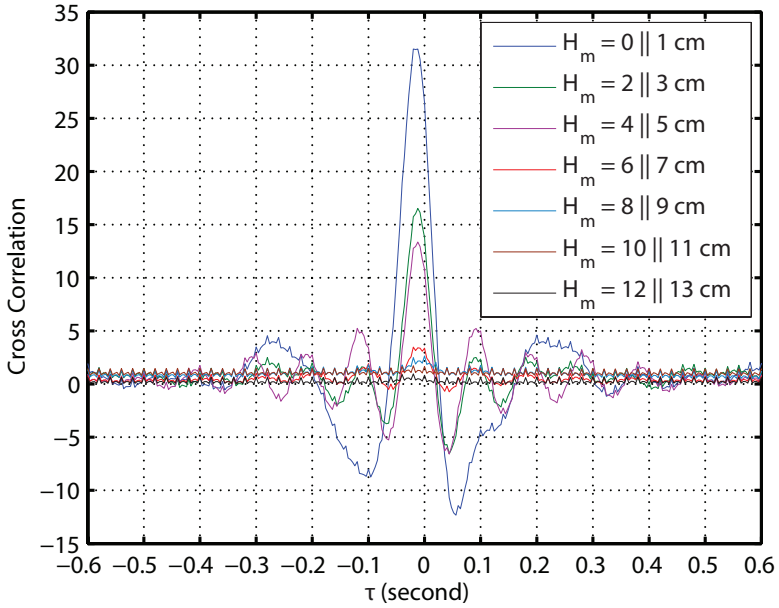

Figure 6.6: The cross correlation of the mean ratio of X-ray intensity between two measurement planes. $v_n = 2.5 \times 10^2 m/s$

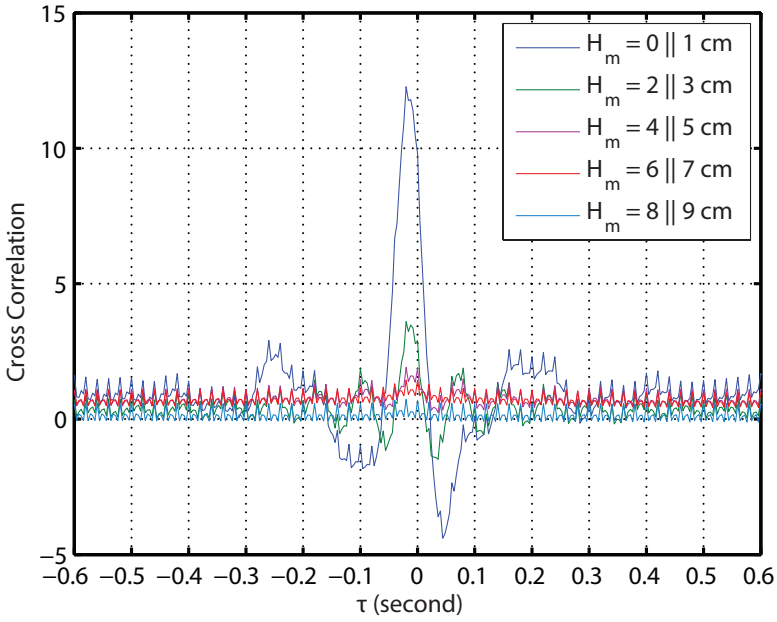

Figure 6.7: The cross correlation of the mean ratio of X-ray intensity between two measurement planes. $v_n = 1.7 \times 10^2 m/s$

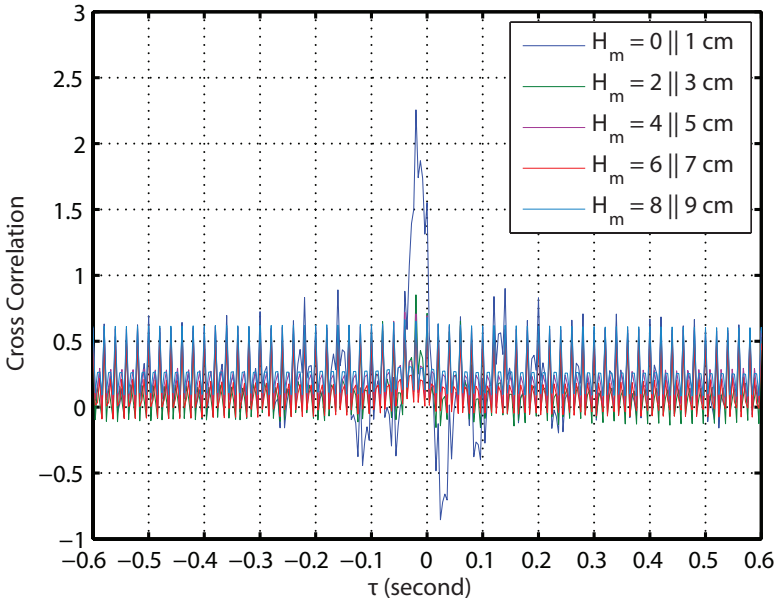

Figure 6.8: The cross correlation of the mean ratio of X-ray intensity between double measurement plane. $v_n = 0.8 \times 10^2 m/s$

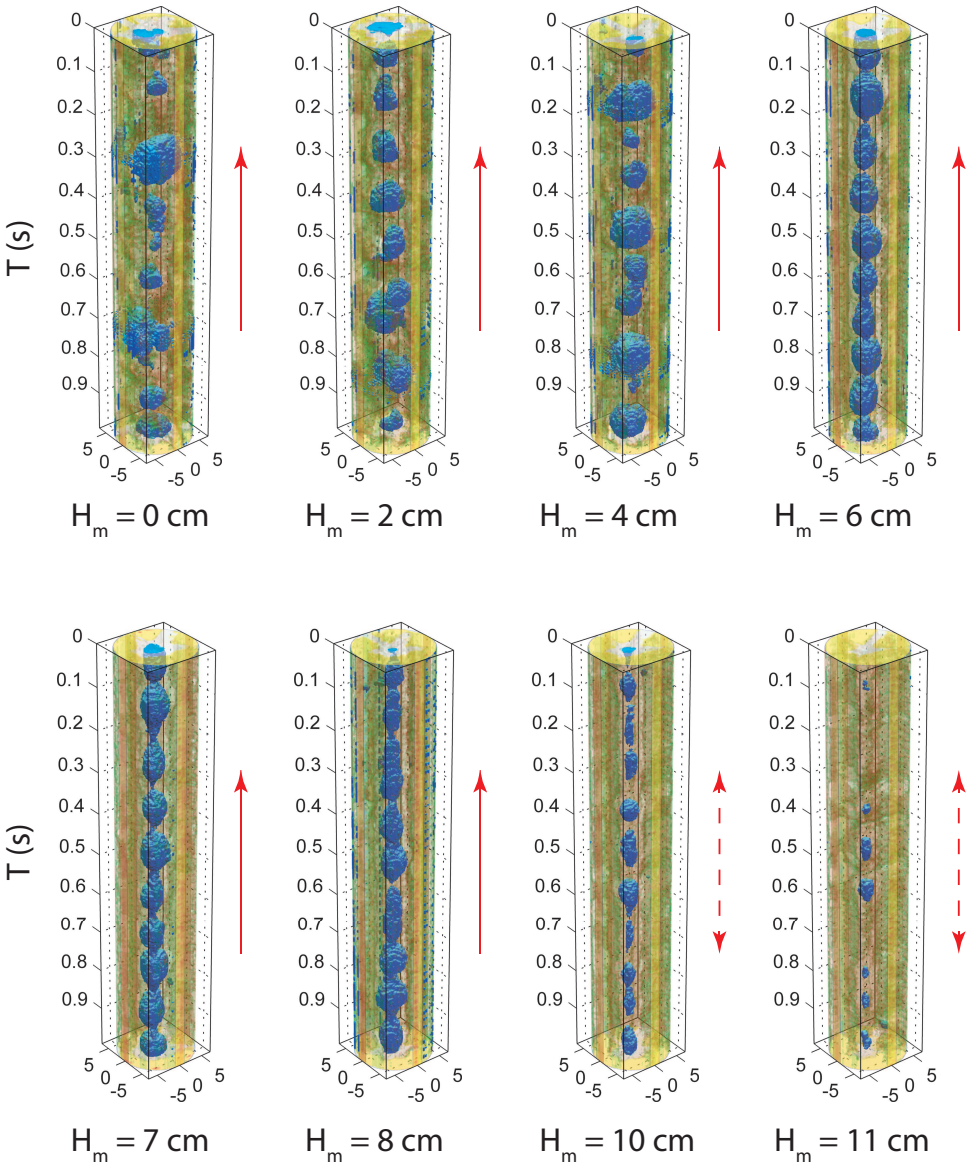

Figure 6.9: The pseudo 3-D images of gas voidage. $v_n = 3.3 \times 10^2 m/s$. Blue is the void region. Green is the diluted region. Red is the compacted region. Red arrow is the moving direction of the gas voids.

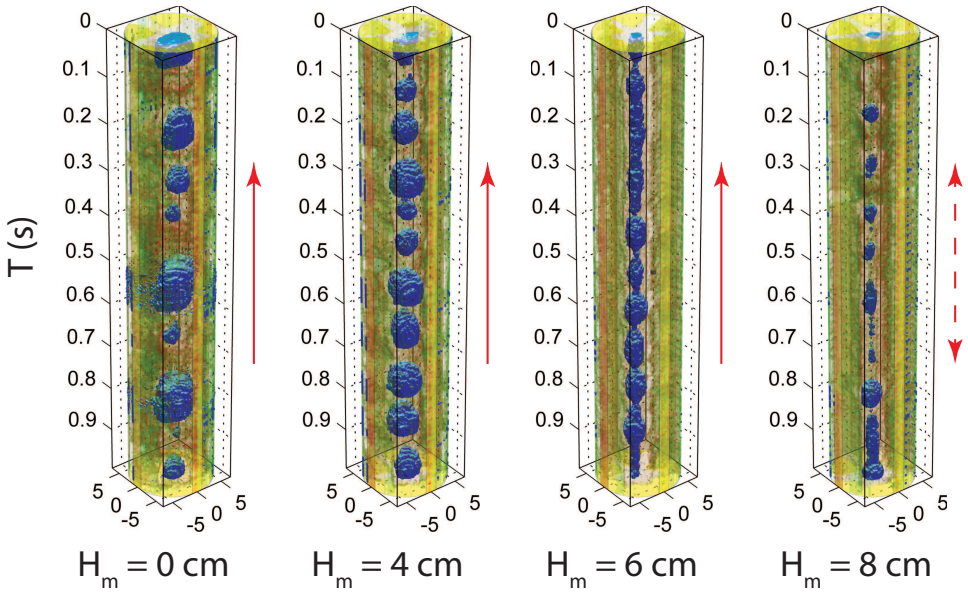

Figure 6.10: The pseudo 3-D images of gas voidage. $v_n = 2.5 \times 10^2 m/s$. Blue is the void region. Green is the diluted region. Red is the compacted region. Red arrow is the moving direction of the gas voids.

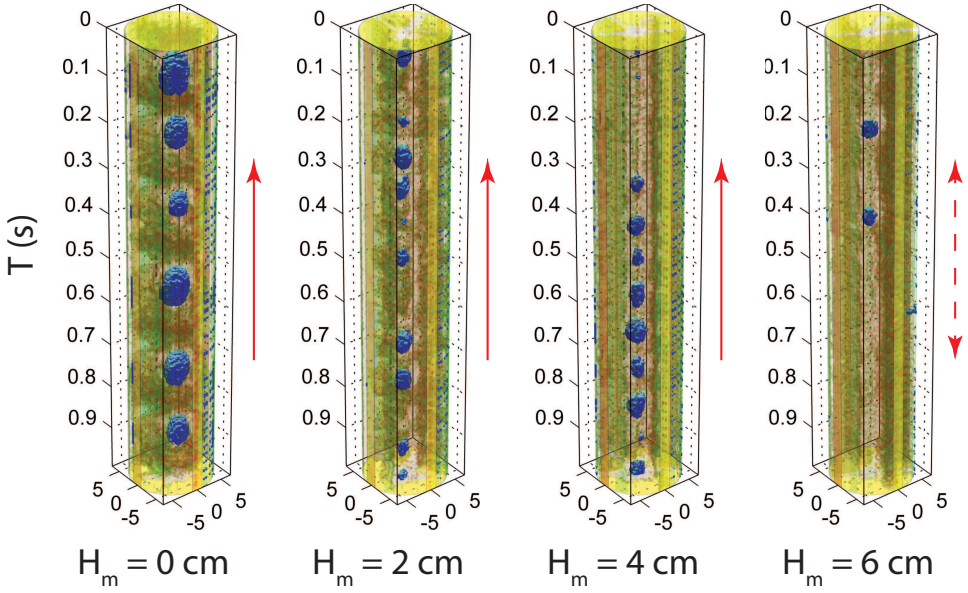

Figure 6.11: The pseudo 3-D images of gas voidage. $v_n = 1.7 \times 10^2 m/s$. Blue is the void region. Green is the diluted region. Red is the compacted region. Red arrow is the moving direction of the gas voids.

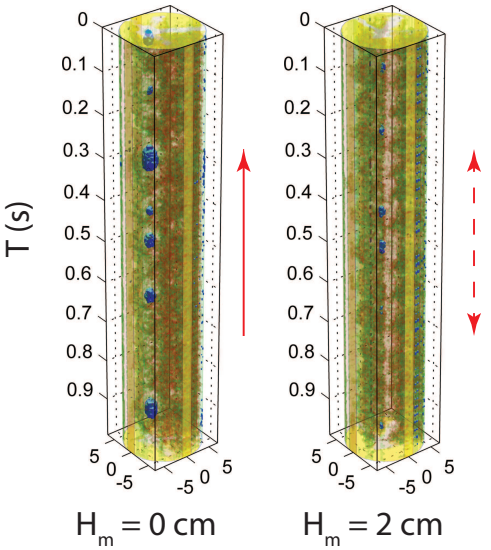

Figure 6.12: The pseudo 3-D images of gas voidage. $v_n = 0.8 \times 10^2 m/s$. Blue is the void region. Green is the diluted region. Red is the compacted region. Red arrow is the moving direction of the gas voids.

When $v_n = 2.5 \times 10^2 m/s$, similar flow patterns are found from cross-correlation and image reconstruction. For the cross-correlation (Fig.6.6), the magnitude is smaller than $v_n = 3.3 \times 10^2 m/s$. The penetration depth (H_p) is also smaller: about 9 to 10 cm. The value and direction of the time lag are similar. The period of fluctuation is also very close to the case $v_n = 3.3 \times 10^2 m/s$. From the reconstructed results (Fig.6.10), we do not detect multiple bubbles in the same cross section anymore, which can be find at H_m = 0-4 cm for $v_n = 3.3 \times 10^2 m/s$. We find that single bubbles are formed at H_m = 6-8 cm, which is closer to the nozzle than for $v_n = 3.3 \times 10^2 m/s$. The cross-correlation still shows sinusoidal behaviour: the bubble process is fairly regular.

When $v_n = 1.7 \times 10^2 m/s$, the pattern of gas flow is different. We do find a similar lag and fluctuations from the cross-correlation (Fig.6.7). The magnitude of the fluctuations and of H_p are smaller. From the image reconstruction (Fig.6.11b), we find that single bubbles are formed close to the nozzle (H_m = 4 cm) and they move up. Splitting and coalescence are not observed below the nozzle. The gap between bubbles is much bigger than for $v_n = 3.3 \times 10^2$ and 2.5×10^2 m/s. Moreover, the cross-correlation has lost its sinusoidal character, except for the lowest position of the jet, where the bubbles are formed.

When $v_n = 0.8 \times 10^2 m/s$, gas voids below the nozzle are hardly observed. Even though the velocity of the nozzle is $1/4$ of the first measurement, the magnitude of the cross-correlation (Fig.6.8) is less than $1/30$. We conclude that the momentum of gas flow from the nozzle is too small to form a gas jet. Most of the gas moves upwards because of buoyancy. We see a few small bubbles formed at the

outlet of the nozzle (H_m = 0 cm) from the reconstructed results (Fig.6.12). When $H_m > 0cm$, the magnitude of the cross-correlation (Fig.6.8) is too small to be distinguished from noise. The gas voids are rarely seen from the image reconstruction (Fig.6.12b, $H_m = 2cm$). We conclude that these voids are only the bottom boundary of the bubble.

6.4.3. Penetration depth

The penetration depth (H_p) is an important parameter for designing the nozzle system for the fluidized beds. It is a simple way to characterize the gas impact on the bed. We compare our measured H_p with the correlations for H_p from the literatures to validate our measurements.

A correlation for H_p of opposing jets has been proposed by Yates et al. [18]. In a study on inclined jets a correlation for H_p including a correction of the jet angle is proposed (see Hong et al. [19]), which seems also promising to calculate the downward jet. However, Sauriol et al. [20] recently showed that Yates et al. [18] agrees best with their experiment data, but still predicts a 50 % longer jet. For water jets, Emami and Briens [21] provided a correlation: $\frac{L_{jet}}{d_n} = 2.3155\left(\frac{\rho_g v_n^2}{\rho_{liq} g d_n}\right)^{0.3580}$, with L_{jet} the average penetration depth of the jet, d_n the inner diameter of the nozzle, ρ_g the gas density at the nozzle exit and ρ_{liq} the water density. We found similar flow patterns for the measurements in water and in the fluidized bed; see Appendix. It thus seems reasonable to apply an analogous correlation using the Froude number to describe our results. Based on our experiments, we propose:

$$\frac{H_p}{d_n} = \alpha\left(\frac{\rho_g v_n^2}{(\rho_b - \rho_g) g d_n}\right)^{\beta} \tag{6.5}$$

where α and β are coefficients, $\alpha = 2.14 \pm 0.1$ and $\beta = 0.37 \pm 0.02$ from fitting of our measurement; d_n is the inner diameter of the nozzle; ρ_g is gas density, ρ_b is the bulk density of the particles; g is gravity's acceleration.

We compare the correlations mentioned above with measured data. Our measurements (see Fig.6.13) agree with the conclusion of Sauriol et al. [20]. The predictions of Yates et al. [18] and Hong et al. [19] are about 50 % bigger than our measurements. Sauriol et al. [20]'s approach for the depth H_p agrees best with our data. Our correlation is easier, and it provides a good estimate at the higher gas velocities. However, there is a big deviation for all the correlations when $v_n < 1.7 \times 10^2 m/s$, where the flow pattern is much different from the high velocity cases. For higher velocities, our correlation gives a good description, though a more extensive data set is required to explore the extent of its validity.

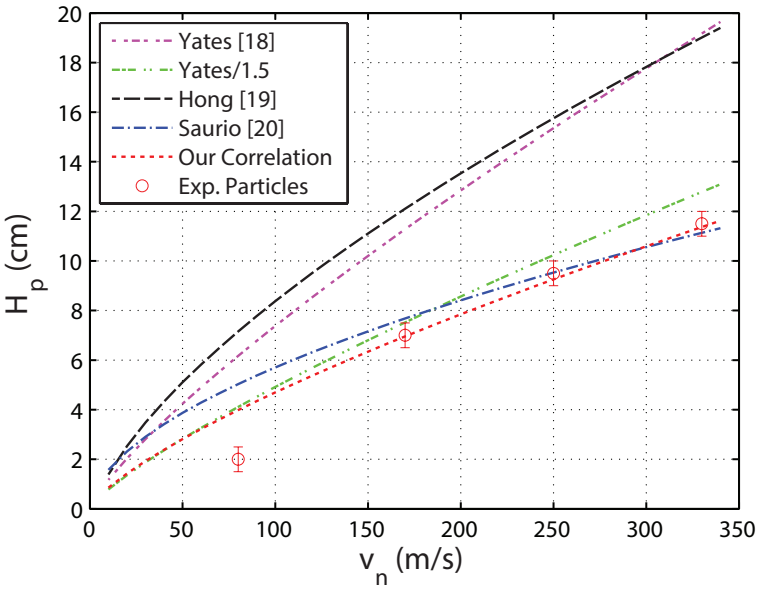

Figure 6.13: H_p for the downward micro-nozzle in the gas-solid system for our experiments and various correlations.

6.5. Conclusion

We use the high speed X-ray tomography system to observe the impact region and the time-resolved gas flow pattern below a downward micro-nozzle in the fluidized bed. A bubbling area, a diluted area, and a compact area are found from the time averaged reconstructions of the X-ray tomography. These agree with the direct analysis of the raw data. We find stable bubbling flow from the time-resolved reconstruction and the cross-correlation. Single bubbles are formed below the nozzle in the cross sectional center and move upwards. The bubbles expand, split and coalesce when moving upwards. The position of the bubbles rotates around the radial axis of the bed. By comparison of the bubble volume and the gas input from the nozzle, we find that most of the gas is injected via the nozzle ends up in bubbles. The gas jet itself is too thin to be observed from our reconstructions.

For $v_n = 1.7 \times 10^2 m/s$ to $3.3 \times 10^2 m/s$, the bubble size increases and the bubble-bubble distance decreases in the position where the bubble forms. Multiple bubbles are found in the same cross-sectional area for $v_n = 3.3 \times 10^2 m/s$, and single bubbles for the other value of v_n. For $v_n = 0.8 \times 10^2 m/s$, only a few small bubbles can be seen at the outlet of the nozzle, because most of the gas from the nozzle moves into the dense particle phase without forming gas voids.

The penetration depth of the gas jet is compared with the correlation from literature. The correlations based on Froude number show good agreement with our

measurement. Based on this, we propose a correlation for a downward micro-nozzle in a gas-solid fluidized bed.

References

[1] Z. Shen, C. L. Briens, M. Kwauk, M. A. Bergougnou, Study of a downward gas jet in a two–dimensional fluidized bed, The Canadian Journal of Chemical Engineering 68 (1990) 534–540.

[2] R. Hong, J. Ding, H. Li, Fluidization of fine powders in fluidized beds with an upward or a downward air jet, China Particuology 3 (2005) 181–186.

[3] F. Li, C. Briens, F. Berruti, J. McMillan, Particle attrition with supersonic nozzles in a fluidized bed at high temperature, Powder Technology 228 (2012) 385–394.

[4] J. A. Quevedo, A. Omosebi, R. Pfeffer, Fluidization enhancement of agglomerates of metal oxide nanopowders by microjets, AIChE Journal 56 (2010) 1456–1468.

[5] J. M. Valverde, A. Castellanos, Effect of vibration on agglomerate particulate fluidization, AIChE Journal 52 (2006) 1705–1714.

[6] A. Ajbar, Y. Bakhbakhi, S. Ali, M. Asif, Fluidization of nano-powders: Effect of sound vibration and pre-mixing with group a particles, Powder Technology 206 (2011) 327–337.

[7] D. Lepek, J. M. Valverde, R. Pfeffer, R. N. Dave, Enhanced nanofluidization by alternating electric fields, AIChE Journal 56 (2010) 54–65.

[8] S. S. Ali, M. Asif, Fluidization of nano-powders: Effect of flow pulsation, Powder Technology 225 (2012) 86–92.

[9] R. Pfeffer, J. Quevedo, J. Flesch, Fluidized bed systems and methods including micro-jet flow, 2013. US Patent 8,439,283.

[10] R. F. Mudde, J. Alles, T. H. J. J. van der Hagen, Feasibility study of a time-resolving x-ray tomographic system, Measurement Science & Technology 19 (2008). 8th International Symposium on Measurement Technology and Intelligent Instruments, Tohoku Univ, Sendai, Japan, Sep. 24-27, 2007.

[11] R. F. Mudde, Time-resolved X-ray tomography of a fluidized bed, Powder Technology 199 (2010) 55–59.

[12] R. F. Mudde, Double x-ray tomography of a bubbling fluidized bed, Industrial & Engineering Chemistry Research 49 (2010) 5061–5065.

[13] R. F. Mudde, Bubbles in a fluidized bed: A fast X-ray scanner, AIChE Journal 57 (2011) 2684–2690.

[14] G. Brouwer, E. Wagner, J. van Ommen, R. Mudde, Effects of pressure and fines content on bubble diameter in a fluidized bed studied using fast X-ray tomography, Chemical Engineering Journal 207–208 (2012) 711 – 717.

[15] A. Andersen, A. Kak, Simultaneous Algebraic Reconstruction Technique (SART): A superior implementation of the ART algorithm, Ultrasonic Imaging 6 (1984) 81 – 94.

[16] S. Alenius, U. Ruotsalainen, Bayesian image reconstruction for emission tomography based on median root prior, European Journal of Nuclear Medicine and Molecular Imaging 24 (1997) 258–265.

[17] X. Yang, J. R. van Ommen, R. F. Mudde, Comparison of genetic algorithm and algebraic reconstruction for x-ray tomography in bubbling fluidized beds, Powder Technology 253 (2014) 626–637.

[18] J. G. Yates, S. S. Cobinah, D. J. Cheeseman, S. P. Jordan, Particles attrition in fluidized beds containing opposing jets, AIChE Symposium Series 87 (1991) 13–19.

[19] R. Y. Hong, Q. J. Guo, G. H. Luo, J. Y. Zhang, J. Ding, On the jet penetration height in fluidized beds with two vertical jets, Powder Technology 133 (2003) 216–227.

[20] P. Sauriol, H. Cui, J. Chaouki, Gas jet penetration lengths from upward and downward nozzles in dense gas–solid fluidized beds, Powder Technology 235 (2013) 42 – 54.

[21] A. Emami, C. Briens, Study of downward gas jets into a liquid, AIChE Journal 54 (2008) 2269–2280.

7

Conclusions and Outlook

High speed X-ray tomography is a powerful tool to measure the time-resolved gas distribution in fluidized beds. Its measurement accuracy can be improved by novel approached for data processing and image reconstruction. In this project, we measured two kinds of gas jets in fluidized beds: a spout in a spouted bed of Geldart group D particles, and a gas jet from a downward micro-nozzle in a fluidized bed for the Geldart group A powders. From these studies, we developed novel methods to solve the tomographic reconstruction problem. We obtained the flow pattern of the gas jets at a high temporal and spatial resolution. In this chapter, we will summarize the main achievements of this dissertation and also discuss directions of future work for future researchers.

7.1. Conclusions

High speed X-ray tomography is introduced in Chapter 2. Its basics are similar to conventional X-ray tomography for medical imaging. The main difference is that it scans the object from different angles simultaneously with multiple sources, instead of rotating the X-ray source and detector array. This method enables high temporal resolution (up to 2500 Hz) measurement, which is of key importance for measuring the dynamics of the fluid flow. Moreover, the high speed X-ray tomography is a *hard field tomography*, i.e. with straight field lines. Its image reconstruction is less troublesome than for *soft field tomography*, such as ECT. It is also easier to get a higher spatial resolution. These make the high speed X-ray tomography a promising tool for the dynamic measurement of the fluidized beds.

In Chapter 3 and 4, we studied the reconstruction algorithms of high speed X-ray tomography. It has less data points for image reconstruction than conventional X-ray tomography, which makes the reconstruction problems more ill-posed. The novel reconstruction algorithms are expected to improve the accuracy of the measurement results under the limited hardware condition. We first compared the Simultaneous Algebraic Reconstruction Technique (SART) and an Adaptive Genetic Algorithm (AGA) in Chapter 3, then developed a hybrid algorithm to combine the advantages of these two algorithms in Chapter 4.

From the comparison between SART and AGA, we found that both of the algorithms have their advantage and disadvantages. From the case studies with synthetic data for the bubble voids in a fluidized bed, we simulated the performance of SART and AGA. AGA performs much better than SART for low spatial resolution reconstructions (20×20 and 30×30 pixels). The accuracy of AGA goes down for fine meshes (50×50), and the computing time strongly increases. There is not a clear trend for SART when the resolution increases. In the cases we tested in this dissertation, we always found the best performance for a mesh of 40×40 pixels. However, this may be different for other cases with different numbers and sizes of phantoms. The presence of noise strongly influences SART; AGA is less sensitive to noise. The disadvantage of AGA is its variation in results due to its stochastic nature. Varying results were obtained for the same case when reconstruction images with higher spatial resolutions (40×40 and up in our case).

SART has the advantage to reconstruct an accurate shape of the phantoms, but produces too much noisy pixels outside the true objects. It also smears small objects. AGA is improved compared with simple GA regarding the convergence. However, the shapes AGA reconstructs are often not accurate, because of its global estimation of such a system with so many variables. We found that the features of SART and AGA are complementary. A combination is tested in chapter 4. From the cases with synthetic data and experimental data, we found that the hybrid algorithm reconstructs the results with better accuracy than SART or AGA separately.

After the algorithm studies for the high speed X-ray tomography, we used this setup

to measure gas jets in the fluidized beds. The spout in a spouted bed is a gas jet of centimeter scale. We measured the dynamics of it in Chapter 5. The spout size and position in a spouted bed are considered constant in most of the literature. However, there are also reports about pressure fluctuations in spouted beds. We used our high speed X-ray tomographic system to observe the spout dynamics in a direct way. The tomographic reconstructions show that the spout size and position may change over time. However, the spatial resolution is too limited to estimate the change.

A more accurate analysis using the raw data was developed to obtain a sub-millimeter resolution. The time-averaged spout size shows rather good agreement with literature. We also developed a simple gas-solid flow model, by which the measured spout size is validated with the observed height to which particles are thrown up in a fountain by the spout.

The time-resolved spout size and position are also obtained from the raw data process. We found that the spout size fluctuates with low amplitude. The most stable position is in the middle of the bed. The most unstable position is close to the inlet of the jet. The most stable state happens for $U/U_{ms} \sim 1.3$ for the entire spout. The spout position close to the bottom of the bed is stable for low gas flow rates. There is a low frequency motion of the spout center of gravity in the upper part of the bed for higher gas flow rates. The case study shows good potential to detect the spout dynamics with the high speed X-ray system.

Another gas jet, a gas jet below a downward facing micro-nozzle system is studied in Chapter 6. We used the high speed X-ray tomography system to observe the impact region and the time-resolved gas flow pattern below a downward micro-nozzle in the fluidized bed. A bubbling area, a diluted area, and a compacted area are found from the time averaged reconstructions of the X-ray tomography. These agree with the direct analysis of the raw data. We find stable bubbling flow from the time-resolved reconstruction and the cross-correlation. Single bubbles are formed below the nozzle in the cross sectional center and move upwards. The bubbles expand, split and coalesce when moving upwards. The position of the bubbles rotates around the radial axis of the bed. By comparison of the bubble volume and the gas input from the nozzle, we find that most of the gas injected via the nozzle ends up in bubbles. The gas jet itself is probably too thin to be observed from our reconstructions.

We compared the flow pattern for different gas velocities through the nozzle. For $v_n = 1.7 \times 10^2 m/s$ to $3.3 \times 10^2 m/s$, the bubble size increases and the bubble-bubble distance decreases at the position where the bubbles are formed. Multiple bubbles are found in the same cross-sectional area for $v_n = 3.3 \times 10^2 m/s$, and single bubbles for the other values of v_n. For $v_n = 0.8 \times 10^2 m/s$, only a few small bubbles can be seen at the outlet of the nozzle, because most of the gas from the nozzle moves into the dense particle phase without forming gas voids.

The flow pattern is similar to a downward micro-nozzle in water for similar flow conditions. A similar impact region and penetration depth are found from our direct observation in water. The bubbles form at similar positions with similar sizes. The rotation of the bubbling region is also observed. Our results and conclusions are validated by correlations of the penetration depth.

7.2. Outlook

Although the accuracy of the high speed X-ray tomography can be improved by the software improvements, we cannot break the fundamental limits with the software methods. An increase of the number of X-ray sources or the number of detectors is the most promising way to improve the spatial resolution and measurement accuracy.

We simulate the performance of the hybrid algorithm for different numbers of X-ray sources and detectors as shown in Fig. 7.1. We design a rather difficult case. Five phantoms with diameters of 1.5 to 5.5cm are placed in a 24 cm diameter fluidized bed. We use the hybrid algorithm, which is the most accurate reconstruction algorithm for the high speed X-ray tomography until now. By using the current setup, we find inaccurate shapes for all the phantoms and wrong positions for small phantoms (1.5 and 2.5cm).

When we double the number of the detectors, the smallest phantom (1.5cm) still cannot be reconstructed in its correct position (Fig. 7.1 (b)). The shapes and the positions for the 2.5cm, 3.5cm, and 4.5cm phantoms are more accurate than from the current setup. Both the current setup and the doubled detectors have the problem that the biggest phantom becomes bigger and the small phantoms become smaller or even disappear. The improvement of increasing the detector number is limited. It is not a cost-effective approach.

A dramatic improvement is found when we increase the number of X-ray tubes from 3 to 5. As Fig. 7.1 (c) shows, all the phantoms are found at their right position with almost perfect shape at the current resolution. Although, the smallest phantom is not totally black, we can still distinguish it from the noise pixels. Besides, we have simulated different cases by using different reconstruction algorithms for increasing number of X-ray tubes, and they all show remarkable improvements of the reconstruction results.

The hybrid algorithm efficiently combines the advantage of SART and AGA. However, the computing time is a problem because we run AGA many times in one computation. AGA is a very time consuming algorithm as we have evaluated in chapter 3. In the current stage, the hybrid algorithm costs more than one hour for one image reconstruction with the coding of Matlab. For measurements with a temporal resolution of 2500 Hz, it is too slow to reconstruct the images of thousands

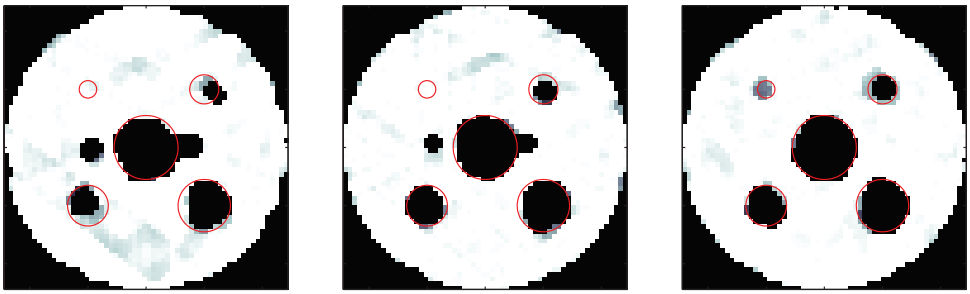

Figure 7.1: The further improvement for the high speed X-ray tomography. The results are simulated from a synthetic data of the phantoms in a 24 cm fluidized bed. The phantom sizes are 1.5 cm, 2.5 cm, 3.5 cm, 4.5 cm and 5.5 cm. The mesh is 50×50 pixels. The reconstructions are done by the hybrid algorithm (see Chapter 4). (a) The current setup (3 X-ray tubes, 32 detectors per each detector array); (b) Increasing the detectors (3 X-ray tubes, 64 detectors per each detector array); (c) Increasing the X-ray tube (5 X-ray tubes, 32 detectors per each detector array).

of seconds measurements. We can only use it to check some samples accurately. The use of programming language influences the speed very much. When we transferred the SART code from Matlab to Fortran, the computational time was reduced by a factor of hundred. We expect that an even more spectacular decrease can be obtained if we transfer the AGA code from Matlab to Fortran or C, because there are much more iterations in AGA than in SART. These iterations slow down the computing in Matlab.

Parallel computing is an efficient way to speed up the hybrid algorithm. For AGA only, Graphics Processing Unit (GPU) can speed up the computing by a factor of hundred compared to a CPU[1]. For the hybrid algorithm, if we use a GPU cluster to distribute the different runs of AGA to its slaves, the long computation times of AGA in the hybrid algorithm can be avoided. These methods to speed up the hybrid algorithm have not been tested during our previous research. Optimization of the coding and testing for the parallel computing would be necessary for application of the hybrid algorithm.

In the measurements of the spouted bed, we have evaluated the changing spout stability with changing gas flow rate. However, Olazar et al. [2] have claimed that the stability is related to the ratio of bottom orifice diameter and particles diameter, and the ratio of the orifice diameter and the column diameter. Mollick and Sathiyamoorthy [3] have found that the standard deviation of pressure fluctuation is a strong function of fluid-particle properties and bed geometries. They suggest using these criteria for estimating the stable regime of the spouted bed. Therefore, in the next step of the research, the parameters such as the particles diameter, density, and the geometry of the bed should be considered when determining the stability of the spout.

We have measured the fluctuation of the spout diameter and the oscillation of the spout position. The validation of these results has been carried out indirectly, by comparing the averaged spout diameter with literature and a simple flow model. However, there is not any mathematical model available to quantify our results. Are these fluctuation and oscillation predictable by mathematical calculation? If so, are the fluctuation and oscillation regular or totally chaotic? To solve these problems, an instantaneous flow model for gas-particle flow in the spouted bed is needed.

We also developed a simple model for the particle circulation in a spouted bed. It is based on the spout diameter from our X-ray measurements. This model has been validated by the measurements for the fountain height of the spouted bed. It has the advantage of the simple structure and fast computing, because the 3-D gas-particle flow is simplified to 1-D mass, momentum and energy transport. The results are accurate enough for engineering use in our case. However, it would be good to elucidate how it performs for other cases, and what its limitations are. We suggest two ways for further validation: more measurements for different properties, and comparison with different numerical models. For further measurements, the particle velocity in the spout, the fountain, and the annulus, which can be calculated by this model, can be compared. For the numerical comparison, there are different flow models [4–8] for the spouted beds. In future studies, the comparison between our model and other models for the same cases will be valuable.

The downward micro-nozzle in a fluidized bed is another kind of gas jet we considered. Our final purpose of this study is to improve the fluidization of nano-particles. However, in the current stage, we only carried out measurements for micro-scale particles, due to challenges involved in working with the nano-particles. Regarding the measurement technique, the calibration data is difficult to obtain for nano-particles because of the very low and varying bulk density. Moreover, extensive safety measure will be required when working with nano-particles, especially in a large volume. Currently, some first measurements of nano-particle fluidization in the tomography setup are carried out by another researcher in our lab.

We only presented the results for a 1.6mm nozzle. The measurements of the smaller nozzles were not successfully carried out, as the pressure of the gas supply is too low. For a smaller diameter of the nozzle, a higher velocity can be provided with the same gas flowrate. We would like to provide a high gas velocity from the nozzle, because it may help to break the agglomerates. However, we also like to have a relatively small superficial gas velocity in the fluidized bed, for saving gas supply and keeping a relatively stable flow. Therefore, smaller nozzles should perform better than the current nozzle for our objectives. To verify this deduction, real tests with smaller nozzle are needed. In addition, we have only tested a single nozzle in the bed. What will be the interaction for multiple nozzles? This will be an interesting topic, in case the spatial resolution of the X-ray system is high enough.

During the test with the downward micro-nozzle system, the gas supply from the distributor is kept at the minimum fluidized velocity. The purpose is to focus on the flow pattern which is formed by the gas only from the nozzle. If we provide a bubbling flow from the bottom distributor, the interaction of the gas jet from the nozzle and the bubbling flow from the distributor will become more complicated. What will be the flow pattern for such system? Will the breakup of the agglomerates increase when there is more interaction between the gas jet from the nozzle and the bubbling flow from the distributor?

We also compared the gas-water and gas-particle flow in the same setup for the downward micro-nozzle system. Similar penetration depth and flow pattern are found for the two systems. The gas-water system is much easier to observe, because it is transparent for visible light. For future studies of such a system, we can first test the different nozzles and gas flowrates in the gas-water column to optimize the parameters of the nozzle and bed. The X-ray tomography measurement for the gas-particle fluidized bed can be carried out with these optimized parameters.

Overall, high speed X-ray tomography is very promising technique to measure the time-resolved gas distribution in fluidized beds. However, its accuracy and speed of reconstruction can be further improved. The measurements of the gas jets in fluidized beds show its capability to measure the dynamics of fluidization. Nevertheless, more measurements are needed for a systematic study.

References

[1] S. Harding, W. Banzhaf, Fast genetic programming on GPUs, volume 4445 of *Lecture Notes in Computer Science*, 2007. Harding, Simon Banzhaf, Wolfgang 10th European Conference on Genetic Programming Apr 11-13, 2007 Valencia, SPAIN.

[2] M. Olazar, M. Sanjose, F. Penas, A. Aguayo, J. Bilbao, Stability and Hydrodyanmics of Conical Spouted Beds with Binary-Mixtures, Industrial & Engineering Chemistry Research 32 (1993) 2826–2834.

[3] P. K. Mollick, D. Sathiyamoorthy, Assessment of stability of spouted bed using pressure fluctuation analysis, Industrial & Engineering Chemistry Research 51 (2012) 12117–12125.

[4] L. Huilin, S. Yongli, L. Yang, H. Yurong, J. Bouillard, Numerical simulations of hydrodynamic behaviour in spouted beds, Chemical Engineering Research & Design 79 (2001) 593–599.

[5] T. Madhiyanon, S. Soponronnarit, W. Tia, A mathematical model for continuous drying of grains in a spouted bed dryer, Drying Technology 20 (2002) 587–614.

[6] W. Q. Zhong, Y. Q. Xiong, Z. L. Yuan, M. Y. Zhang, Dem simulation of gas-solid

flow behaviors in spout-fluid bed, Chemical Engineering Science 61 (2006) 1571–1584.

[7] O. Gryczka, S. Heinrich, N. G. Deen, M. V. Annaland, J. A. M. Kuipers, M. Jacob, L. Morl, Characterization and cfd-modeling of the hydrodynamics of a prismatic spouted bed apparatus, Chemical Engineering Science 64 (2009) 3352–3375.

[8] K. G. Santos, V. V. Murata, M. A. S. Barrozo, Three-dimensional computational fluid dynamics modelling of spouted bed, Canadian Journal of Chemical Engineering 87 (2009) 211–219.

A

Appendix

In the main text of Chapter 6, we study the time-resolved gas distribution below a downward facing micro-nozzle in a fluidized bed using layer-to-layer X-ray tomographic scanning and cross-correlation analysis. In this appendix, we study an air jet in water using visual observation. Because the gas velocity from the nozzle is very high, the inertial force dominates the gas flow jet. The surface tension, which does not exist for the fluidized bed, has minor influence for the gas-water system in this case.

We measured a gas jet in water in the same column and for similar conditions. We used water instead of solid particles. There is no gas flow from the bottom plate anymore. The gas flow rates from the downward micro-nozzle are exactly the same as we set for the gas/solid fluidized bed. We used a high speed camera to record the phase distribution of gas/liquid flow below the nozzle. A frame rate of 400 fps is used. We recorded the images of each experiment for 10 s.

Bubbling flow is observed from the snapshots (Fig.A.1) for different flow conditions. There is always a large bubble formed below the nozzle. The size and position of these bubbles are similar to those in the fluidized bed for $v_n = 1.7 \times 10^2$ to $3.3 \times 10^2 m/s$. The bubble area is bigger in water than in the fluidized bed for $v_n = 0.8 \times 10^2 m/s$. There are also a lot of mini bubbles encircling the big bubbles. This is similar to the 'diluted area' we observed from the fluidized bed. However, we cannot determine whether the diluted area in the fluidized bed is made of tiny bubbles or if the particle phase is uniformly diluted, because of the limitation of the spatial resolution for our X-ray tomography. The bubbling region rotates around the center of the cross section, which is also observed during the fluidized bed experiments.

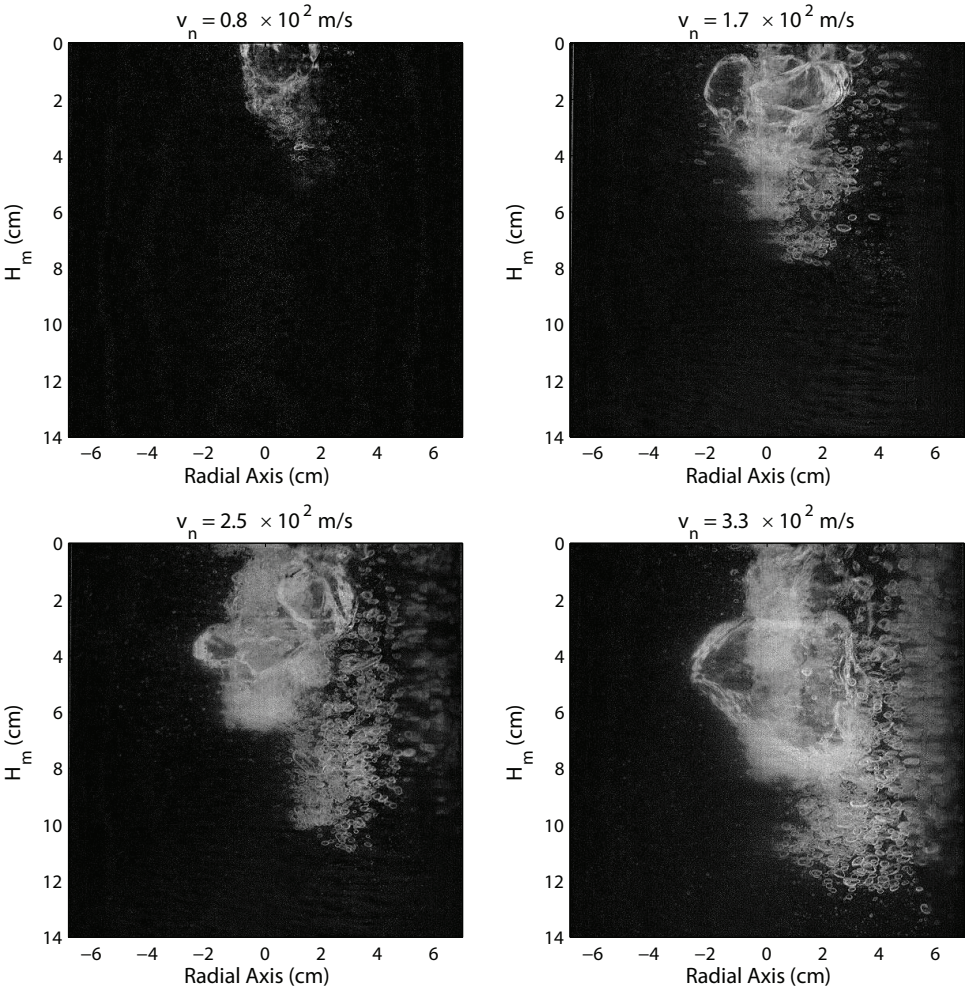

Figure A.1: Snapshots of the gas jet in water for different flow rates. The images are taken by a high speed camera with a frame rate of 400 fps. The resolution is 96 dpi due to the high frame rate. The background (without gas jet) is removed to reduce the influence of the inhomogeneous background light from the cylindrical column.

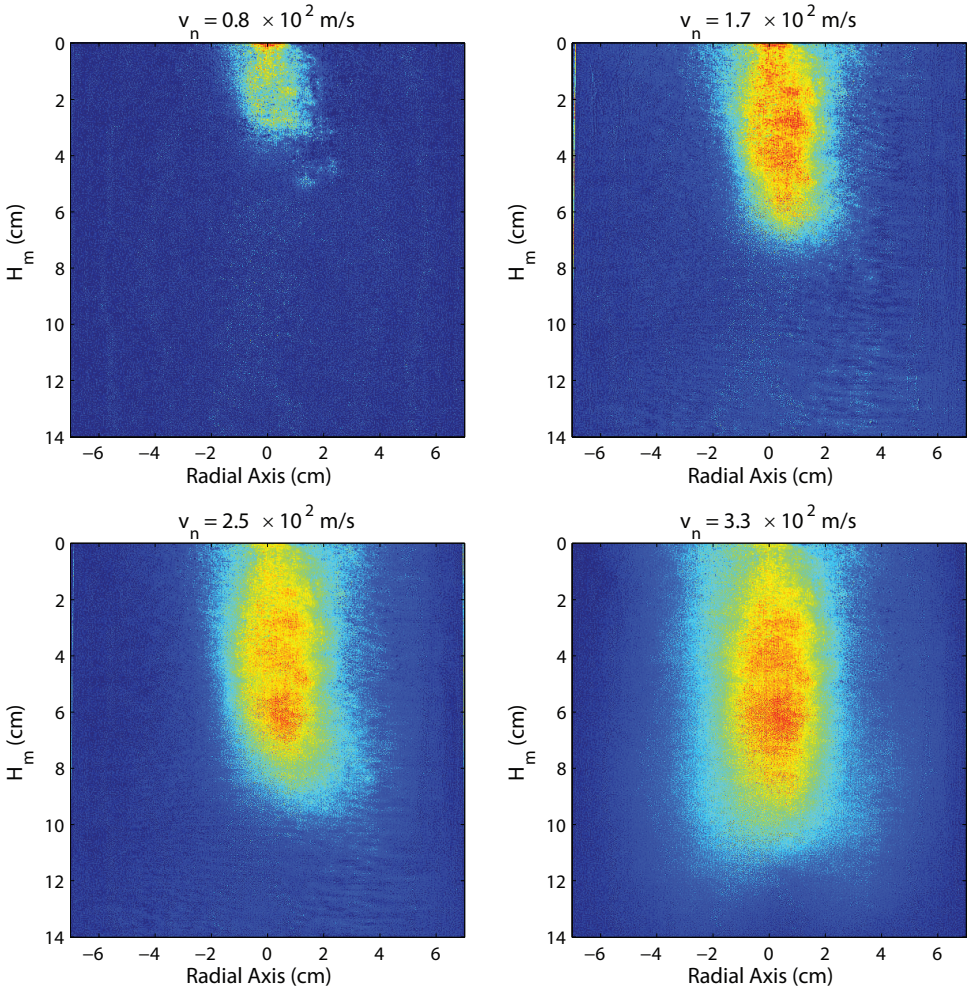

Figure A.2: Influenced area of the gas jet in water. The results are averages from the high speed camera over a period of 10 s. The red color indicates that gas bubbles frequently appear in that position. The deep blue color indicates only water.

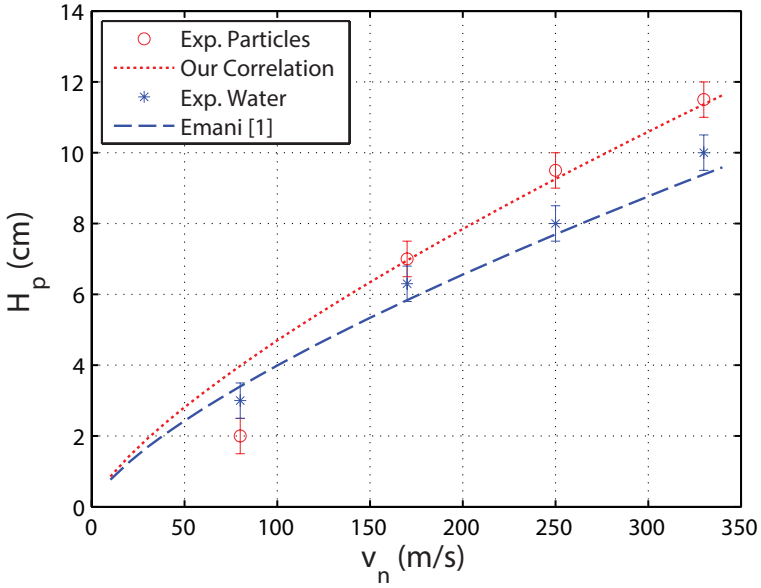

Figure A.3: H_p for the downward micro-nozzle in the gas-solid system ("particles") and in the gas-water system ("water"). 'Our Correlation' is the correlation for the measurement of gas-solid system, which can be found in the main text of the article.

The impact region of the nozzle in water is studied by averaging the images for 10 s, see Fig.A.2. Red is the region where the boundary of gas/water mostly appears. By averaging the 4000 images measured in 10 s, this color map indicates the intensity profile of the bubbling flow. We find similar patterns as the averaged results in the fluidized bed. The bubbling flow mainly happens in the center of the bed. The penetration depth (H_p) is very similar for both measurements (Fig.A.3). We compared the experimental H_p in gas-water system with Emami and Briens [1]'s correlation. It shows that our measurement fits the correlation well. Comparing gas-water and gas-solid system, the H_p for fluidized bed is a little bigger than for water when $v_n > 0.8 \times 10^2 m/s$.

Similar flow patterns are found for the measurements in water and in the fluidized bed. In general, the impact region for water is smaller than for the fluidized bed. We see two reasons for it: (1) the bulk density of fluidized particles is smaller than water (about $0.7 \times 10^3 kg/m^3$ for the fluidized bed, $1.0 \times 10^3 kg/m^3$ for water); (2) there is a surface tension force for water but not for the fluidized bed. Even with these differences, the result of water is accurate enough to represent the gas flow from the downward micro-nozzle in a fluidized bed for engineering application. Compared to the high cost of a X-ray setup, testing in water can be a low-cost alternative for designing the downward micro-nozzle system in a fluidized bed.

We like to stress here, that there are also fundamental differences between an air

jet in water and in a fluidized bed. The gas from the jet will remain in the form of bubbles in the water case. The size of these bubbles is partly governed by surface tension. In a fluidized bed, surface tension does not exist. Moreover, the gas can flow into the powder phase away from the jet region without forming bubbles. These differences will show up most strikingly when the jet flow is low. For the water case than still bubbles need to be formed, while for the fluidized bed, the gas can flow into the dense particle phase without having to form voids. This is probably the reason why the jet depth in the fluidized bed drops quicker to small values for the low jet velocity case.

References

[1] A. Emami, C. Briens, Study of downward gas jets into a liquid, AIChE Journal 54 (2008) 2269–2280.

Summary

High speed X-ray tomography is a promising tool to visualize the time-resolved gas distribution for fluidized beds. The tomography unit at Delft University of Technology is composed of three X-ray tubes and three double-layer detector arrays. The X-ray tubes are places at 120° around the fluidized bed. The detector arrays are placed opposite to the X-ray tubes. The full angle scanning can be done simultaneously, without mechanically rotating the X-ray tube as in traditional medical CT. The temporal resolution can be up to 2500 fps. By using this high speed X-ray tomographic system in my dissertation, we study tomographic reconstruction algorithms and measure different gas jets in the fluidized beds.

To evaluate the performance of the novel reconstruction algorithms for high speed X-ray tomography, Simultaneous Algebraic Reconstruction Technique (SART) and Adaptive Genetic Algorithm (AGA) are compared in Chapter 3. The reconstruction quality of AGA is better than SART at low resolutions, but SART performs better at high resolution in finding the right shape. The system noise influences AGA less than SART. SART is much faster and does not have reproducibility problems; poor reproducibility influences the reliability of AGA.

The features of the reconstruction quality for SART and AGA are further discussed in Chapter 4. AGA is better than SART in distinguishing small phantoms and small distance between phantoms. SART, on the other hand, is better at reconstructing the shapes than AGA. We developed a hybrid approach to combine the advantages of AGA and SART. The result of AGA is used as initial guess for SART in this hybrid algorithm, by which the reconstruction accuracy is indeed improved.

A flat-base spouted bed is studied with the high speed X-ray tomography system in Chapter 5. We focus on the spout diameter and position. The hybrid algorithm is used to visualize the spout in the cross sectional area of the spouted bed. For a more accurate quantitative study, we developed a method to process the raw data directly. The time-averaged results of the spout diameters are validated with the literature. A simple model for the particle circulation is developed based on the time-averaged spout diameter. The model is also validated by measurement of the fountain height.

The time-resolved results of the spout diameter are analyzed by the Power Spectral Density (PSD). The stability of the spout diameter is discussed for different measurement heights and gas flowrates by comparing the average PSD. We find that the most stable spout diameter happens at $U/U_{ms} \sim 1.3$ in the middle part of the spout. The time-resolved spout position is plotted by polar coordinates. We found

that the spout position is more stable when the diameter is less stable, and vice versa.

Another gas jet, i.e. the gas distribution below a downward facing micro-nozzle in a fluidized bed, is also measured using the high speed X-ray tomography in Chapter 6. The improved SART method is used for the reconstruction because we need to consider the transition area between the gas voids and bulk phase. Time-averaged 3-D images of the gas distribution below the nozzle are obtained. The results are compared with direct analysis of the raw data. A bubbling area, a diluted area, and a compacted area are found.

We analyzed the dynamics of the gas voids by employing a cross-correlation technique and inspecting the reconstructed pseudo 3-D image. The cross-correlation estimates the direction of bubble motion, and also helps to calculate the bubble velocity and bubble size. The pseudo 3-D image shows the pattern of the gas voids. We found that single bubbles are regularly formed by the nozzle, and move upwards. The expansion, splitting and coalescence of the bubbles were also observed. The gas injected from the nozzle mainly ends up in bubbles. We compared the fluidized bed results with those obtained for a similar nozzle in a gas-water system, and found a similar flow pattern and penetration depth.

In summary, we improved the accuracy of high speed X-ray tomography by developing novel data processing approaches, such as the hybrid algorithm and raw data processing. We evaluated the dynamics of the spout in a flat-base spouted bed from the tomographic measurements, and developed a model for particle circulation based on these measurements. We also measured the time-resolved gas distribution below the downward facing micro-nozzle using the high speed X-ray tomography. The obtained results illustrate that X-ray tomography is a valuable tool to study gas-solids distribution – both time-averaged and time-resolved in fluidized beds.

Samenvatting

Hogesnelheids-röntgentomografie is een veelbelovende techniek om de tijdsafhankelijke gasdistributie in gefluïdiseerde bedden te visualiseren. De tomograaf van de Technische Universiteit Delft bestaat uit drie röntgenbuizen en drie dubbellaagse sensorrijen. De röntgenbuizen staan om de 120° rondom het gefluïdiseerde bed. De sensorrijen staan tegenover de röntgenbuizen. Zo kan een scan van de volledige omtrek instantaan worden uitgevoerd, zonder de röntgenbuizen rond het bed te roteren, zoals bij een medische CT-scanner. De maximale tijdsresolutie is 2500 fps. Door deze hogesnelheidsröntgentomografie in mijn onderzoek toe te passen, kunnen we tomografische reconstructiealgoritmes bestuderen en verschillende gasstralen in gefluïdiseerde bedden meten.

Om de prestaties van de nieuwe reconstructiealgoritmes voor hogesnelheidsröntgentomografie te bepalen, worden de Simultane Algebraïsche Reconstructie Techniek (SART) en the Adaptieve Genetisch Algorithme (AGA) in hoofdstuk 3 vergeleken. Bij lage resoluties is de reconstructiekwaliteit van AGA beter dan die van SART, maar bij hoge resolutie reconstrueert SART de juiste vorm beter dan AGA. De systeemruis beïnvloedt AGA minder dan SART. SART is veel sneller en heeft geen reproduceerbaarheidsproblemen; een matige reproduceerbaarheid beïnvloedt de betrouwbaarheid van AGA.

Andere aspecten van de reconstructiekwaliteit van SART en AGA worden besproken in hoofdstuk 4. AGA is beter dan SART in het onderscheiden van kleine fantomen en kleine afstanden tussen fantomen. SART daarentegen is beter in het reconstrueren van vormen dan AGA. We hebben een hybride aanpak ontwikkeld, die de voordelen van AGA en SART combineert. In dit hybride algoritme wordt het resultaat van AGA als beginwaarde voor SART gebruikt, waardoor de nauwkeurigheid van de reconstructie inderdaad is verbeterd.

In hoofdstuk 5 is een spouted bed met een vlakke bodem met de hogesnelheidsröntgentomograaf bestudeerd (hoofdstuk 5). We richten ons daarbij op de diameter en de positie van de gasstraal. Het hybride algoritme is toegepast om de gasstraal in de dwarsdoorsnede van het spouted bed te visualiseren. Om nauwkeurigere kwantitatieve studies uit te kunnen voeren hebben we een methode ontwikkeld om de ruwe data direct te verwerken. De tijdsgemiddelde resultaten van de spuitstraaldiameters zijn gevalideerd met de literatuur. Op basis van de tijdsgemiddelde gasstraaldiameter is een simpel model voor de deeltjescirculatie ontwikkeld. Het model is ook gevalideerd met metingen van de fonteinhoogte.

De tijdsafhankelijke resultaten van de gasstraaldiameter zijn geanalyseerd aan de

hand van de spectrale vermogensdichtheid (PSD). Door de gemiddelde PSD te vergelijken is de stabiliteit van de spuitstraaldiameter beschouwd voor verschillende meethoogten en gasdebieten. De spuitstraaldiameter is het meest stabiel als $U/U_{ms} \approx 1,3$ in het midden van de spuitstraal. De tijdsafhankelijke spuitstraalpositie wordt vastgelegd in poolcoördinaten. De spuitstraalpositie blijkt stabieler te zijn, wanneer de diameter minder stabiel is, en omgekeerd.

In hoofdstuk 6 wordt een andere gasstraal, te weten de gasdistributie onder een neerwaarts gerichte microspuitmond in een gefluïdiseerd bed, eveneens gemeten met de hogesnelheids-röntgentomograaf. De verbeterde SART-methode is toegepast voor de reconstructie, omdat we het overgangsgebied tussen de gasbellen en de bulkfase in ogenschouw moeten nemen. We hebben tijdsgemiddelde 3D-beelden van de gasdistributie onder de spuitmond verkregen. De resultaten zijn vergeleken met een rechtstreekse analyse van de ruwe data. Een bubbelend gebied, een verdund gebied en een verdicht gebied worden onderscheiden.

We hebben de dynamica van de gasbellen geanalyseerd door gebruik te maken van een kruiscorrelatietechniek en door het gereconstrueerde pseudo-3D beeld te analyseren. De kruiscorrelatie schat de richting van de bubbelbeweging en helpt tevens de bubbelsnelheid en de bubbelgrootte te berekenen. Het pseudo-3D beeld toont het patroon van de gasbellen. We vinden dat enkelvoudige bubbels regelmatig bij de spuitmond worden gevormd en omhoog bewegen. Expansie, splitsing en samensmelting van bubbels werden ook waargenomen. Het gas dat door de spuitmond wordt geïnjecteerd eindigt voornamelijk in bubbels. We vergelijken de resultaten van het gefluïdiseerde bed met gegevens verkregen voor een soortgelijke spuitmond in een gas-watersysteem en vinden dat het soortgelijk stromingspatroon de penetratiediepte soortgelijk zijn.

Samengevat hebben wij de nauwkeurigheid van hogesnelheidsröntgentomografie verbeterd door nieuwe gegevensverwerkingsmethoden te ontwikkelen, zoals het hybride algoritme en een methode voor de verwerking van ruwe data. We bekeken de dynamica van de spuitstraal in een spuiend bed met een vlakke bodem uit de tomografische metingen en ontwikkelden een deeltjescirculatiemodel, gebaseerd op deze metingen. Tevens hebben we de tijdsafhankelijke gasdistributie onder een neerwaarts gerichte microspuitmond gemeten, gebruik makend van hogesnelheidsröntgentomografie. De verkregen resultaten tonen aan dat röntgentomografie een waardevol instrument is voor het bestuderen van verdelingen van gas en vaste stof in gefluïdiseerde bedden, zowel tijdsgemiddeld als tijdsafhankelijk.

Acknowledgements

Four years ago, nobody expected that I could finish my PhD, even myself. Now, obviously, I am approaching to the end. It was a hard journey. However, with the kind supervisors, colleagues, friends and families around me, it was a wonderful experience. I wish to thank them all in this section.

First of all, I need to express my highest gratitude to my advisors. Rob and Ruud, I feel so lucky to have you as my coaches. Rob, you gave me the opportunity to continue my study in TUDelft. I learned from you for conducting high quality scientific research. You guided me to find my interests in the research. You lead me to the exciting directions and let me enjoy the research. Your encouragements stimulated me to face the difficulties optimistically. Your ideas and advices are of great importance to help me finishing my thesis and publications. Ruud, you have always been patient and kind to my requests. I learned from you to properly communicate with colleagues, and to efficiently present our results to the community. Your careful checking for my writings ensures the quality of my thesis and our publications.

The technicians and secretaries in TP group (previous multi-scale physics) are very professional. They deserve the greatest respect from anyone who has ever worked in this group. Evert, you trained me for the operation of X-ray facilities. You prepared the setup for all my measurements. You assisted me for the data acquisition. We always had happy cooperation. Anita, Amanda, Angela and Fiona, your patience and warmth just like your beauties. You never refused to dealt with my trivial problems, which actually cost a lot of efforts. You saved me so much time.

I would like to thank the advisors in my first year in TUDelft, although I did not finish that project. Chris, I would say I did not waste time from that failed project. You gave me the chance to start my PhD in TUDelft. You helped me to improve my communication skills and study abilities. Your rigorous attitude to scientific problems is a good example for my start. Sasa and Volkert, I enjoyed the discussions with you. You are always gentle and encouraging. In addition, I thank Volkert to train me the microPIV operation, and Mojgan to train me the cleanroom operation.

The students and colleague who have participated in my project can never be omitted. Jasper, you are a talented student. I thank you for your contribution to our hybrid algorithm. Sönke, I thank you for your special idea of the genetic algorithm. Christo, I thank you for the joint publication.

My life in the TP group could not have been this exciting without the interesting colleagues. I warmly thank all of you for sharing happiness and joy during cele-

brations, drinks, lunches, and dinners. Mohammad, Farzad, Annekatrien, Anton, Milos, Wenjie, Rajat, Bernhard, Rudi, Koen, Cees, Michiel, and Niels, your names are always in my sweet memories.

I would like to express my special thanks to my dear officemates, Reza, Galileu, Dries, and Duong. You are more good friends than ordinary colleagues. Our exiting office discussions enlarged my vision of the world. Our weekend parties brought a lot of happiness to me. I enjoyed to play tennis and to have beers with you. Reza, I thank you for sharing the apartment in my last year. Dries, I thank you for translating my thesis Summary. Our weekly swimming is a great habit, which will be beneficial for our entire life.

I had hard time in the previous four years, but my life was colorful and joyful. My sweet memories in TUDelft are mostly composed of exciting travels and dinner parties. I was lucky to meet many wonderful friends. Adele, you are the first friend I have known in Delft. We had many trips together. You served me delicious dinners weekly like a real family during my downs. You encouraged me to practice piano regularly. No more words for our friendship, the time proves. Yuqing, we traveled ten countries together. You are a steady companion on the trip. I learned a lot from your tolerance and modesty. Shidan, you are always full of energy. I charged happiness from our monthly dinners. I learned from you to be easy for my life.

I would like to thank those friends who have accompanied me in the trips, Zhu Yunpeng, Xu Shiming, Ge Xin, Yang Dan, Li Zheng, Ge Mengqiu, Li Cong, and Yu Chang. I also want to thank the friends who have enriched my life in Delft, Fan Liyuan, Zhao Qiaole, Li Zhang, Fan Huajun, Xiao Fangliang, Lv Xiaoqian, Cheng Peiyao, Su Ping, and Nicky. It does not mean I forget those friends whose names were not listed here. You are always appreciated to exist in my life in Delft.

The last few months of my PhD were spent in China. I am grateful that I had an easy life in such a hard situation with the help from my MSc supervisor and friends. Baojiang and Zhiyuan, I would like to thank you to provide me the comfortable accommodation and office. Because of you, I can focus on the final works without worrying about my life. Xiuhua, I want to thank you for standing by my side in the last half year.

The last part is dedicated to the most important and special people, my dear families. Your continuous love and support are the source of my power for running to this end. I feel sorry that I had limited time to accompany you. I wish I can change the situation after I obtain the PhD.

Curriculum Vitæ

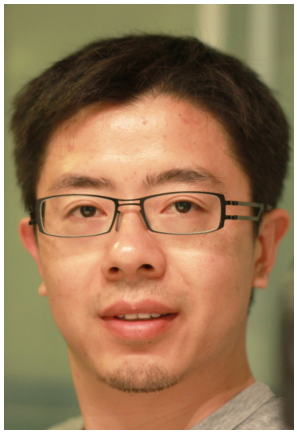

Xiaogang Yang was born on May 8^{th}, 1984 in Jingchuan, Gansu Province, China. He lived most of his youth in this town, and had primary school to high school study there. From 2002, he started BSc study in China University of Petroleum (UPC) in Shandong Province. The major is Marine Engineering, which is mainly for offshore oil and gas development. From 2006, he continued MSc study in the same university, under the supervision of Prof. Baojiang Sun. The topic is multiphase problems in deepwater drilling. In 2009, he graduated from UPC and started his PhD in Delft University of Technology. He studied microfluidics with Prof. Chris Kleijn, Dr. Sasa Kenjeres and Dr. Volkert van Steijn. From 2011, he switched to the present project: high speed X-ray tomographic measurements of fluidized beds, under the supervision of Prof. Robert F. Mudde and Dr. J. Ruud van Ommen.

List of Publications

Papers

1. **Xiaogang Yang**, J. Ruud van Ommen, and Robert F. Mudde, *Comparison of Genetic Algorithm and Algebraic Reconstruction for X-Ray Tomography in Bubbling Fluidized Beds*, Powder Technology (2014), 253, 626–637, DOI: 10.1016/j.powtec.2013.12.007.

2. **Xiaogang Yang**, J. Ruud van Ommen, E. Wagner, and Robert F. Mudde, *Time-resolved Characterization of a Flat-Base Spouted Bed with a High Speed X-ray System*, Chemical Engineering Journal (2014), 254, 143–152, DOI: 10.1016/j.cej.2014.05.050.

3. **Xiaogang Yang**, J. Ruud van Ommen, and Robert F. Mudde, *Gas Distribution of a Downward Micro-nozzle Assisted Fluidized Bed of Fine Powder*, Chemical Engineering Journal (2015), 264, 945–953, DOI:10.1016/j.cej.2014.11.127.

4. **Xiaogang Yang**, J. Ruud van Ommen, J. Schoormans and Robert F. Mudde, *A hybrid tomographic reconstruction algorithm for a high speed X-ray tomography system*, Computer Physics Communication,–accepted.

5. C. Rautenbach, R.F. Mudde, **X. Yang**, M.C. Melaaen, and B.M. Halvorsen, *A comparative study between electrical capacitance tomography and time-resolved X-ray tomography*, Flow Measurement and Instrumentation (2013), 30, 34–44, DOI: 10.1016/j.flowmeasinst.2012.11.005.

Proceedings

1. **Xiaogang Yang**, J. Ruud. van Ommen, Robert F. Mudde, *Time-resolved Measurement of the Spout Shape inside a Spouted Bed with High Speed X-ray Tomography*, 9th European Congress of Chemical Engineering, The Hague, The Netherlands, 2013.

2. **Xiaogang Yang**, J. Ruud. van Ommen, E. Wagner, Robert F. Mudde, *Spout Shape and Stability in a Flat-Base Spouted Bed Using a High Speed X-Ray Tomography*, AIChE 2013 Annual Meeting 317379, San Fransisco, USA, 2013.

3. J. Ruud van Ommen, **Xiaogang Yang**, Jess Gmez Hernndez, Jelle J. Sonneveld, Evert C. Wagner, Robert F. Mudde, *Recent Advances in X-Ray Tomography of Fluidized Beds*, AIChE 2014 Annual Meeting 386635, Atlanta, USA, 2014.